10-2-2015

Design, Synthesis and Characterization of Transition Metal Oxide Nanomaterials as Efficient Sorbents and Emerging Catalysts and Investigation of Carbon Structure-Oxidation Activity Correlations

Lakshitha R. Pahalagedara
lakshitha.pahalagedara@uconn.edu

Design, Synthesis and Characterization of Transition Metal Oxide Nanomaterials as Efficient Sorbents and Emerging Catalysts and Investigation of Carbon Structure-Oxidation Activity Correlations

Lakshitha Randimal Pahalagedara, Ph. D

University of Connecticut, 2015

The research work presented here is focused on designing and characterizing new synthetic techniques for transition metal oxide nanomaterials as efficient sorbents and highly active catalysts and investigating carbon structure-oxidation activity correlations for diesel particulate filter optimization. This thesis is delineated into three parts.

The first part describes the synthesis of mesoporous cobalt oxides (M-Co-X, X=150, 250, 350, 450ºC) with tunable porosity, and crystallinity based on an inverse micelle soft template method and investigation of the M-Co-X materials as desulfurizing sorbents in a fixed bed reactor in the temperature range of 25-250ºC. A considerably high sulfur sorption capacity was observed even at room temperature (13.4 g S/ 100 g sorbent) and very high values were observed in the temperature range of 175-250ºC (65.0-68.9 g S/ 100 g sorbent). The sulfided materials were further analyzed with LA-XRD, WA-XRD, N_2 sorption studies,

FESEM, FESEM-EDX, TEM, FETEM-EDX, TGA, and TPO. The M-Co-250 material reached 100% theoretical sulfur capacity at 150ºC. The presence of interconnected intraparticle voids and surface exposed particles were found to be the critical factors determining the ability of H_2S to diffuse in the sorbent. The mesostruture of the M-Co-X material was preserved even after sulfidation. Other mesoporous metal oxides synthesized by the same method (Cr_2O_3 (UCT-37), CuO (UCT-11), Mn_2O_3 (UCT-1), and Fe_2O_3 (UCT-5)) also showed sulfur capacities of 2-200 times more than the corresponding nonporous materials.

The second part presents a microwave assisted hydrothermal synthesis and characterization of cobalt doped cryptomelane type manganese oxide (K-OMS-2) microwires. Their catalytic activity was tested in an oxidation reaction with benzyl alcohol as the substrate and the cobalt doped OMS-2 materials showed 100% selectivity towards benzyl aldehyde with a conversion of 55%. The cobalt doped OMS-2 materials were also investigated as a desulfurization sorbent in a fixed bed reactor at 250ºC where high sulfur sorption capacities (49.4 g sulfur/100 g sorbent) were observed. Here, the structure controlled synthesis was performed using a facile one step microwave assisted hydrothermal method (MWHY) associated with a rapid temperature ramping (200ºC/min). The structural effects induced by the compositional control of transition metal dopants on the cryptomelane (space group I4/m) body centered tetragonal structure were identified with X-ray diffraction (XRD) and transmission electron microscopy (TEM). The XRD and TEM results showed that the systematic variance of the cobalt content was accompanied by a stepwise lattice

expansion of (110) plane from 6.70 to 7.43 Å. The XRD, high resolution TEM (HRTEM)/TEM, Raman spectroscopy, Fourier transform infrared (FTIR) spectroscopy, thermogravimetric analysis (TGA), and X-ray photoelectron spectroscopy (XPS) data suggested that the as-synthesized cobalt doped OMS-2 materials were also crystalline with no segregated metal oxide impurities. The uniform morphology of the metal doped OMS-2 materials was observed by the field-emission scanning electron microscopy (FESEM), whereas energy-dispersive X-ray (EDX) analysis confirmed the successful incorporation of metal dopant into the OMS-2 structure. Inductively coupled plasma atomic emission spectroscopy (ICP-AES) showed a higher degree of doping (Co/Mn = ~0.26) associated with MWHY method over conventional methods. On the other hand, TGA demonstrated that the as-synthesized materials were more thermally unstable than their undoped counterparts. The observed structural and chemical characteristics upon doping with some metal cations were explained by the Jahn-Teller distortion.

The third part demonstrates a comprehensive investigation of structure-activity relationships for a diesel engine soot sample (Corning) and ten commercially available carbon black samples. Particle sizes were determined using Scanning Electron Microscopy (SEM) and Transmission Electron Microscopy (TEM); specific surface area was determined by nitrogen sorption studies; while the microstructure was investigated by X-ray Diffraction (XRD) peak profile analysis, Raman spectroscopy, and TEM. Oxidation activity of these samples was studied using Thermo Gravimetric Analysis (TGA) under an

oxidative (10% O_2) environment consistent with the typical oxygen levels in the diesel engine exhaust. Various structural parameters, such as the average particle size, specific surface area, degree of organization, and average crystallite stacking height, were correlated with the TGA oxidation activity data. In general, samples with low particle size, high surface area, highly amorphous nature (low degree of organization), and low crystallite stacking height showed high oxidation activity. A second diesel engine soot sample (Corning), which was collected at different operating conditions, was used to validate the obtained structure-activity correlations. Overall, our rigorous analysis for a large number of samples with multiple techniques has indicated unique and novel correlations between soot structure and reactivity.

Design, Synthesis and Characterization of Transition Metal Oxide Nanomaterials as Efficient Sorbents and Emerging Catalysts and Investigation of Carbon Structure-Oxidation Activity Correlations

Lakshitha Randimal Pahalagedara, Ph. D

B.Sc., University of Peradeniya, 2009

A Dissertation

Submitted in Partial Fulfillment of the

Requirement for the Degree of

Doctor of Philosophy

At the University of Connecticut

2015

APPROVAL PAGE

Doctor of Philosophy Dissertation

Design, Synthesis and Characterization of Transition Metal Oxide Nanomaterials as Efficient Sorbents and Emerging Catalysts and Investigation of Carbon Structure-Oxidation Activity Correlations

Presented by

Lakshitha Randimal Pahalagedara, B.Sc.

Major Advisor _____
Dr. Steven L. Suib

Associate Advisor _____
Dr. Christian Bruckner

Associate Advisor _____
Dr. Alfredo Angeles-Boza

Associate Advisor _____
Dr. Jie He

Associate Advisor _____
Dr. Fatma Selampinar

University of Connecticut

2015

DEDICATION

To my parents, my wife Madhavi, my sister, brother-in-law and nieces

for the amazing support you have always provided

ACKNOWLEDGEMENTS

Foremost, I would like to express my sincere gratitude to my advisor Dr. Steven L. Suib for his guidance and continuous support throughout my graduate studies. His motivation, enthusiasm, and immense knowledge of multidisciplinary research were critical to me as a research scientist. He also gave me great opportunities to grow in other areas such as communication, administration, and leadership. I would also like to extend my gratitude to my associate advisors, Dr. Christian Bruckner, Dr. Alfredo Angeles-Boza, Dr. Jie He, and Dr. Fatma Selampinar for their generous help, motivation, and advice.

I would also like to express my gratitude to Drs. Frank Galasso, William Willis, Ashish Mhadeshwar, Saminda Dharmarathna, Cecil King'ondu, Hector Garces, Homer Genuino, Hom Sharma, Hui Huang, Altug Poyraz, Chung-Hao Kuo and Yong-Tao Meng for their help and support. My appreciation also goes to current group members Sheng-Yu Chen, Saiful Islam Liton, David Kriz, Curt Guild, Sourav Biswas and Wenqiao Song for their support in my projects.

I would like to extend my heartiest gratitude to my wife Madhavi, who has been the most patient and supportive person who stood beside me during my academic journey over the past five years. I am highly indebted to my parents M. B. Pahalagedara and S. D. Pahalagedara, for their continuous support in my education. Finally I would like to express my deepest gratitude to my sister, Kalpanie and brother-in-law, Dhammika who motivated and supported me throughout my life.

TABLE OF CONTENTS

CHAPTER I. LOW TEMPERATURE DESULFURIZATION OF H_2S: HIGH SORPTION CAPACITIES BY MESOPOROUS COBALT OXIDE VIA INCREASED H_2S DIFFUSION. 1

1.1. INTRODUCTION 1

1.2. EXPERIMENTAL SECTION 4

1.2.1. Materials 4

1.2.2. Synthesis of mesoporous cobalt oxide 4

1.2.3. Catalyst Characterization 5

1.2.3.1. X-Ray Powder Diffraction Studies 5

1.2.3.2. Scanning Electron Microscopy and Energy Dispersive X-ray Spectroscopy 5

1.2.3.3. Transmission Electron Microscopy and Focused Ion Beam Technology 6

1.2.3.4. N_2 Sorption Studies 6

1.2.3.5. Thermo Gravimetric Analysis 6

1.2.3.6. X-ray Photoelectron Spectroscopy 7

1.2.3.7. Temperature Programmed Oxidation-Mass Spectrometry 7

1.2.4. Sulfidation Reactor and Sulfur Sorption Capacity 7

1.3. RESULTS 9

1.3.1. Physiochemical Properties of Commercial and Mesoporous Cobalt Oxide Materials 9

1.3.2. Desulfurization Performances Of Commercial And Mesoporous Cobalt Oxide Materials 13

1.3.3. Comparison of Physiochemical Properties of M-Co-250 before and After Sulfidation at 200ºC 13

1.3.4. Desulfurization Activities of Other Mesoporous (UCT) Materials ... 22

1.4. DISCUSSION 24

1.5. CONCLUSIONS 28

REFERENCES 29

CHAPTER II. MICROWAVE ASSISTED HYDROTHERMAL SYNTHESIS OF α-MnO_2: LATTICE EXPANSION VIA RAPID TEMPERATURE RAMPING AND FRAMEWORK SUBSTITUTION. 36

2.1. INTRODUCTION 36

2.2. EXPERIMENTAL 40

2.2.1. Materials 40

2.2.2. Catalyst Preparation 41

2.2.3. Catatyst Characterization 41

2.2.3.1. X-Ray Powder Diffraction Studies 41

2.2.3.2. Scanning Electron Microscopy and Energy Dispersive X-ray Spectroscopy 42

2.2.3.3. Transmission Electron Microscopy 42

2.2.3.4. Fourier Transformation infra Red (FT-IR) Spectroscopy 42

2.2.3.5. Thermo Gravimetric Analysis 43

2.2.3.6. N_2 Sorption Studies 43

2.2.3.7. Raman Spectroscopy 43

2.2.3.8. Inductively Coupled Plasma-Atomic Emission Spectroscopy 44

2.2.3.9. X-ray Photoelectron Spectroscopy 44

2.2.4. Catalytic Performance 44

2.2.5. Desulfurization Performance 45

2.3. RESULTS 46

2.3.1. Microwave assisted hydrothermal (MWHY) synthesis of K-OMS-2 and metal doped K-OMS-2 nanomaterials ([M]-K-OMS-2) and the effects of the reaction parameters on the lattice parameters..... 46

2.3.2. Effect of cobalt doping on the shape evolution of [Co]-OMS-2_{MWHY} nanowires 50

2.3.3. Effect of reaction parameters on the extent of cobalt doping 51

2.3.4. Effect of cobalt doping on the microstructure 52

2.3.5. Effect of cobalt doping on the surface properties, surface structure and composition 55

2.3.6. Effect of cobalt doping on the Thermal stability 62

2.3.7. Selective oxidation of benzyl alcohol to benzyl aldehyde..... 63

2.3.8. Desulfurization performance for the removal of hydrogen sulfide.64

2.4. DISCUSSION 68

2.5. CONCLUSIONS 79

REFERENCES 80

CHAPTER III. STRUCTURE AND OXIDATION ACTIVITY CORRELATIONS FOR CARBON BLACKS AND DIESEL SOOT 87

3.1. INTRODUCTION 87

3.2. EXPERIMENTAL SECTION 91

3.2.1. Materials 91

3.2.2. Catalyst Characterization 93

3.2.2.1. X-Ray Powder Diffraction Studies 93

3.2.2.2. Scanning Electron Microscopy 94

3.2.2.3. Transmission Electron Microscopy 94

3.2.2.4. N_2 Sorption Studies 94

3.2.2.5. Raman Spectroscopy 95

3.2.2.1. Thermo Gravimetric Analysis 95

3.3. RESULTS 95

3.3.1. Effect of particle size on oxidation activity 95

3.3.2. Effect of surface area on oxidation activity 98

3.3.3. Effect of degree of organization on oxidation activity 100

3.3.4. Effect of crystallite stacking height on oxidation activity 102

3.4. DISCUSSION 105

3.5. CONCLUSIONS 114

REFERENCES 115

LIST OF FIGURES

Figure 1.1. (a) Low angle and (b) High angle PXRD patterns (c) Nitrogen sorption isotherms and (d) BJH desorption pore size distributions of commercial cobalt oxide (C-Co) and mesoporous cobalt oxides (M-Co-X, X=150, 250, 350, 450ºC) (e) Low resolution and (f), (g) high resolution FESEM images of M-Co-250 which contains micron sized openings which enhances the diffusion of reactant species..... 10

Figure 1.2. (a) Breakthrough curves and (b) Sulfur sorption capacities of commercial cobalt oxide (C-Co) and mesoporous cobalt oxides (M-Co-X, X=150, 250, 350, 450ºC) after sulfidation at 200 ºC. Mesoporous cobalt oxide materials calcined at 250 and 350ºC show the highest breakthrough times and the highest sulfur sorption capacities. (c) Breakthrough curves and (d) Sulfur sorption capacities of mesoporous cobalt oxide (M-Co-250) after sulfidation at different temperatures. Mesoporous cobalt oxide materials sulfided at temperatures above 175°C show the highest breakthrough times and the highest sulfur sorption capacities..... 14

Figure 1.3. (a) Low angle PXRD patterns (b) High angle PXRD patterns (c) Nitrogen sorption isotherms and (d) BJH desorption pore size distributions of mesoporous cobalt oxide (M-Co-250) before and after sulfidation at 200 °C. Cobalt oxide is converted to cobalt sulfide retaining its mesoporous nature. 15

Figure 1.4. Wide-angle PXRD patterns of (a) M-Co-250 and after sulfidation at (b) 25ºC (c) 100ºC (d) 175ºC and (e) 200ºC..... 16

Figure 1.5. (a) Nitrogen sorption isotherms and (b) BJH pore size distributions of M-Co-250 before and after sulfidation at different temperatures. 17

Figure 1.6. (a) Low resolution and High resolution (inset) FESEM images, FESEM-EDX elemental maps for (b) Co, (c) S, and (d) O, (e) TEM image, and FETEM-EDX elemental maps of the cross-sectional view of isolated microsphere for (f) Co (g) S (h) O for mesoporous cobalt oxide (M-Co-250) after sulfidation**.** 18

Figure 1.7. (a) FESEM image of M-Co-250 after sulfidation at 200ºC (b) FESEM-EDX line analysis from point A to B for cobalt, oxygen, sulfur and silicon. .. 19

Figure 1.8. FESEM-FIB images of (a) Pt coating and (b) cross sectional view of M-Co-250 sulfided at 200ºC. 19

Figure 1.9. XPS data (a) before and after sulfidation at 200ºC and (b) S 2p region of sulfided M-Co-250. 21

Figure 1.10. (a) Thermogravimetric analysis of mesoporous cobalt oxide calcined at 250ºC before and after sulfidation and (b) Temperature programmed oxidation (TPO) of mesoporous cobalt oxide after sulfidation. 22

Figure 1.11. Breakthrough curves of fresh M-Co-250 and regenerated M-Co-250 for sulfidation at 200°C. The mesoporous cobalt oxide can be regenerated at 400°C under air without a significant loss in its sulfur sorption capacity. 23

Figure 2.1. Polyhedral representation of the crystal structure of α-MnO_2 type materials. The structure is viewed down the c-axis of the tetragonal unit cell. Potassium atoms are shown in grey and MnO_6 octahedra are shown in brown. 37

Figure 2.2. XRD patterns of different [M]-K-OMS-2 materials synthesized by MWHY method where M^{n+}/ Mn^{2+} initial molar is 0.50. 48

Figure 2.3. (a) XRD patterns of 0.50[Co]-K-OMS-2 materials synthesized by different methods (b) A perspective drawing of the solid state crystal structure of K-OMS-2, showing octahedrally coordinated porous framework and the imaginary (110) plane: red, O; grey, Mn; purple, K. 49

Figure 2.4. (a) XRD patterns of [Co]-K-OMS-2_{MWHY} at different initial Co^{2+}/Mn^{2+} initial molar ratios (b) Change in d-spacing with Co^{2+}/Mn^{2+} initial molar ratio. 49

Figure 2.5. FE-SEM images of (a) K-OMS-2_{MWHY} (b) 0.50[Co]-K-OMS-2_{MWHY} (c) 0.50[Co]-K-OMS-2_{REF} and (d) 0.50[Co]-K-OMS-2_{HY}. 50

Figure 2.6. (a) Co/Mn and K/Mn molar ratios of K-OMS-2_{REF} and 0.50[Co]-K-OMS-2 synthesized with different synthesis methods, obtained by ICP-AES analysis (b) Change in composition of Mn, Co, and K with increasing cobalt amount obtained by EDX analysis. 52

Figure 2.7. (a) FE-SEM image and EDX elemental maps of (b) oxygen (c) potassium (d) manganese and (e) cobalt in 0.50[Co]-K-OMS-2_{MWHY}. 53

Figure 2.8. TEM images of (a) K-OMS-2_{MWHY} (b) 0.50[Co]-K-OMS-2_{MWHY} and (c) 0.70[Co]-K-OMS-$2_{MWHY.}$ 54

Figure 2.9. TEM and HRTEM images of (a) K-OMS-2_{MWHY} (b) 0.50[Co]-K-OMS-2_{MWHY} and (c) 0.70[Co]-K-OMS-2_{MWHY}.....54

Figure 2.10. N_2 adsorption/ desorption isotherms and Barrett-Joyner-Halenda (BJH) desorption pore size distribution curves (inset) of (a) K-OMS-2_{MWHY} (b) 0.50 [Co]-K-OMS-2_{HY} and (c) 0.70 [Co]-K-OMS-2_{MWHY}. 55

Figure 2.11. FTIR spectra of (a) K-OMS-2_{MWHY} (b) 0.50[Co]-K-OMS-2_{MWHY}. ...57

Figure 2.12. (a) FTIR spectra and (b) Raman spectra of K-OMS-2_{MWHY} and 0.50[Co]-K-OMS-2_{MWHY}. 58

Figure 2.13. XPS spectrum of 0.50[Co]-K-OMS-2_{MWHY}.....59

Figure 2.14. (a) XPS spectrum of Co 2p region of 0.50[Co]-K-OMS-2_{MWHY} (b) thermogravimetric analysis profiles of K-OMS-$2_{MWHY,}$ 0.50[Co]-K-OMS-2_{MWHY} and 0.70[Co]-K-OMS-2_{MWHY}.....60

Figure 2.15. XPS spectra of O 1s region of (a) K-OMS-2_{MWHY} (b) 0.50[Co]-K-OMS-2_{MWHY}……..61

Figure 2.16. XPS spectrum of Mn 2p region of 0.50[Co]-K-OMS-2_{MWHY}…….62

Figure 2.17. XRD pattern of 0.50[Co]-K-OMS-2_{MWHY} after sulfidation at 250ºC.65

Figure 2.18. (a) FE-SEM image and EDX elemental maps of (b) oxygen (c) sulfur (d) manganese and (e) cobalt in 0.50[Co]-K-OMS-2_{MWHY} after sulfidation at 250ºC…….66

Figure 2.19. (a) Breakthrough curves (b) sulfur sorption capacities for K-OMS-2_{MWHY} , 0.50[Co]-K-OMS-2_{HY} and 0.50[Co]-K-OMS-2_{MWHY} and (c) possible $H_2S_{(g)}$ sorption mechanism by K-OMS-2: white, H; red, O; yellow, S; grey, K…….67

Figure 2.20. EDX spectrum of 0.50 [Co]-K-OMS-2_{MWHY} after sulfidation……78

Figure 3.1. FE-SEM images for (a) Monarch 1400, (b) Monarch 280, (c) Printex U, and (d) diesel soot- 1……...96

Figure 3.2. Correlation for oxidation activity with the average initial particle size. Panels a and b correspond to the light-off temperatures T_{10} and T_{50},respectively……...97

Figure 3.3. FE-SEM image for diesel soot-2……98

Figure 3.4. Correlation for oxidation activity with the specific surface area. Panels a and b correspond to the light-off temperatures T_{10} and T_{50}, respectively……..99

Figure 3.5. Raman spectra for carbon blacks and diesel soot-1……100

Figure 3.6. Correlation for oxidation activity with the intensity ratio of the Raman D1 and G peaks……101

Figure 3.7. Raman spectrum (λ=514 nm) for diesel soot-2 ……102

Figure 3.8. XRD patterns for carbon blacks and diesel soot-1 ……103

Figure 3.9. Correlation for oxidation activity with the crystallite stacking height……..103

Figure 3.10. XRD spectrum for diesel soot-2……104

Figure 3.11. Proposed structure of carbon black …….....106

Figure 3.12. Overview HRTEM image of Printex-G……..107

Figure 3.13. (a) Overview and (b) enlarged HRTEM images of Printex-XE2B……..107

Figure 3.14. Overview HRTEM image of Monarch 1300……109

Figure 3.15. Overview HRTEM image of diesel soot-1……..……110

Figure 3.16. (a) TEM and (b) HRTEM images of diesel soot-2……..….111

Figure 3.17. HRTEM images of (a) the smallest (~10 nm) and middle sized (~39 nm), and (b) the largest (~84 nm) particles of Vulcan XC 72R…….……113

Figure 3.18. Summary of the variation of oxidation activity as correlated to particle size, surface area, degree of organization, and crystallite stacking height……..….114

LIST OF SCHEMES

Scheme 1.1. Schematic representation of the experimental set-up. 8

Scheme 2.1. Selective oxidation of benzyl alcohol to benzyl aldehyde..... 44

Scheme 2.2. Schematic representation of the experimental set-up. 46

LIST OF TABLES

Table 1.1. Structural parameters of mesoporous cobalt oxide materials before and after sulfidation. 12

Table 1.2. The sulfur sorption capacities of mesoporous and nonporous MO_x materials 24

Table 2.1. BET surface area of as synthesized OMS-2 materials. 57

Table 2.2. Selective oxidation of benzyl alcohol. 64

Table 2.3. Average weight and atomic percentages of elements in 0.50[Co]-K-OMS-2_{MWHY} after sulfidation. 78

Table 3.1. Engine operating conditions during diesel soot sampling. All soot was collected under steady-state operating conditions 92

Table 3.2. Physical properties and oxidation activity data for carbon black and diesel soot samples 92

CHAPTER I. LOW TEMPERATURE DESULFURIZATION OF H_2S: HIGH SORPTION CAPACITIES BY MESOPOROUS COBALT OXIDE VIA INCREASED H_2S DIFFUSION.

1.1. Introduction

Sulfur containing compounds (Such as H_2S, COS, dimethyl sulfide (DMS), and CS_2) are considered as the naturally occurring contaminants in hydrocarbon feedstock, natural gas, and coal gas.[1-6] The removal of sulfur containing impurities are economically beneficial to avoid corrosion, catalyst deactivation, and electrode poisoning. From an environmental point of view, the emission of sulfur compounds into the atmosphere causes acid rains. Among the above mentioned sulfur containing impurities, H_2S has drawn special attention not only due to being hazardous, toxic, and corrosive but also its wide occurrence both naturally and in industrial processes.[1-3] Condensation, oxidation, catalytic combustion, and acid gas treatments are the widely used methods for H_2S removal.[7-11] Among them, H_2S adsorption has been widely preferred due to high efficiency, reliability, and availability of wide range of sorbents and low working temperatures. Common sorbents are activated carbon, zeolites, modified alumina, clays, metal oxides or mixed metal oxides.[2,3] Among these, the mixed metal oxides have become more popular in desulfurization processes due to a wide range of working temperatures (300-800ºC) and viability of compositional changes.[7,12] Zinc, manganese, copper, iron, cobalt, nickel, chromium, and calcium based oxides are the most extensively studied oxides for desulfurization

in solid-gas reactions due to their high affinity to S (Eq. 1.1)[7,9,13-17] where M_xO_y and M_xS_y are the initial metal oxide sorbent and the metal sulfide after the reaction

$$M_xO_{y(s)} + yH_2S_{(g)} \rightarrow M_xS_{y(s)} + yH_2O_{(g)} \qquad (1)$$

Thus far, zinc oxide based sorbents with high sulfur affinity for desulfurization and high thermal stability have been proven to be practically applicable and as potential materials for H_2S removal. However, desulfurization processes by zinc oxides require high temperatures for efficient removal. Therefore, recently much attention has been drawn in developing low cost sorbents with lower operation temperatures. Recent thermodynamic studies indicate that sorbents based on transition metal oxides such as oxides of Co, Cu, Mn, Cr, Fe, Ni, and W are possible candidates for low temperature desulfurization.[18-20,20-24] Among them, cobalt oxide based sorbents are found to be very promising with higher degree of H_2S removal rates and subsequent metal sulfide conversions obtained with different cobalt oxide based sorbents.[9] However, in these studies cobalt is not the major component of the designed sorbents. These materials also suffer from the limitations for lowering of the desulfurization operating temperatures (<400 ºC) while maintaining satisfactory sulfur sorption capacities.

The diffusion of H_2S through the material is critical for reaching the active sites to obtain a high efficiency. Therefore, the physicochemical properties (surface area, porosity, morphology, and pore volume) of sorbents play a crucial role.[25,26] These properties are known to be directly correlated to the

desulfurization efficiency. In this work, we report a low temperature and efficient desulfurization (H_2S removal) by novel mesoporous cobalt oxide materials (University of Connecticut, UCT mesoporous materials). The materials are prepared by a recently developed inverse micelle templating sol-gel route.[27] The method allows one to prepare thermally stable and high surface area mesoporous transition metal (TM) oxides with tunable mesopore sizes and volumes. With the method, it is also possible to evaluate the role of the physicochemical properties on the desulfurization performances. Unlike traditional mesoporous materials, these UCT materials are formed by randomly packed monodispersed nano-particles and mesopores are formed by connected intraparticle voids.[28,29,30] The tested mesoporous cobalt oxides show significantly higher sulfur sorption capacity even at room temperature. The highest H_2S removal can be reached at temperatures as low as 175ºC. Moreover, the performances of mesoporous cobalt oxides are almost 60 times higher than their nonporous analogues. The mesoporosity of the material is modulated by varying the calcination temperatures of the materials. The chemical, structural, and morphological changes due to sulfidation of cobalt oxides were closely monitored by numerous characterization techniques (LA-PXRD, WA-PXRD, N_2 sorption, EDX, XPS, TPO, TGA). In addition to the mesoporous cobalt oxide, several other mesoporous materials (Mn, Ni, Cr etc.) prepared with the same approach were also tested for desulfurization. The sulfur sorption capacities of their respective commercially available nonporous counterparts were also tested for better evaluation of the removal performances.

1.2. Experimental Section

1.2.1. Materials

Cobalt(II) nitrate hexahydrate ($Co(NO_3)_2 \cdot 6H_2O \geq 98.0\%$), 1-butanol (anhydrous, 99.8%) and Poly (ethylene glycol-block-Poly(propylene glycol)-block-Poly(ethylene glycol) PEO_{20}-PPO_{70}-PEO_{20} (Pluronic P123) were purchased from Sigma Aldrich. Concentrated nitric acid (HNO_3, 68-70%) was purchased from J.T. Baker. All chemicals were used without further purification.

1.2.2. Synthesis of mesoporous cobalt oxide

$Co(NO_3)_2 \cdot 6H_2O$ (0.02 mol) was dissolved in a solution containing 0.23 mol of 1-butanol, 0.038 mol of HNO_3 and 4.31×10^{-4} mol of P123 surfactant in a 150 mL beaker at room temperature (RT) and under magnetic stirring. The obtained clear gel was place in an oven at 120ºC for 12 h. The obtained powder was washed several times with ethanol. Then, the powder was dried in a vacuum oven overnight and the dried powder was calcined at different temperatures (150-450ºC) in order to achieve the desired crystal structure and mesopore size distribution. The samples were labeled as M-Co-X where X is the final calcination temperature.

1.2.3. Catalyst Characterization

1.2.3.1. X-Ray Powder Diffraction Studies

The powder X-ray diffraction (XRD) studies were performed with a Rigaku Ultima IV diffractometer using Cu Kα (λ = 0.15406 nm) radiation. Beam voltage and beam current of 40 kV and 44 mA were used respectively. The data were collected in the 2 theta ranges, 2 to 8º for low angle (LA) XRD studies (scan rate = 0.5º/min.), and 5 to 75º for wide angle (WA) XRD studies (scan rate = 2.0º/min.). The XRD patterns of samples were collected on a glass sample holder. Determination of crystallite size of the cobalt oxide materials was done using the Debye-Scherer equation.

1.2.3.2. Scanning Electron Microscopy and Energy Dispersive X-ray Spectroscopy

Morphological characterization of the synthesized materials was done using a FEI Nova NanoSEM FE-SEM with a beam current of 1.0 mA and a Schottky emitter operating at 2.0 kV. FESEM sample preparation was done by suspending the samples in absolute ethanol and then a drop of the suspension was dispersed on Au coated silicon chips mounted onto stainless-steel sample holders with double-sided carbon tape. Prior to the analysis all the samples were dried under vacuum. The EDX analysis was done using an Oxford X-max80 EDX analyzer operating at an electron accelerating voltage of 10 kV.

1.2.3.3. Transmission Electron Microscopy and Focused Ion Beam Technology

Transmission electron microscopy (TEM) and high-resolution transmission electron microscopy (HRTEM) studies were done with a JEOL 2010 UHR FasTEM operating at an accelerating voltage of 200 kV, equipped with an energy dispersive X-ray analysis (EDS) system. The sample preparation was done by suspending the material in 2-propanol and then a drop of the suspension was placed onto a carbon-coated copper grid and allowed to dry under infrared light. Focused ion beam (FIB) technology was performed using a FEI Strata 400S dual beam FIB system.

1.2.3.4. N_2 Sorption Studies

The nitrogen sorption experiments were done using a Quantachrome Autosorb iQ_2 surface area system. Prior to the experiments all samples were degassed at 150°C for 12 h. The Brunauer−Emmett−Teller (BET) method was used to determine the specific surface area of samples.

1.2.3.5. Thermo Gravimetric Analysis

Thermal stability studies were conducted by thermogravimetric analysis (TGA) using a Hi-Res TGA 2950 thermogravimetric analyzer. The temperature ramp for TGA was 10ºC/min in nitrogen atmosphere.

1.2.3.6. X-ray Photoelectron Spectroscopy

XPS analyses were performed using a PHI model 590 spectrometer with multiprobes, using Al Kα radiation (λ=1486.6 eV) as the radiation source.

1.2.3.7. Temperature programmed oxidation-mass spectrometry

Temperature programmed oxidation (TPO)-mass spectrometry analyses were performed with a home-made set-up and an MKS-UTI PPT quadrupole mass spectrometer. Sulfided M-Co-250 (100 mg) was packed in a quartz tube and the tube was placed in a horizontal tubular furnace. The loaded sample was heated from room temperature to 700ºC with a 5ºC/min heating rate under a 200 sccm air/H_2 (1:1) gas mixture.

1.2.4. Sulfidation reactor and sulfur sorption capacity

The sulfur sorption experiments were carried out in the range from room temperature (RT) to 300 ºC. The laboratory scale sulfur sorption apparatus is shown in Scheme 1.1. The fixed bed tubular reactor made of quartz with an internal diameter of 2 mm was oriented vertically in a tube furnace with PID control. In each experiment, 0.05 g of mesoporous materials and 0.05 to 0.20 g of commercial materials were packed in the reactor supported by quartz wool. A J-type thermocouple was placed at the top of the sorbent bed. Prior to each experiment, the sorbent was heated to the analysis temperature and held for 1 hr with a He flow of 36 SCCM. Gaseous samples were analyzed for sulfur using the analytical comprised of a SRI 8610C GC equipped with a GS-GasPro capillary

column (30 m × 0.32 mm I.D.) and a flame photometric detector (FPD). Helium served as the carrier gas and a 10 port sampling valve with an electronic actuator was used to make automatic injections into the GC every 10 min. Tubing and fittings were stainless steel throughout. The flow rates, feed, and composition were controlled using mass flow controllers (MFCs) (MKS model 1479A, 20 SCCM ± 1% full scale and Alicat Scientific, 200 SCCM ± 0.2 % full scale). The sulfidation reactions were carried out using a certified gas mixture (Scott Specialty Gases, 1 % H_2S in He) and the weight hourly space velocity was fixed at ~ 60 L h^{-1} g^{-1}.

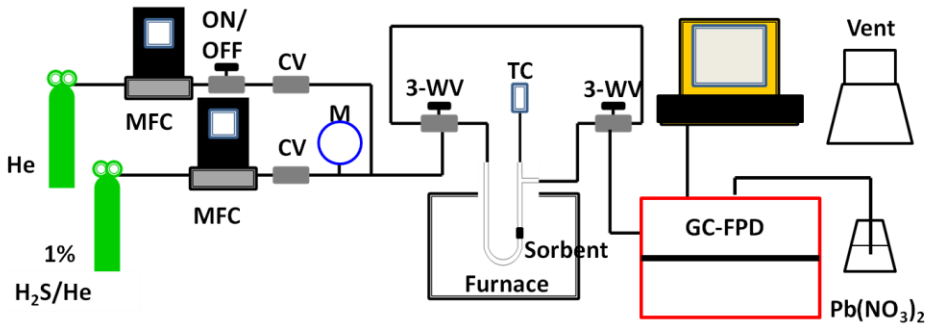

Scheme 1.1. Schematic representation of the experimental set-up[a]

[a]GC: Gas chromatograph, FPD: Flame photometric detector, MFC: Mass flow controller, TC: Thermocouple, 3WV: 3-Way valve, CV: Check valve, M: Manometer.

The sulfur sorption capacities (SC) of materials sulfided at different temperatures were calculated according to the Eq. 1.2.

$$\mathrm{SC}\left(\frac{\text{g sulfur}}{100\ \text{g sorbent}}\right) = \mathrm{WHSV} \times \left[\frac{\mathrm{M}}{\mathrm{V_{mol}}} \times \int_0^t (\mathrm{C_{in}} - \mathrm{C_{out}})\mathrm{d}t\right] \qquad (2)$$

Where WHSV is weight hourly space velocity in mL h^{-1} g^{-1}, M is the atomic weight of sulfur (32 g mol^{-1}), V_{mol} is the molar volume in L mol^{-1} under standard

conditions of 298 K and 1 atm (24.5 L mol^{-1}), C_{in} and C_{out} are the inlet and outlet concentrations (%), respectively, and t is the breakthrough time (BT) in hours. The BT is defined as the time when the outlet concentration reached 50 ppm.

1.3. Results

1.3.1. Physiochemical properties of commercial and mesoporous cobalt oxide materials

Figure 1.1a shows the low-angle powder X-ray diffraction (PXRD) lines for commercial (C-Co) and mesoporous cobalt oxide materials (M-Co-X, where X=150, 250, 350, and 450ºC) heated to different final temperatures (150 to 450^{o}C). The low angle diffraction lines were observed only for M-Co-150, M-Co-250, and M-Co-350 indicating the presence of an ordered mesostructure. The low angle diffraction line positions are almost the same for M-Co-150 and M-Co-250 (9.6 and 9.1 nm, respectively) but shifted to 11.8 nm by increasing the final heat treatment to 350ºC (Table 1.1). The commercial cobalt oxide and M-Co-450 did not show any low angle diffraction.

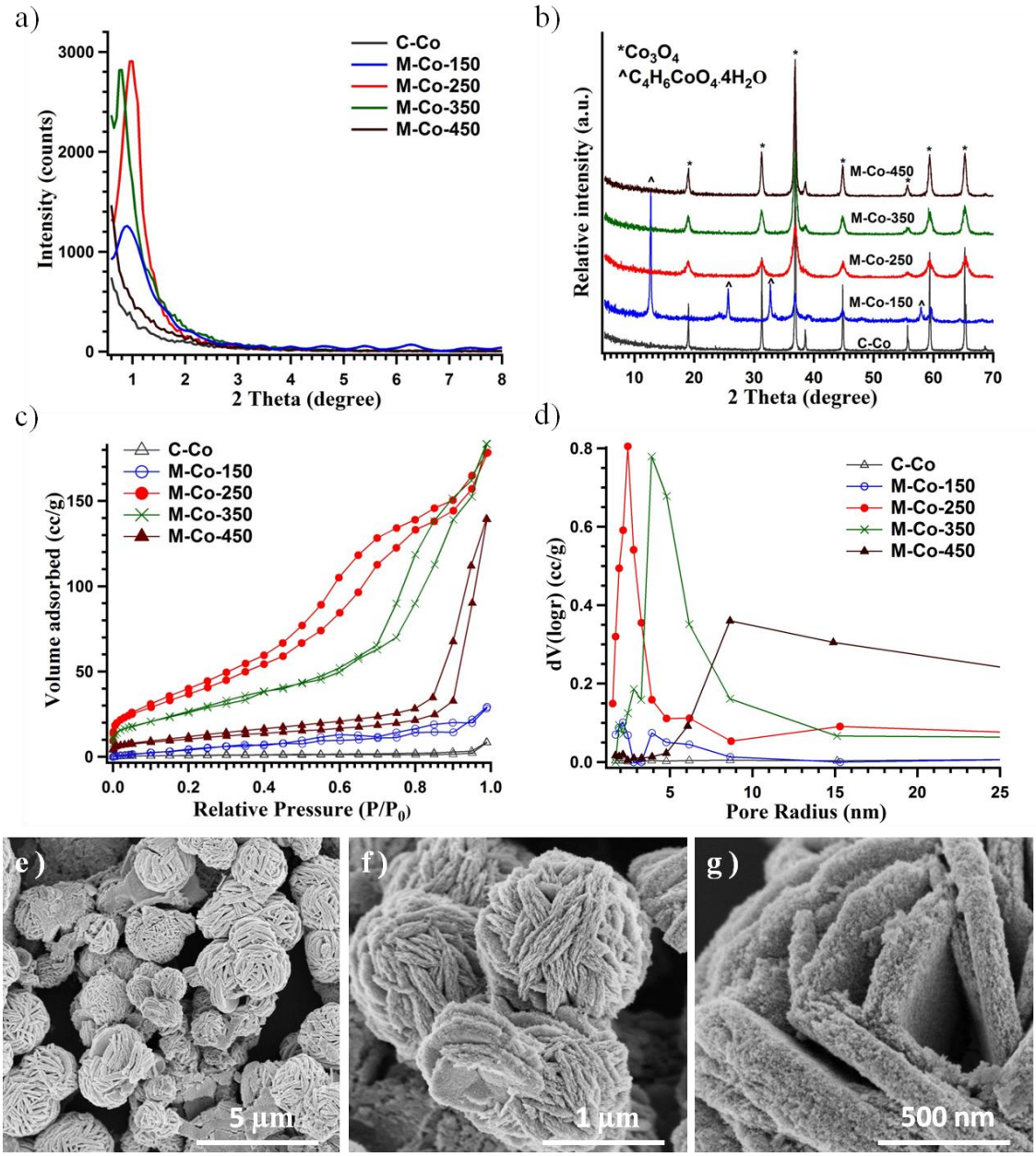

Figure 1.1. (a) Low angle and (b) High angle PXRD patterns (c) Nitrogen sorption isotherms and (d) BJH desorption pore size distributions of commercial cobalt oxide (C-Co) and mesoporous cobalt oxides (M-Co-X, X=150, 250, 350, 450ºC) (e) Low resolution and (f), (g) high resolution FESEM images of M-Co-

250 which contains micron sized openings which enhances the diffusion of reactant species.

The wide-angle PXRD pattern of M-Co-150 was clearly different from those observed for the commercial cobalt oxide and other M-Co-X materials (Figure 1.1b). The diffraction lines of the M-Co-150 material can be assigned to cobalt acetate hydrate, $C_4H_6CoO_4 \cdot 4H_2O$ (ICSD no. 00-025-0372) without any impurity peaks. The PXRD patterns of other M-Co-X could be indexed to the cubic phase of Co_3O_4 (ICSD no. 01-071-4921). The wide angle PXRD lines intensities were gradually increased as the calcination temperature was increased from 250 to 450ºC. However, the intensities of diffraction lines for commercial cobalt oxide were the highest; hence they have the highest crystallinity.

Figure 1.1c shows the N_2 sorption isotherms of mesoporous cobalt oxides. M-Co-250 and M-Co-350 materials showed characteristic Type IV adsorption isotherms suggesting an ordered mesoporous structure (Figures 1.1c and 1.1d). Commercial cobalt oxide has the lowest surface area (3 m^2/g). M-Co-150 shows the lowest BET surface area (23 m^2/g) among the M-Co-X materials but increased to 143 m^2/g when the calcination temperature was raised (250ºC). However, the surface area decreases upon further increase of the calcination temperature. M-Co-350 and M-Co-450 have surface area values of 99 and 38 m^2/g, respectively (Table 1.1). The change in Barrett-Joyner-Halenda (BJH) desorption pore volumes also follow a similar pattern, whereas, commercial cobalt oxide (0.01 cc/g) and M-Co-150 (0.05 cc/g) have the lowest pore volumes.

M-Co-250 shows the highest pore volume of 0.30 cc/g and decreased to 0.21 cc/g when the calcination temperature was increased to 450ºC (M-Co-450) (Table 1.1). On the other hand, BJH desorption pore diameter increases (from 3.4 to 17.2 nm) in the order of its non porous material, M-Co-150, M-Co-250, M-Co-350, and M-Co-450 (Table 1.1). Figure 1.1e shows the low resolution field-emission scanning electron microscopy (FESEM) images for M-Co-250 where spherical particles are sized between 1.4-2.8 µm. As shown in Figures 1.1f and 1.1g, these particles contain micron sized openings which enhance the diffusion of reactant species.

Table 1.1. Structural parameters of mesoporous cobalt oxide materials before and after sulfidation.

Material	PXRD Low-angle peak position (nm)	BET Surface area (m^2/g)	BJH Des. pore diameter (nm)	BJH Des. pore volume (cm^3/g)	Crystallite size (nm)
M-Co-150	9.6	23	4.2	0.05	11.1
M-Co-250	9.1	143	4.9	0.30	9.3
M-Co-350	11.8	99	7.6	0.28	12.8
M-Co-450	NA	38	17.2	0.21	19.7
C-Co	NA	3	3.4	0.01	63.1
M-Co-250-S25*	NA	98	3.8	0.16	3.5
M-Co-250-S100*	NA	71	3.4	0.09	5.1
M-Co-250-S175*	NA	62	3.8	0.06	2.3
M-Co-250-S200*	10.3	82	3.4	0.13	5.7

NA = Not applicable
***SX =** Sulfided at XºC

1.3.2. Desulfurization performances of commercial and mesoporous cobalt oxide materials

The breakthrough curves for commercial cobalt oxide (C-Co) and M-Co-X materials are presented in Figure 1.2a. The temperature inside the catalyst bed was maintained at 200ºC throughout the process. The C-Co showed the lowest BT of 0.28 h. The mesoporous cobalt oxide materials have BT times of 1.06, 17.02, 17.80, and 5.69 h for M-Co-150, M-Co-250, M-Co-350, and M-Co-450, respectively. Sulfur sorption capacities were determined according to Eq. 2 and are presented in Figure 1.2b. The sulfur sorption capacity varied from 1.4 to 69.2 g S/ 100 g sorbent where commercial cobalt oxide had the lowest (1.4 g S/ 100 g sorbent) and M-Co-250 and M-Co-350 showed the highest (66.7 and 69.2 g S/ 100 g sorbent, respectively). M-Co-150 and M-Co-450 show moderate sulfur sorption capacities; 4.3 and 22.2 g S/ 100 g sorbent, respectively.

Figure 1.2c shows the breakthrough curves for M-Co-250 sulfided at different temperatures ranging from room temperature (25°C) to 250ºC. Interestingly, M-Co-250 showed a significant BT (3.44 h) even at room temperature. When the sulfidation temperature was gradually increased up to 175°C, the BT also increased from 3.44 to 16.72 h and then remained almost the same (BTs of 17.05 and 17.58 h at 200°C and 250°C, respectively). The sulfur sorption capacities of M-Co-250 at different temperatures are demonstrated in Figure 1.2d which follow the same trend as the BTs. At RT M-Co-250 showed the lowest sulfur sorption capacity of 13.4 g S/100 g sorbent. The capacity increased

up to 65.0 g S/ 100 g sorbent at 175°C. At 200 and 250°C sulfur sorption capacities of 66.7 and 68.9 g S/ 100 g sorbent were observed, respectively.

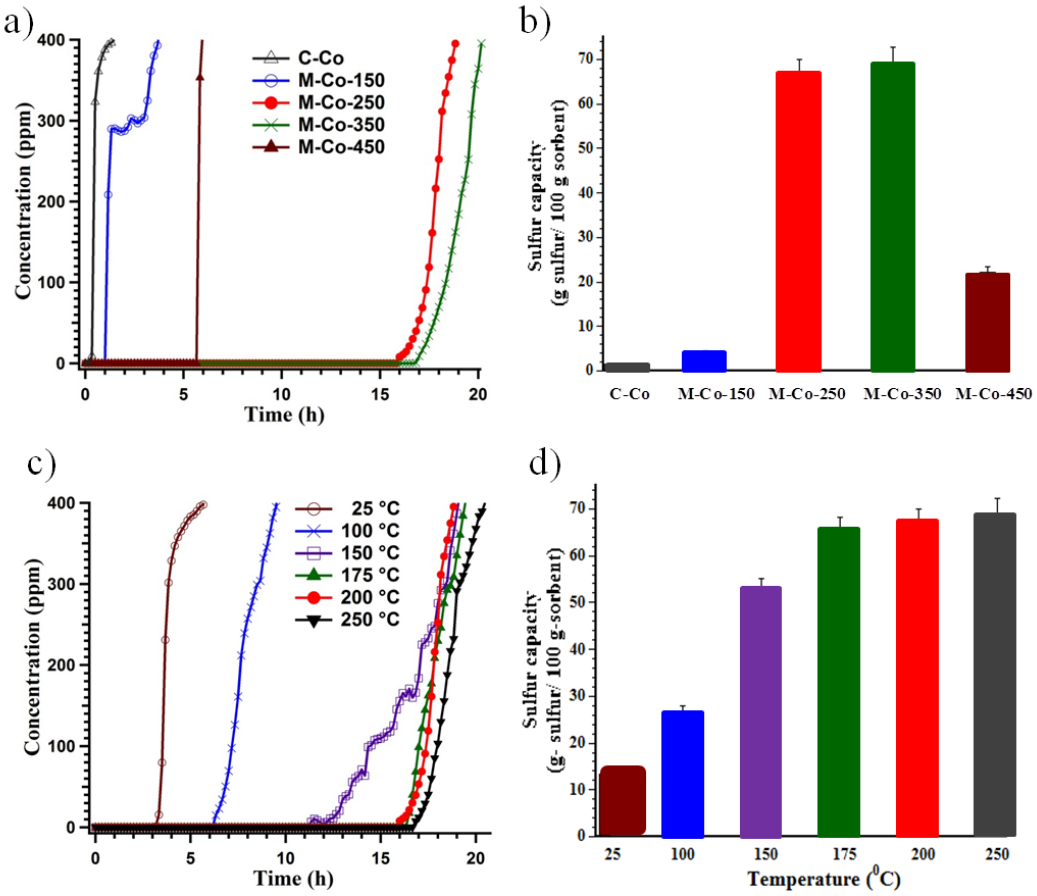

Figure 1.2. (a) Breakthrough curves and (b) Sulfur sorption capacities of commercial cobalt oxide (C-Co) and mesoporous cobalt oxides (M-Co-X, X=150, 250, 350, 450ºC) after sulfidation at 200 ºC. Mesoporous cobalt oxide materials calcined at 250 and 350ºC show the highest breakthrough times and the highest sulfur sorption capacities. (c) Breakthrough curves and (d) Sulfur sorption capacities of mesoporous cobalt oxide (M-Co-250) after sulfidation at different temperatures. Mesoporous cobalt oxide materials sulfided at temperatures above

175°C show the highest breakthrough times and the highest sulfur sorption capacities.

1.3.3. Comparison of physiochemical properties of M-Co-250 before and after sulfidation at 200ºC

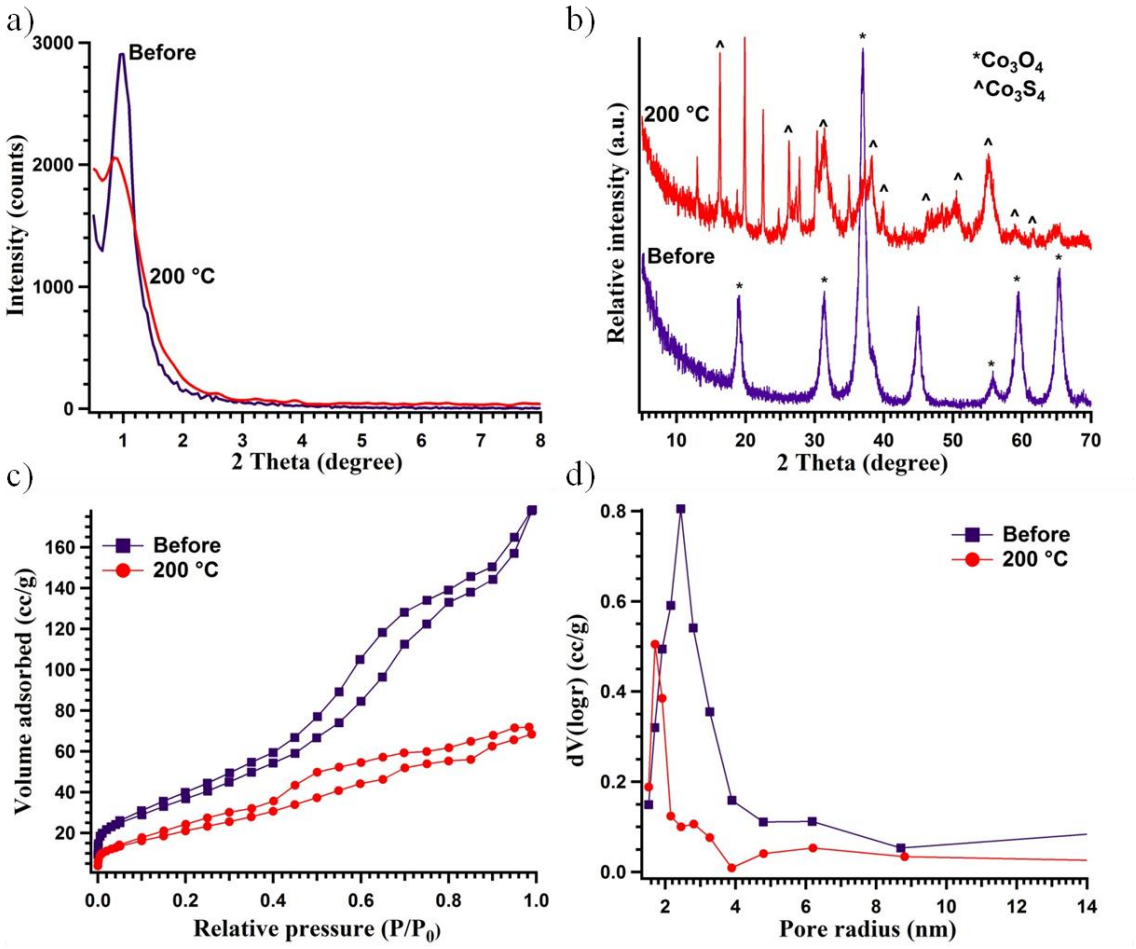

Figure 1.3. (a) Low angle PXRD patterns (b) High angle PXRD patterns (c) Nitrogen sorption isotherms and (d) BJH desorption pore size distributions of mesoporous cobalt oxide (M-Co-250) before and after sulfidation at 200 °C. Cobalt oxide is converted to cobalt sulfide retaining its mesoporous nature.

Due to the presence of a low angle diffraction line, the low-angle PXRD studies suggest that the mesoporosity of M-Co-250 was retained even after sulfidation at 200°C. A remarkable observation is that during desulfurization, the low-angle diffraction line position of M-Co-250 shifted from 9.1 to 10.3 nm (Figure 1.3a). As shown in Figure 1.3b, upon sulfidation at 200°C most of the original cobalt oxide PXRD peaks disappeared. Instead cobalt sulfide peaks (ICSD no. 01-074-6715) immerged along with a few unassigned peaks. Figure 1.4 shows the wide-angle PXRD patterns for M-Co-250 sulfided at different temperatures. When the sulfidation temperature was gradually increased, the intensities of peaks assigned for cobalt oxide were gradually decreased while those for cobalt sulfide are gradually increased. These observations suggest that most of the oxygen in the cobalt oxide structure was replaced by sulfur to give a mesoporous cobalt sulfide structure.

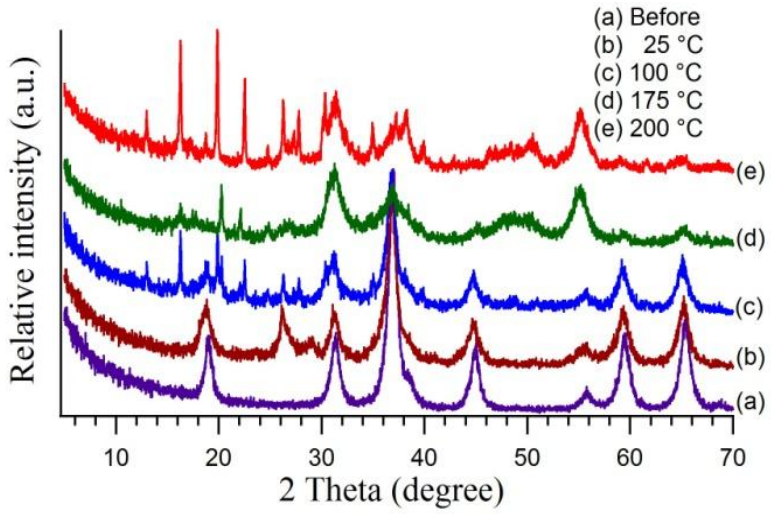

Figure 1.4. Wide-angle PXRD patterns of (a) M-Co-250 and after sulfidation at (b) 25ºC (c) 100ºC (d) 175ºC and (e) 200ºC.

The characterization of surface properties of the sulfided materials is shown in Figures 1.3c and 1.5a. The observed N_2 sorption isotherms for all sulfided M-Co-250 at all the temperatures give characteristic Type IV adsorption isotherms (Figure 1.5a), indicating the existence of a mesoporous structure. However, M-Co-250 material sulfided at 200ºC adsorbed the highest volume of N_2 gas among the sulfide materials and its isotherm shows the closest relationship in shape to that of its unsulfided counterpart (Figure 1.3c). The pore-size distributions for each of the sulfided M-Co-250 materials are given in Figure 1.5b and all the materials showed monomodal pore sizes, in the range of 3.4-3.8 nm. However, the average pore sizes of all the sulfided materials were lower than that of the unsulfided M-Co-250 (4.8 nm). The M-Co-250 sulfided at 200°C showed the highest porosity and the most uniform pore size distribution. The smaller pore size after sulfidation might be due to increase in size of nanoparticles during the sulfidation (Figure 1.3d).

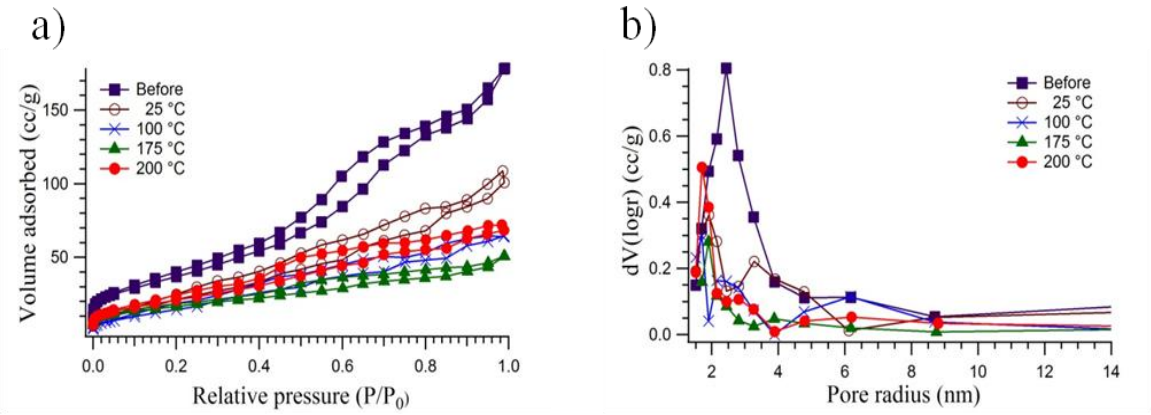

Figure 1.5. (a) Nitrogen sorption isotherms and (b) BJH pore size distributions of M-Co-250 before and after sulfidation at different temperatures.

The particles were spherical in shape and contain micron sized openings in the structure. However, the particle sizes were slightly increased (1.6-3.0 µm). Furthermore, Figure 1.6a shows that the sizes of the openings in the material also have increased compared to Figure 1.1g. Figure 1.6 shows the a) FESEM image, and b) Co c) S d) O FESEM-EDX elemental map data obtained for M-Co-250 sulfided at 200ºC. The cobalt oxide aggregate shown in the images clearly demonstrates the high amount of sulfur present in the material with respect to oxygen. The relative amount of oxygen is much lower compared to cobalt and sulfur, indicating that the oxygen in the cobalt oxide structure is replaced by sulfur. The presence of sulfur in the sulfided material was also analyzed by FESEM-EDX line analysis from point A to B (Figure 1.7a). As Figure 1.7b shows both cobalt and sulfur signals are high while the oxygen signal is very low in intensity.

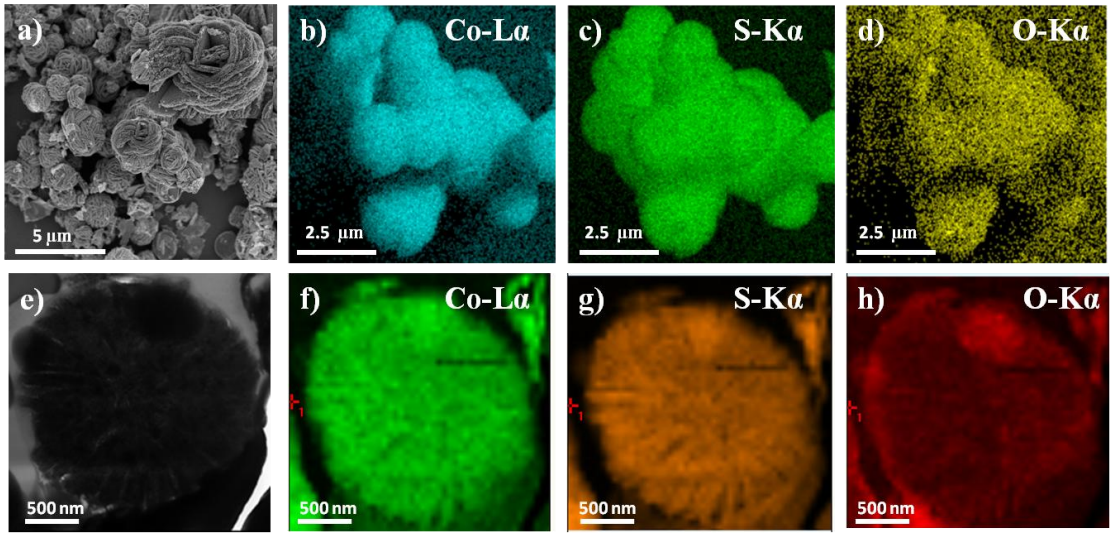

Figure 1.6. (a) Low resolution and High resolution (inset) FESEM images, FESEM-EDX elemental maps for (b) Co, (c) S, and (d) O, (e) TEM image, and

FETEM-EDX elemental maps of the cross-sectional view of isolated microsphere for (f) Co (g) S (h) O for mesoporous cobalt oxide (M-Co-250) after sulfidation.

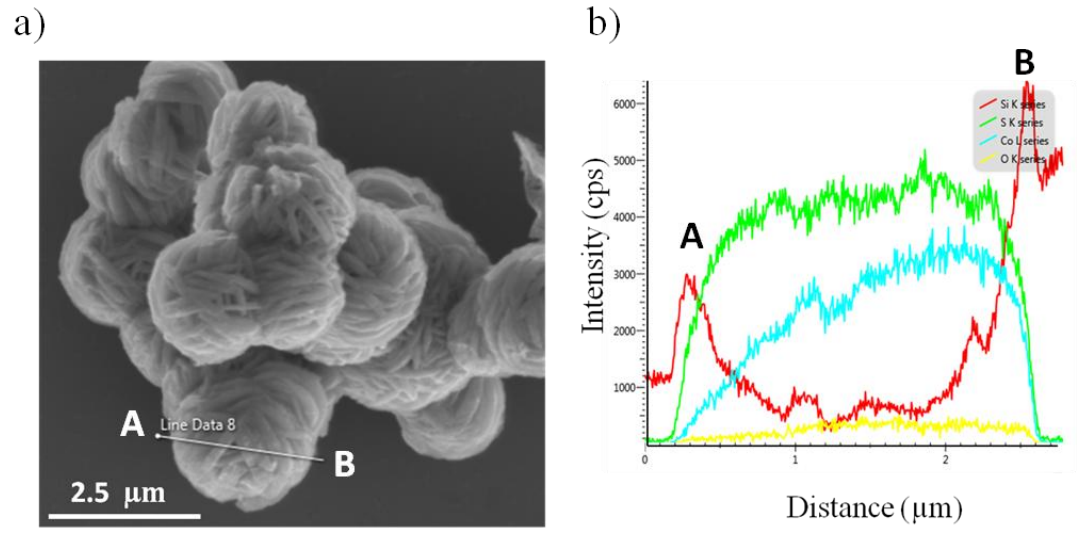

Figure 1.7. (a) FESEM image of M-Co-250 after sulfidation at 200ºC (b) FESEM-EDX line analysis from point A to B for cobalt, oxygen, sulfur and silicon.

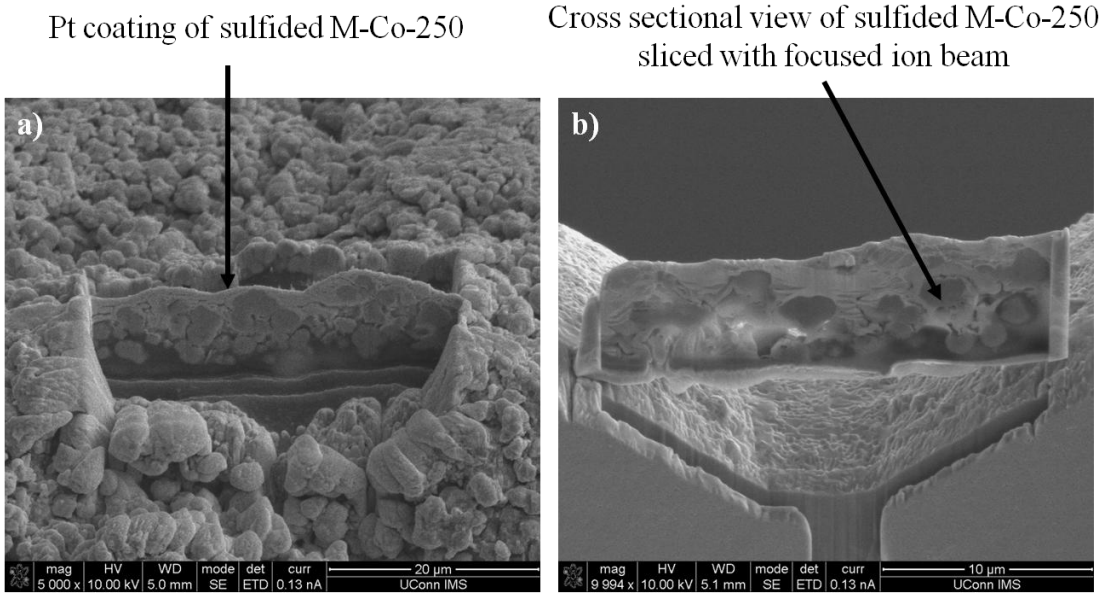

Figure 1.8. FESEM-FIB images of (a) Pt coating and (b) cross sectional view of M-Co-250 sulfided at 200ºC.

However, FESEM-SEM analysis gave no clue about the fractional coverage of sulfur in the mesoporous cobalt oxide particle. Therefore, the cross-section of a single particle was analyzed by HRTEM and FETEM-EDX. Figure 1.8a shows the platinum coated sulfided M-Co-250 microspheres and Figure 1.8b shows the vertically sliced mesoporous cobalt oxide material by focused ion beam (FIB) methods where the cross sections of microspheres are exposed. As shown in Figure 1.6e, the HRTEM image cross section of the single M-Co-250 microsphere suggests the idea of an interconnected mesoporous structure. Figures 1.6f-h show the elemental maps for the cross section of sulfided M-Co-250 microspheres which were obtained by FETEM-EDX map analysis and they provide clear evidence for the extremely high fractional coverage of sulfur inside the microspheres. On the other hand, the elemental analysis for oxygen shows that its abundance is very low inside the microsphere with respect to those for cobalt and sulfur. However, a slightly high abundance of oxygen was observed closer to the surface of the microsphere. These data suggest that hydrogen sulfide gas not only reaches all the particles in an aggregate, but also shows a very high degree of diffusion inside the mesopores. The chemical fate of sulfur in the sulfided materials was analyzed with XPS studies (Figures 1.9a and 1.9b) and the major species is S^{2-} (162.0, 163.4 eV) which exists as Co_3S_4. In addition, sulfur is present in the form of elemental sulfur (164.7, 166.6 eV), and SO_4^{2-} (168.9, 170.5 eV).

Figure 1.10a shows the TGA analysis data for M-Co-250 and the material sulfided at 200°C, both under air and nitrogen. The unsulfided M-Co-250 shows a high thermal stability until 800°C. However, when the sulfided material was analyzed with air, two slight drops in weight percent were seen; one drop of 5% from room temperature to 120ºC and another of 2.5% from 120 to 340ºC. The mass then increased until 760ºC followed by a drastic weight drop of 37% and this was observed during the oxidation of cobalt sulfide due to the formation of intermediate compounds in the temperature range of 340-760ºC. Under inert atmosphere (N_2), the same pattern was followed until 460ºC and then cobalt sulfide starts to get reduced. Removal of trapped sulfur and sorbent structure regeneration was studied by TPO. At around 395ºC O_2 was consumed and SO_2 was evolved (Figure 1.10b). No other gases were evolved between room temperature and 700°C. The sulfur sorption capacity of the regenerated M-Co-250 was tested at 200°C. Interestingly, this material showed a sulfur sorption capacity of 33.7 g S/100 g sorbent after regeneration at a high temperature as 400°C under air (Figure 1.11).

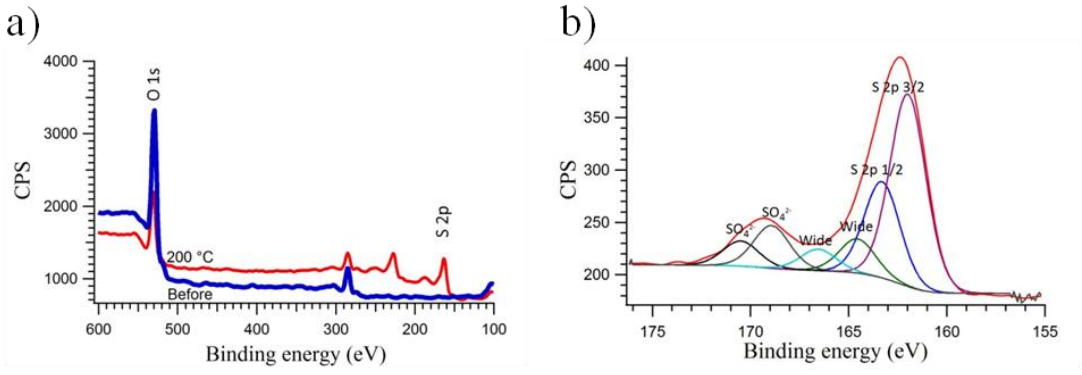

Figure 1.9. XPS data (a) before and after sulfidation at 200ºC and (b) S 2p region of sulfided M-Co-250.

1.3.4. Desulfurization activities of other mesoporous (UCT) materials

Other mesoporous metal oxides (UCT materials), Cr_2O_3, CuO, Mn_2O_3, and Fe_2O_3 were synthesized by the same synthetic method as M-Co-X materials according to the procedure of Poyraz et al. and they were also analyzed for their potential applications as desulfurization sorbents (M-Y-X, where Y represents the metal and X represents calcinations temperature). Desulfurization by their nonporous counterparts were also studied as control experiments. All the studied mesoporous materials showed significantly high specific capacities compared to the nonporous materials at 200°C. As Table 1.2 shows mesoporous Mn_2O_3 (M-Mn-250) showed the highest activity with a sulfur sorption capacity of 43.1 g sulfur/100 g sorbent, while mesoporous Cr_2O_3 (M-Cr-250) showed the lowest activity (19.6 g S/100 g sorbent). Interestingly, their desulfurization performances were 2 (by M-Fe-250)-200 (by M-Mn-250) times higher than those obtained by the nonporous metal oxides (C-MO_x). Mesoporous Co lies in between the hard bases and soft bases in the periodic table, showing considerably high specific capacities compared to other mesoporous metal oxides. Being neither a strong hard base nor soft base, Co can easily break Co-O bonds and make Co-S bonds. Moreover, that helps in regenerating the sorbent by breaking Co-S bonds at low temperatures.

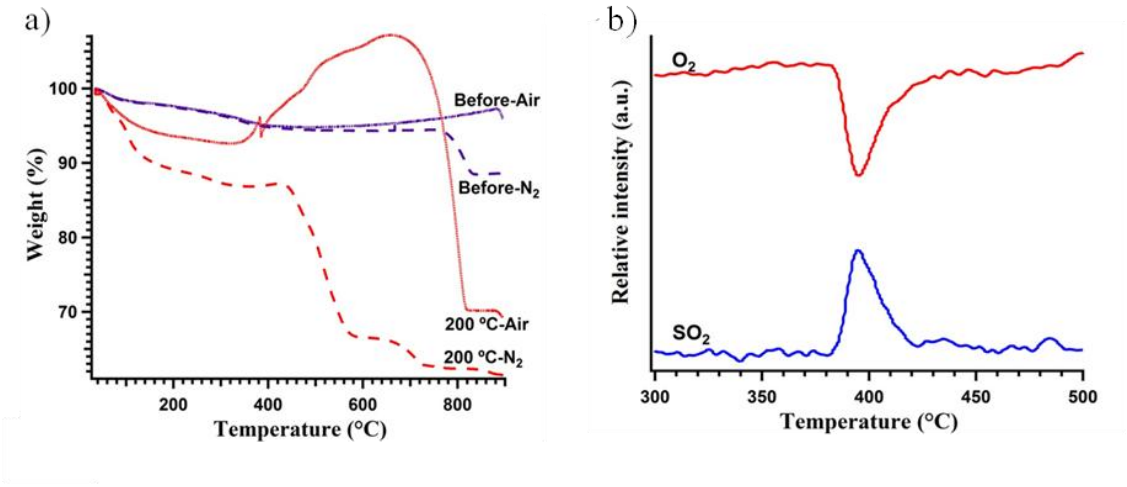

Figure 1.10. (a) Thermogravimetric analysis of mesoporous cobalt oxide calcined at 250ºC before and after sulfidation and (b) Temperature programmed oxidation (TPO) of mesoporous cobalt oxide after sulfidation.

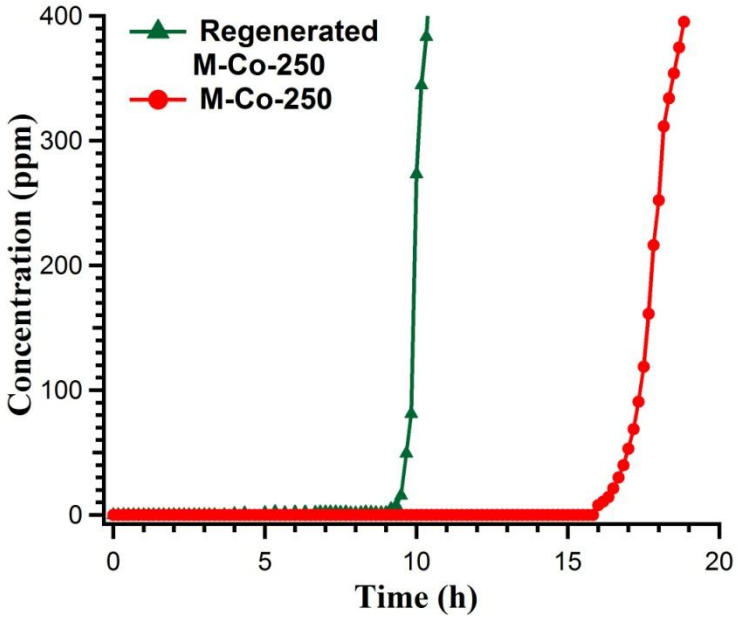

Figure 1.11. Breakthrough curves of fresh M-Co-250 and regenerated M-Co-250 for sulfidation at 200°C. The mesoporous cobalt oxide can be regenerated at 400°C under air without a significant loss in its sulfur sorption capacity.

Table 1.2. The sulfur sorption capacities of mesoporous and nonporous MO_x materials

MO_x	Nomenclature	Sulfur capacity (g S/100 g sorbent)
Meso-Cr_2O_3 (M-Cr-250)	UCT-37	19.6
Meso-CuO (M-Cu-250)	UCT-11	24.6
Meso-Mn_2O_3 (M-Mn-250)	UCT-1	43.1
Meso-Fe_2O_3 (M-Fe-250)	UCT-5	24.8
C-Cr_2O_3	NA	2.6
C-CuO	NA	1.3
C-Mn_2O_3	NA	0.2
C-Fe_2O_3	NA	11.0

1.4. Discussion

The well ordered mesoporous cobalt oxide materials were synthesized by carefully controlling the nature of the reaction medium and the interactions between the reagents as proposed in the literature.[27-32] In contrast to the traditional synthetic routes for the preparation of mesoporous metal oxides, the mesoporous materials prepared by the inverse micelle packing method in this study (UCT materials) consist of a low angle XRD peak where its position corresponds to the average sizes of the nanoparticles (Figure 1.1a).[27] The intraparticle voids of the nanoparticles connect with each other to form the mesoporous structure. The commercial cobalt oxide contains no mesoporous structure. When the calcination temperature is increased to 250ºC the sizes of the nanoparticles, hence the sizes of the interparticle voids for M-Co-350,

increase due to the sintering of Co_3O_4 nanoparticles. This observation is in good agreement with the BJH pore size distribution data where a concomitant variation in the pore diameter is observed with increasing the calcination temperature. When the calcination temperature is further increased to 450ºC the mesostructure collapses and no low angle peak is observed. As shown in Figure 1.1b, the Co_3O_4 phase is formed via a hydrated cobalt acetate phase. Once Co_3O_4 phase is formed its crystalline nature increases with temperature as explained in Figure 1.1b. However, commercial cobalt oxide possessed a higher crystallinity compared to all the M-Co-X materials. The effect of nanocrystallinity is well reflected by the N_2 sorption data. The lower the crystallite size is, the higher the exposed surface area is, and hence the higher the volume of gas adsorbed. In addition, the commercial cobalt oxide (C-Co) did not show a Type IV isotherm indicating the lack of mesoporosity (Figures 1.1c and 1.1d).[27] Table S1 shows that the surface area place an important role in determining the sulfur sorption capacity. Therefore, the presence of surface exposed particles and interconnected intraparticle voids are responsible for having high sulfur sorption capacities by mesoporous cobalt oxide materials compared to the non porous cobalt oxide.

As shown in Figures 1.2a and 1.2b, M-Co-250 and M-Co-350 materials gave significantly high BTs and sulfur sorption capacities at temperatures as low as 200ºC in contrast to the materials published in the literature where high temperatures (>400 ºC) are required in order to obtain considerable sulfur sorption capacities.[20,22,32-36] However, the materials are in good agreement with

the data observed in the literature in terms of the shape of the breakthrough curve.[13] Here, although the M-Co materials are highly active in sulfur sorption and the conversion of oxide to sulfide continues after the breakthrough, once BT is obtained, they lose the ability to remove H_2S efficiently. The slopes of the breakthrough curves depend on the nature and the surface morphology of the sorbent. This effect is well reflected in Figure 1.2a, where M-Co-250 and M-Co-350, which possess very high mesoporosity, have breakthrough curves with lower slopes compared to the other materials. Hence, in these materials sulfidation after the BT is more effective compared to materials with either low or no porosity.[25,26]

The sulfidation is a radial property and the extent of sulfidation of a material is controlled by the ability of the H_2S molecules to diffuse inside the material. Therefore, the conversion of the oxide to the sulfide is governed by two major factors. The first is the temperature at which the sulfidation takes place, where the kinetic energy of the H_2S molecule, hence the diffusion rate is increased with temperature. The metal oxide to metal sulfide conversion with temperature could be seen in the sequence of PXRD patterns in Figure 1.4 and total conversion is obtained by 200ºC (Figure 1.3b).[37,38] The second factor involves surface properties of the material. The higher the amount of surface particle is, the easier the H_2S molecules to reach all the particles in an aggregate. This is clearly reflected in the FESEM-EDX data presented in Figures 1.6a-d. The EDX elemental maps show that H_2S reaches all the particles in an aggregate and O is replaced by S. This emphasizes the role of mesoporosity.

Hence, these materials can be considered as a surface active sorbent rather than a bulk material. Another important property of the sorbent is its high porosity (Figures 1.1e and 1.1f). As seen in Figure 1.6e, the cross section of an individual particle shows that the material consists of interconnected pores which is a critical factor in determining the extent of diffusion of H_2S molecules inside the particles.[25] This phenomenon is well supported by the FETEM-EDX maps shown in Figures 1.6f-h where sulfur has a uniform distribution throughout the particle while oxygen is mainly seen on the particle surface due to adsorbed species between the time of sulfidation and the time of FETEM-EDX analysis. This is further shown by the FESEM-EDX line analyses across a single particle (Figures 1.7a and 1.7b) where oxygen amount is greatly suppressed by sulfur.

The morphology evolution after sulfidation for M-Co-250 (Figure 1.6a) showed that sintering is not taking place; hence, the mesoporosity was retained. Interestingly, the LA-PXRD data agree with the fact of retaining the mesostructure by the existence of a low angle diffraction line after sulfidation.[27] However, the crystal structure analysis shows that the low-angle peak position is increased upon sulfidation indicating an increase in the particle sizes as the crystal radius of S^{2-}(1.70 Å) is larger than that of O^{2-} (1.21 Å). The N_2 sorption data further suggest the mesoporous nature of the sulfide materials with the existence of a Type IV isotherm, and a uniform BJH pore size distribution curve in which the pore diameter is reduced upon sulfidation due to swelling of individual particles (Figures 1.3c and 1.3d).

Although the weight loss of the fresh sample under air is negligible, under N_2 atmosphere a weight drop around 800ºC is observed due to the reduction of the material (Figure 1.10a).[13] The initial mass loss of the sulfided material both under air and nitrogen might be due to adsorbed moisture and physisorbed H_2S. However, the weight increase of the sulfide material under air is due to formation of cobalt sulfate. This might take place by the reaction between SO_2 and the regenerated material (Co_3O_4).[13] The idea was confirmed by the TPO data (Figure 1.10b) where sulfur dioxide is evolved (395ºC) just before the weight increase starts in the TGA data.

Other mesoporous metal oxides synthesized with the same approach as UCT mesoporous materials, were tested for low temperature (200ºC) H_2S removal under the same conditions and showed relatively low H_2S uptakes compared to M-Co materials (Table 1.2). However, the UCT materials showed significantly higher activities compared to their analogous nonoporous materials due to their mesostructure consists of interconnected intraparticle voids which increases the diffusion of $H_2S_{(g)}$.[14,39,40] Based on the high activity data observed for mesoporous Mn_2O_3 materials, further studies are being carried out in our laboratories.

1.5. Conclusion

The mesoporous cobalt oxide materials synthesized by the inverse micelle templating method were used as sorbents for the removal of H_2S at low

temperatures (25-250ºC). The mesoporous materials showed superior activity even at room temperature and reached 100% theoretical sulfur capacity (52.5 g S/100g sorbent) at a very low temperature as 150ºC. The sulfur sorption capacity increased as the sulfidation temperature was increased and the maximum sulfur capacities (65-68.9 g S/100g sorbent) were reached in the range of 175-250ºC. According to the literature, even though the sulfidation at low temperatures is kinetically slow, the mesoporous cobalt oxide materials showed high sulfur capacities and reached high oxide to sulfide conversions. Other mesoporous materials (Cr_2O_3, CuO, Mn_2O_3, and Fe_2O_3) also showed superior activities compared to their nonporous analogues (as high as 200 times). Based on the data observed, due to the presence of surface exposed particles and the interconnected intraparticle voids, the diffusion of H_2S in the sorbent is greatly enhanced providing high sulfur capacities.

References

(1). van der Drift, A.; van Doorn, J.; Vermeulen, J. W. Ten residual biomass fuels for circulating fluidized-bed gasification. *Biomass Bioenergy* **2001***, 20*, 45.

(2). Leppälahti, J.; Koljonen, T. Nitrogen evolution from coal, peat and wood during gasification: Literature review. *Fuel Process Technol* **1995***, 43*, 1.

(3). Torres, W.; Pansare, S. S.; Goodwin, J. G., Jr. Hot Gas Removal of Tars, Ammonia, and Hydrogen Sulfide from Biomass Gasification Gas. *Cat. Rev. Sci. Eng.* **2007***, 49,* 407.

(4). Cal, M. P.; Strickler, B. W.; Lizzio, A. A. High temperature hydrogen sulfide adsorption on activated carbon: I. Effects of gas composition and metal addition. *Carbon* **2000***, 38*, 1757.

(5). Habibi, R.; Rashidi, A. M.; Daryan, J. T.; zadeh, A. M. Study of the Rod-Like and spherical nano-ZnO morphology on H2S removal from natural gas. *Appl. Surf. Sci.* **2010***, 257*, 434.

(6). Meng, X.; de Jong, W.; Pal, R.; Verkooijen, A. H. M. In bed and downstream hot gas desulphurization during solid fuel gasification: A review. *Fuel Process Technol* **2010***, 91*, 964.

(7). Garces, H. F.; Galindo, H. M.; Garces, L. J.; Hunt, J.; Morey, A.; Suib, S. L. Low temperature H_2S dry-desulfurization with zinc oxide. *Microporous and Mesoporous Materials* **2010***, 127*, 190.

(8). Sethuraman, V. A.; Weidner, J. W. Analysis of sulfur poisoning on a PEM fuel cell electrode. *Electrochim. Acta* **2010***, 55*, 5683.

(9). Chung, J. B.; Chung, J. S. Desulfurization of using cobalt-containing sorbents at low temperatures. *Chemical Engineering Science* **2005***, 60*, 1515.

(10). Yang, H.; Cahela, D. R.; Tatarchuk, B. J. A study of kinetic effects due to using microfibrous entrapped zinc oxide sorbents for hydrogen sulfide removal. *Chemical Engineering Science* **2008***, 63*, 2707.

(11). Kuramochi, H.; Wu, W.; Kawamoto, K. Prediction of the behaviors of H2S and HCl during gasification of selected residual biomass fuels by equilibrium calculation. *Fuel* **2005***, 84*, 377.

(12). Cheah, S.; Carpenter, D. L.; Magrini-Bair, K. A. Review of Mid- to High-Temperature Sulfur Sorbents for Desulfurization of Biomass- and Coal-derived Syngas. *Energy Fuels* **2009***, 23,* 5291.

(13). Garces, H. F.; Espinal, A. E.; Suib, S. L. Tunable Shape Microwave Synthesis of Zinc Oxide Nanospheres and Their Desulfurization Performance Compared with Nanorods and Platelet-Like Morphologies for the Removal of Hydrogen Sulfide. *J. Phys. Chem. C* **2012***, 116,* 8465.

(14). Westmoreland, P. R.; Harrison, D. P. Evaluation of candidate solids for high-temperature desulfurization of low-BTU gases. *Environ. Sci. Technol.* **1976***, 10,* 659*.*

(15). Slimane, R. B.; Abbasian, Utilization of metal oxide-containing waste materials for hot coal gas desulfurization. J. *Fuel Process Technol* **2001***, 70*, 97.

(16). Ko, T.; Chu, H.; Liou, Y. A study of Zn–Mn based sorbent for the high-temperature removal of H_2S from coal-derived gas. *J. Hazard. Mater.* **2007***, 147*, 334.

(17). Flytzani-Stephanopoulos, M.; Sakbodin, M.; Wang, Z. Regenerative Adsorption and Removal of H_2S from Hot Fuel Gas Streams by Rare Earth Oxides. *Science* **2006***, 312*, 1508.

(18). Gibson, J. B., III; Harrison, D. P. The Reaction between Hydrogen Sulfide and Spherical Pellets of Zinc Oxide. *Ind. Eng. Chem. Proc. Des. Dev.* **1980***, 19,* 231.

(19). Lew, S.; Jothimurugesan, K.; Flytzani-Stephanopoulos, M. High-temperature hydrogen sulfide removal from fuel gases by regenerable zinc oxide-titanium dioxide sorbents. *Ind. Eng. Chem. Res.* **1989***, 28,* 535.

(20). Woods,M. C.; Gangwal, S. K.; Harrison, D. P.; Jothimurugesan, K. Kinetics of the reactions of a zinc ferrite sorbent in high-temperature coal gas desulfurization. *Ind. Eng. Chem. Res.* **1991***, 30,* 100.

(21). Bakker, W. J. W.; Kapteijn, F.; Moulijn, J. A. A high capacity manganese-based sorbent for regenerative high temperature desulfurization with direct sulfur production: Conceptual process application to coal gas cleaning. *Chem. Eng. J.* **2003***, 96*, 223.

(22). Wang, Z.; Flytzani-Stephanopoulos, M. Cerium Oxide-Based Sorbents for Regenerative Hot Reformate Gas Desulfurization. *Energy Fuels* **2005***, 19,* 2089.

(23). Kobayashi, M.; Shirai, H. High-Temperature Sulfidation Behavior of Reduced Zinc Ferrite in Simulated Coal Gas Revealed by in Situ X-ray Diffraction Analysis and Mössbauer Spectroscopy. *Energy Fuels* **2002***, 16,* 601*.*

(24). Zhang, R.; Huang, J.; Zhao, J.; Sun, Z.; Wang, Y. Sol−Gel Auto-Combustion Synthesis of Zinc Ferrite for Moderate Temperature Desulfurization. *Energy Fuels* **2007***, 21,* 2682*.*

(25). Sun, J.; Modi, S.; Liu, K.; Lesieur, R.; Buglass, J. Kinetics of Zinc Oxide Sulfidation for Packed-Bed Desulfurizer Modeling. *Energy Fuels* **2007***, 21,* 1863*.*

(26). Zevenhoven, C. A. P.; Yrjas, K. P.; Hupa, M. M. Hydrogen Sulfide Capture by Limestone and Dolomite at Elevated Pressure. 2. Sorbent Particle Conversion Modeling. *Ind. Eng. Chem. Res.* **1996***, 35,* 943*.*

(27). Poyraz, A. S.; Kuo, C-H.; Biswas, S.; King'ondu, C. K.; Suib, S. L. A general approach to crystalline and monomodal pore size mesoporous materials. *Nat. Commun.* **2013***, 4, 3952,* 1.

(28). Boettcher, S. W.; Fan, J.; Tsung, C., Shi, Q.; Stucky, G. D. Harnessing the Sol–Gel Process for the Assembly of Non-Silicate Mesostructured Oxide Materials. *Acc. Chem. Res.* **2007**, *40,* 784*.*

(29). Schu¨th, F. Non-siliceous Mesostructured and Mesoporous Materials. *Chem. Mater.* **2001**, *13,* 3184.

(30). Pahalagedara, M.N.; Pahalagedara, L. R.; Kuo, C-H.; Dharmarathna, S.; Suib, S. L. *Langmuir* **2014**, *30*, 8228.

(31). Pahalagedara, M. N.; Samaraweera, M. A.; Dharmarathna, S.; Kuo, C-H.; Pahalagedara, L. R.; Gascon, J. A.; Suib, S. L. Removal of azo dyes: Intercalation into sonochemically synthesized NiAl-Layered double hydroxide. *J. Phys. Chem. C* **2014**, *118 (31),* 17801-17809.

(32). Banerjee, S., Santhanam, A.; Dhathathreyan, A.; Rao, P. M. Synthesis of Ordered Hexagonal Mesostructured Nickel Oxide. *Langmuir* **2003**, *19,* 5522.

(33). Woods, M. C.; Gangwal, S. K.; Jothimurugesan, K.; Harrison, D. P. Reaction between hydrogen sulfide and zinc oxide-titanium oxide sorbents. 1. Single-pellet kinetic studies. *Ind. Eng. Chem. Res.* **1990***, 29,* 1160.

(34). Flytzani-Stephanopoulos, M.; Sakbodin, M.; Wang, Z. Regenerative Adsorption and Removal of H2S from Hot Fuel Gas Streams by Rare Earth Oxides. *Science* **2006***, 312*, 1508.

(35). Alonso, L.; Palacios, J. M. Performance and Recovering of a Zn-Doped Manganese Oxide as a Regenerable Sorbent for Hot Coal Gas Desulfurization. *Energy Fuels* **2002***, 16,* 1550.

(36). Pahalagedara, L. R.; Dharmarathna, S.; King'ondu, C. K.; Pahalagedara, M. N.; Meng, Y-T.; Kuo, C-H.; Suib, S. L. Microwave-assisted hydrothermal synthesis of α-MnO_2: Lattive Expansion via rapid temperature ramping and framework substitution *J. Phys. Chem. C* 2014, *118* (35), 20363–20373.

(37). Zhang, H.; Solomon, L. V.; Ha, D-H.; Honrao, S.; Hennig, R. G.; Robinson, R. D. $(NH_4)_2S$, a highly reactive molecular precursor for low temperature anion exchange reactions in nanoparticles. *Dalton Trans.* **2013**, *42*, 12596.

(38). Samokhvalov, A.; Tatarchuk, B. Characterization of active sites, determination of mechanisms of H2S, COS and CS2 sorption and regeneration of ZnO low-temperature sorbents: past, current and perspectives. J. *Phys. Chem. Chem. Phys.* **2011**, *13*, 3197.

(39). Dolan, M. D.; Ilyushechkin, A. Y.; McLennan, K. G.; Sharma, S. D. Sulfur removal from coal-derived syngas: thermodynamic considerations and review. *Asia-Pacific Journal of Chemical Engineering* **2012***, 7*, 1.

(40). Pahalagedara, L. R.; Sharma, H. N.; Kuo, C-H; Dharmarathna, S; Joshi, A.; Suib, S. L.; Mhadeshwar, A. B. Structure and oxidation activity correlations for carbon blacks and Diesel soot. *Energy Fuels,* **2012**, *26* (11), 6757-6764.

CHAPTER II. MICROWAVE ASSISTED HYDROTHERMAL SYNTHESIS OF α-MnO_2: LATTICE EXPANSION VIA RAPID TEMPERATURE RAMPING AND FRAMEWORK SUBSTITUTION.

2.1. Introduction

Manganese oxide octahedral molecular sieves are porous inorganic nanostructures,[1] with an excellent catalytic activity[2] due to their mixed valent lattice structure[3] consisting of Mn^{2+}, Mn^{3+} , and Mn^{4+} and they also possess good semiconducting properties.[4] Among the class of manganese oxide octahedral molecular sieve material (OMS), the most extensively studied is cryptomelane-type OMS material which is composed of edge shared MnO_6 octahedra forming a 2 × 2 (0.46 nm × 0.46 nm) 1-D tunnel structure[5] (Figure 2.1). OMS-2 material is environmentally benign and relatively cheap and has found a wide range of applications in the fields of environmental,[6] sustainable energy research,[7] battery materials,[8] gas sorption,[9] energy storage,[10] oxidation catalysis,[11] and pollution control.[6] The chemical composition of OMS-2 material is $KMn_8O_{16}\cdot nH_2O$, where Mn^{2+}, Mn^{3+}, and Mn^{4+} reside in the framework sites resulting in an average oxidation state of 3.8^+, while K^+ resides in the tunnel sites compensating the charge imbalance due to the reduction of Mn^{4+}.[2,12] Introduction of a metal ion/ metal ions, either into the OMS-2 tunnels or to the framework could be used to tune the structure, morphology, and lattice parameters, which offer novel chemical and physical properties.

Figure 2.1. Polyhedral representation of the crystal structure of α-MnO_2 type materials. The structure is viewed down the c-axis of the tetragonal unit cell. Potassium atoms are shown in grey and MnO_6 octahedra are shown in brown.

The morphology, chemical and physical characteristics, and hence the applications of OMS-2 materials also depend on the synthetic route. Chen et al. successfully prepared and characterized manganese oxide OMS-2 materials with different metal cations doped into the structure using a reflux method.[13] In this study an aqueous solution of the metal cation dopant (Cu^{2+}, Zn^{2+}, Ni^{2+}, Co^{2+}, Al^{3+}, or Mg^{2+}) was added to the refluxing mixture and these foreign metal cations mostly resided in the framework sites. In addition, Co has found to be at the highest levels (Co/ Mn atomic ratio = 0.097) inside the OMS-2 structure. However, this work suffers from low doping levels.

In another study, King'ondu et al. synthesized novel, multidoped cryptomelane self-assembled hollow nanostructures using Mo^{6+}, V^{5+}, Cu^{2+}, and Fe^{2+} as the dopant cations. Here, the authors were able to tailor the morphology, particle size, crystal system, and surface area of OMS-2 materials through

multiple substitutions using the reflux method.[14] Metal cation doped OMS-2 materials have also been used in specific applications, such as microwave field assisted synthesis of vanadium doped OMS-2 for Li-ion intercalation,[8] hydrothermal, and reflux synthesis of Ag–OMS-2 for electrochemical studies,[12] hydrothermal synthesis of Cu doped OMS-2 for their X-ray absorption and cyclic voltammetric studies,[10] increased thermal stability of Co and Sn doped OMS-2,[15] framework doping of Fe in cryptomelane tunnel structures for higher thermal stability and increased basic sites,[16] hydrothermal synthesis of In doped OMS-2 materials for electrocatalytic reduction of oxygen,[17] reflux synthesis of W-framework doped for OMS-2 for tuning conductivity,[18] higher valency ion (V and Nb) substitution into OMS-2 framework via an hydrothermal synthesis in order to obtain increased electrical resistivity,[19] and reflux synthesis of Mo doped OMS-2 materials for green decomposition of organic dyes.[20] However, the afore-mentioned studies have used longer reaction times (90 min to 4 days) at elevated temperatures (above 100 ºC) during the synthesis of the metal doped OMS-2 materials, therefore have high energy consumption.

Due to its wide applicability, short reaction times, and unique properties, microwave assisted synthesis routes have widely been used in the preparation of inorganic materials.[21-27] Unlike conventional oil bath heating, in microwave processing, an inverted temperature gradient takes place. The rapid dielectric heating is generated internally within the material due to applied microwave radiation with a commonly used frequency of 2.45 GHz.[22,24] Mohajerani et al. discussed the effect of kinetic conditions of the primary solution in determining

the final morphology of the products,[22] while Cheng et al. studied the increased crystal growth rates under microwave electromagnetic fields.[28] Researchers have achieved rapid temperature ramps in their syntheses by using microwave heating systems with sealed vessels.

During the synthesis of organic compounds using microwaves under sealed conditions, Gadye et al. discovered that faster heating rates can be obtained in the presence of ions in the reaction mixture.[27] Moreover, Liu et al. synthesized gold nanorods with a high aspect ratio influenced by the rapid microwave heating.[26] They also studied the relationship between the temperature ramp and the physical characteristics (size and the shape) of the gold nanoparticles. In 2010, Huang et al. introduced a rapid process to synthesize cryptomelane type pristine manganese oxide OMS material using microwave assisted hydrothermal (MWHY) techniques.[29] In their study, the synthesis was carried out at 200ºC and 15 bar in a very short reaction time (5 min), but most importantly, the temperature ramp and the pressure ramp were extremely high (200ºC/min and 15 bar/min, respectively) compared to those of conventional methods.

In this work, we report a facile synthesis of novel metal doped cryptomelane ([M]-K-OMS-2, where M denotes the dopant metal) self-assembled microwires synthesized via a rapid MWHY method. The effects of reaction temperature ramp are systematically studied and compared using a Biotage Initiator microwave apparatus and conventional heating methods. The microfibers have been synthesized by a template free reaction using Ag^{+}, Ce^{3+},

Co^{2+}, Cu^{2+}, Ni^{2+}, Sr^{2+}, V^{4+}, and Zn^{2+} as the dopant cations. In this work we have focused on the physiochemical characterization of the [Co]-K-OMS-2 materials and its catalytic activity in the oxidation of benzyl alcohol to benzyl aldehyde. Moreover, by altering the Co to Mn ratio, we observed a concomitant variance in the lattice structure. Gas phase H_2S desulfurization was used as a model experiment, in order to study the effects by the size of its one dimensional tunnel and the presence of dopants. Based on these observations we propose a technique which can be adopted for large scale synthesis of doped K-OMS-2 with controlled structural properties. The fundamental studies involving the impact of the tunnel size, and the growth direction, on the degree freedom of a guest molecule ($H_2S_{(g)}$) inside its 1-D tunnels are also discussed.

2.2. Experimental

2.2.1. Materials

Potassium sulfate, K_2SO_4, potassium peroxydisulfate, $K_2S_2O_8$, manganese(II) sulfate monohydrate , $MnSO_4 \cdot H_2O$, cobalt(II) nitrate hexahydrate, $Co(NO_3)_2 \cdot 6H_2O$ and other metal precursors were purchased from Sigma-Aldrich. The solvents used in this work were purchased from commercial sources. All reagents were purchased from Aldrich and used as received, unless otherwise indicated.

2.2.2. Catalyst Preparation

In a typical synthesis, K_2SO_4 (0.418 g, 0.2387 mol/L), $K_2S_2O_8$ (0.648 g, 0.2387 mol/L), $MnSO_4 \cdot H_2O$ (0.270 g, 0.159 mol/L), and a known amount of dopant precursor were dissolved in 10.0 mL of distilled, deionized water (DDW). The aqueous reaction mixture was prepared in a 20 mL quartz reaction vial equipped with a magnetic stirrer, and then sealed with a cap. The synthesis was carried out in the Biotage Initiator microwave synthesizer programmed to heat up to 200ºC with a hold time of 10 min. All *x*[M]-K-OMS-2 materials (where M stands for metal dopant including Ag, Ce, Co, Cu, Ni, Sr, V, and Zn while *x*, ranging from 0.05 to 1.00, stands for M to Mn initial molar ratio) were washed with DDW several times to remove any possible impurities and then dried at 120ºC for 24 h. Table S1 shows the precursors used for the syntheses.

2.2.3. Catalyst Characterization

2.2.3.1. X-Ray Powder Diffraction Studies

X-ray diffraction studies were carried out for the samples prepared to confirm the structure and phase purity using a Rigaku Ultima IV diffractometer with Cu Kα radiation (λ = 0.15406 nm). A beam voltage of 40 kV and beam current of 44 mA in a continuous scan mode with a scanning rate of 2.0 deg s^{-1} in the 2*θ range* from 5° to 70º was used. The phases identified using The International Center for Diffraction Data (ICDD) database.

2.2.3.2. Scanning Electron Microscopy and Energy Dispersive X-ray Spectroscopy

Morphologies of the materials were studied using Zeiss DSM 982 Gemini emission scanning microscope equipped with a Schottky Emitter at an accelerating voltage of 2 KV having a beam current of 1 mA. The samples were dispersed in ethanol then were coated on a silicon wafer and kept under vacuum overnight to dry prior to analysis. The EDX analyses were carried out with an FEI Nova NanoSEM 450 SEM equipped with an Oxford X-max80 EDX analyzer operating at an electron accelerating voltage of 10 kV.

2.2.3.3. Transmission Electron Microscopy

Micromorphology was studied by using transmission electron microscopy (TEM) and high resolution transmission electron microscopy (HR-TEM). TEM and HR-TEM studies were done with a JEOL 2010 UHR FasTEM operating at an accelerating voltage of 200 kV. The sample preparation was done by suspending the material in 2-propanol and then a drop of the suspension was placed onto a carbon-coated copper grid and allowed to dry.

2.2.3.4. Fourier Transformation infra Red (FT-IR) Spectroscopy

Fourier transformation infra red (FT-IR) spectra were obtained, using a Thermo-Scientific Nicolet FT-IR Model 8700 (in the range 4000−400 cm^{-1}) equipped with a DTGS detector. The dark brown manganese oxide powders

were ground with dry KBr at a ratio of 1:100 and then pressed into self supporting pellets at about 10 000 psi.

2.2.3.5. Thermo Gravimetric Analysis

Thermal stability studies of the materials were carried out by thermogravimetric analysis (TGA) using a Hi-Res TA instrument Model 2950. The temperature ramp for TGA was 20º/min in nitrogen atmosphere.

2.2.3.6. N_2 Sorption Studies

The nitrogen sorption experiments were carried out using a Quantachrome Autosorb iQ_2 surface area system. All samples were degassed at 150 °C for 12 h before the analysis. Determination of specific surface area was done using the Brunauer−Emmett−Teller (BET) method.

2.2.3.7. Raman Spectroscopy

Raman measurements were taken at room temperature on a Renishaw 2000 Ramascope attached to a charge-coupled device (CCD) camera, with an Ar^+ ion laser (514.4 nm) as the excitation source. Before each measurement was taken, the spectrometer was calibrated with a silicon wafer.

2.2.3.8. Inductively Coupled Plasma-Atomic Emission Spectroscopy

ICP-AES analyses were performed with a Thermo Jarrell Ash ICAP 61e Trace Analyzer. The standard solutions for ICP-AES were purchased from Alfa Aesar.

2.2.3.9. X-ray Photoelectron Spectroscopy

XPS analyses were carried out using a PHI model 590 spectrometer with multiprobes, using Al Kα radiation (λ=1486.6 eV) as the radiation source.

2.2.4. Catalytic Performance

Liquid phase benzyl alcohol oxidation was selected as a probe reaction which has been investigated by manganese oxide materials as catalysts. Benzyl alcohol (1 mmol) was dissolved in 15 mL of toluene in a 50 mL round bottomed flask charged with 50 mg of OMS-2 catalyst. The reaction mixture was stirred using a magnetic stir bar and refluxed in an oil bath for 2 h under air atmosphere (Scheme 2.1). Pristine K-OMS-2_{MWHY} and 0.50[Co]-K-OMS-2 prepared from the conventional hydrothermal method (0.50[Co]-K-OMS-2_{HY}) were also studied under the same conditions as control reactions.

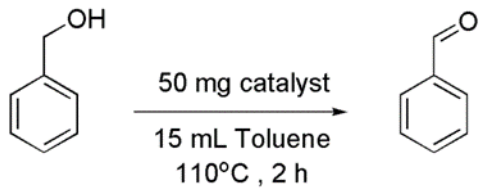

Scheme 2.1. Selective oxidation of benzyl alcohol to benzyl aldehyde.

2.2.5. Desulfurization Performance

The H_2S sorption experiments were carried out at 250ºC in a vertical fixed bed reactor made out of a quartz tube with an internal diameter of 2 mm. Prior to the desulfurization reactions, the sorbents were heated to 250ºC with a He flow of 10 standard cubic centimeters per minute (SCCM) and held for 1 h with a He flow of 36 SCCM. The outlet gas was analyzed with an analytical system comprised of a SRI 8610 GC equipped with a flame photometric detector (FPD) (Scheme 2.2). The separation was done using a GC-GasPro capillary column (30 m × 0.32 nm I.D.). The desulfurization reactions were carried out using a certified gas mixture (Scott Specialty Gases, 1 % H_2S in He). The sulfur sorption capacities were calculated according to Eq. 1.

$$\mathrm{SC}\left(\frac{\mathrm{g\ sulfur}}{100\ \mathrm{g\ sorbent}}\right) = \mathrm{WHSV} \times \left[\frac{\mathrm{M}}{\mathrm{V_{mol}}} \times \int_0^t (\mathrm{C_{in}} - \mathrm{C_{out}})\mathrm{d}t\right] \qquad (1)$$

Where *WHSV* is weight hourly space velocity in L h^{-1} g^{-1} (60 L h^{-1} g^{-1}), *M* is the atomic weight of sulfur (32 g mol^{-1}), V_{mol} is the molar volume in L mol^{-1} under standard conditions of 298 K and 1 atm (24.5 L mol^{-1}), C_{in} and C_{out} are the inlet and outlet concentrations (%), respectively, and *t* is the breakthrough time (BT) in hours. The BT is defined as the time when the outlet concentration reached 50 ppm.

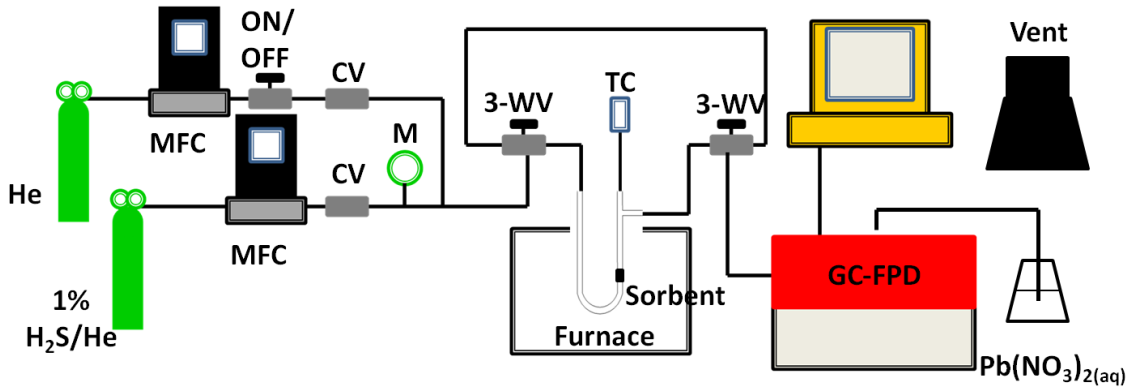

Scheme 2.2. Schematic representation of the experimental set-up. GC: Gas chromatograph, FPD: Flame photometric detector, MFC: Mass flow controller, TC: Thermocouple, 3WV: 3-Way valve, CV: Check valve, M: Manometer.

2.3. Results

2.3.1. Microwave assisted hydrothermal (MWHY) synthesis of K-OMS-2 and metal doped K-OMS-2 nanomaterials ([M]-K-OMS-2) and the effects of the reaction parameters on the lattice parameters

PXRD patterns obtained for the OMS-2 materials doped with different metal cations (Ag^{+}, Ce^{3+}, Co^{2+}, Cu^{2+}, Ni^{2+}, Sr^{2+}, V^{4+}, and Zn^{2+}) were used to identify the phase of the products, to determine the maximum amount of dopants which can be incorporated into OMS-2 materials without destroying the lattice structure, and to compare the relative peak intensities and the peak positions between different [M]-K-OMS-2 materials. As shown in Figure 2.2, the patterns agree with the natural tetragonal cryptomelane (space group *I4/m*) with chemical composition of KMn_8O_{16}. The diffraction patterns showed no additional peaks corresponding to segregated crystalline phases of the oxides of doped metals.

As observed in Figure 2.2, [Co]-K-OMS-2, [Cu]-K-OMS-2, and [Ni]-K-OMS-2 showed an increase in intensity of (110) peak (Figure 1b) and (220) peak, while the others did not show such effect. Furthermore, (110) and (220) peaks of both [Co]-K-OMS-2 and [Cu]-K-OMS-2 showed a shift towards lower 2θ values, while the rest of the peaks remained at the same position. All the other [M]-K-OMS-2 materials, except [Ce]-K-OMS-2, showed broad and less intense peaks as compared to pristine K-OMS-2.

Figure 2.3a shows the XRD patterns of pristine K-OMS-2 synthesized by a microwave assisted hydrothermal (K-OMS-2_{MWHY}) method, and 0.50[Co]-K-OMS-2 was synthesized by a reflux method (0.50[Co]-K-OMS-2_{REF}) (100ºC, 24 h, 1 bar), a microwave reflux method (0.50[Co]-K-OMS-$2_{MW\text{-}REF}$) (100ºC, 90 min, 1 bar), a conventional hydrothermal method (0.50[Co]-K-OMS-2_{HY}) (200ºC, 10 min, 22 bar), and a microwave assisted hydrothermal method (0.50[Co]-K-OMS-2_{MWHY}) (200ºC, 10 min, 22 bar). All the other XRD patterns except that for [Co]-K-OMS-2_{MWHY} showed peaks which could be indexed to a pure cryptomelane phase with no shifts in peak positions. Only the peaks indexed as (110) and (220) of [Co]-K-OMS-2_{MWHY} were shifted towards lower 2θ values with increased relative intensities.

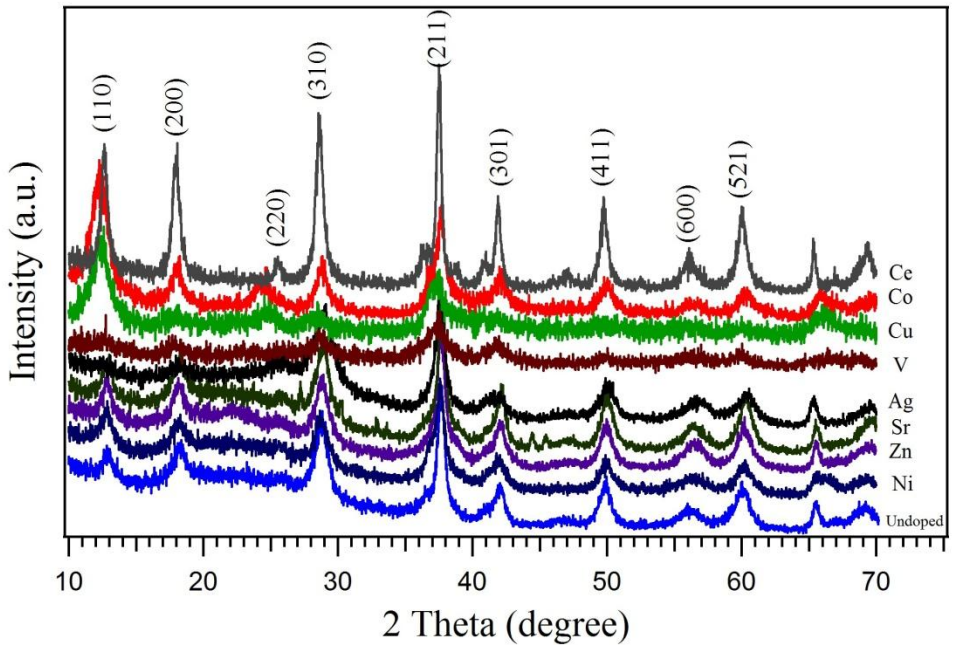

Figure 2.2. XRD patterns of different [M]-K-OMS-2 materials synthesized by MWHY method where M^{n+}/ Mn^{2+} initial molar is 0.50.

The effect of initial Co^{2+} to Mn^{2+} molar ratio on the [Co]-K-OMS-2_{MWHY} structure was studied, by using different initial $[Co^{2+}]/[Mn^{2+}]$ in the reaction mixture. Figure 2.4a shows the XRD patterns of [Co]-K-OMS-2_{MWHY} where $[Co^{2+}]/[Mn^{2+}]$ = *x* = 0.01, 0.03, 0.05, 0.07, 0.10, 0.50, 0.70, and 1.00 (*x* = Initial molar ratio between Co^{2+} and Mn^{2+}). As Figure 2.4a shows, with higher *x*, a gradual shift for (110) peak and (220) peak towards lower 2θ values was observed up to *x* = 0.70. The intensities of the afore-mentioned peaks were also progressively increased, while that of the other peaks decreased. Figure 2.4b shows that 0.01[Co]-K-OMS-2_{MWHY} consists of a $d_{(110)}$ of 6.80 Å, while the d spacing increases up to 7.43 Å upon the gradual increase of *x*.

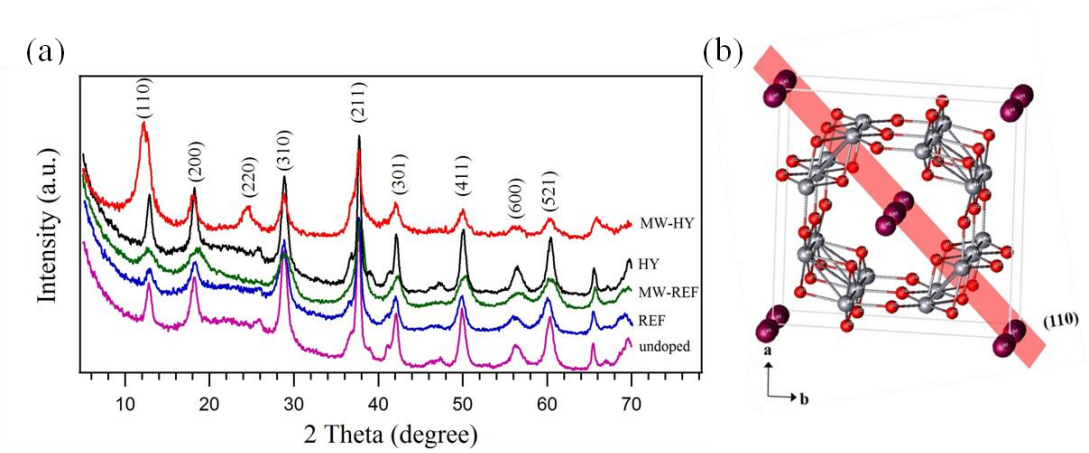

Figure 2.3. (a) XRD patterns of 0.50[Co]-K-OMS-2 materials synthesized by different methods (b) A perspective drawing of the solid state crystal structure of K-OMS-2, showing octahedrally coordinated porous framework and the imaginary (110) plane: red, O; grey, Mn; purple, K.

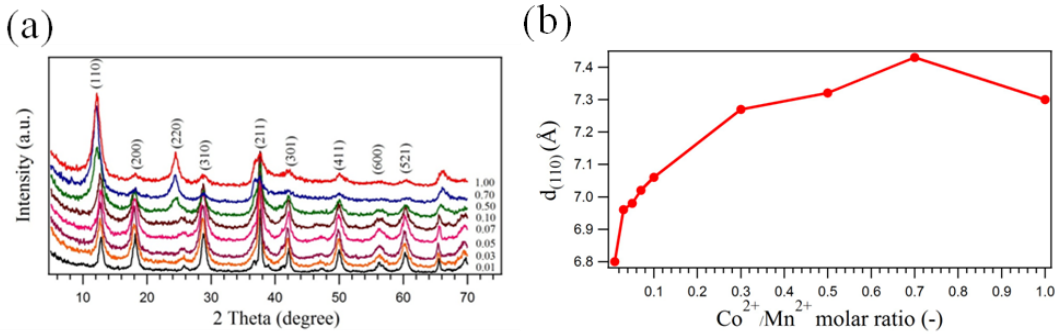

Figure 2.4. (a) XRD patterns of [Co]-K-OMS-2_{MWHY} at different initial Co^{2+}/Mn^{2+} initial molar ratios (b) Change in d-spacing with Co^{2+}/Mn^{2+} initial molar ratio.

2.3.2. Effect of cobalt doping on the shape evolution of [Co]-OMS-2_{MWHY} nanowires

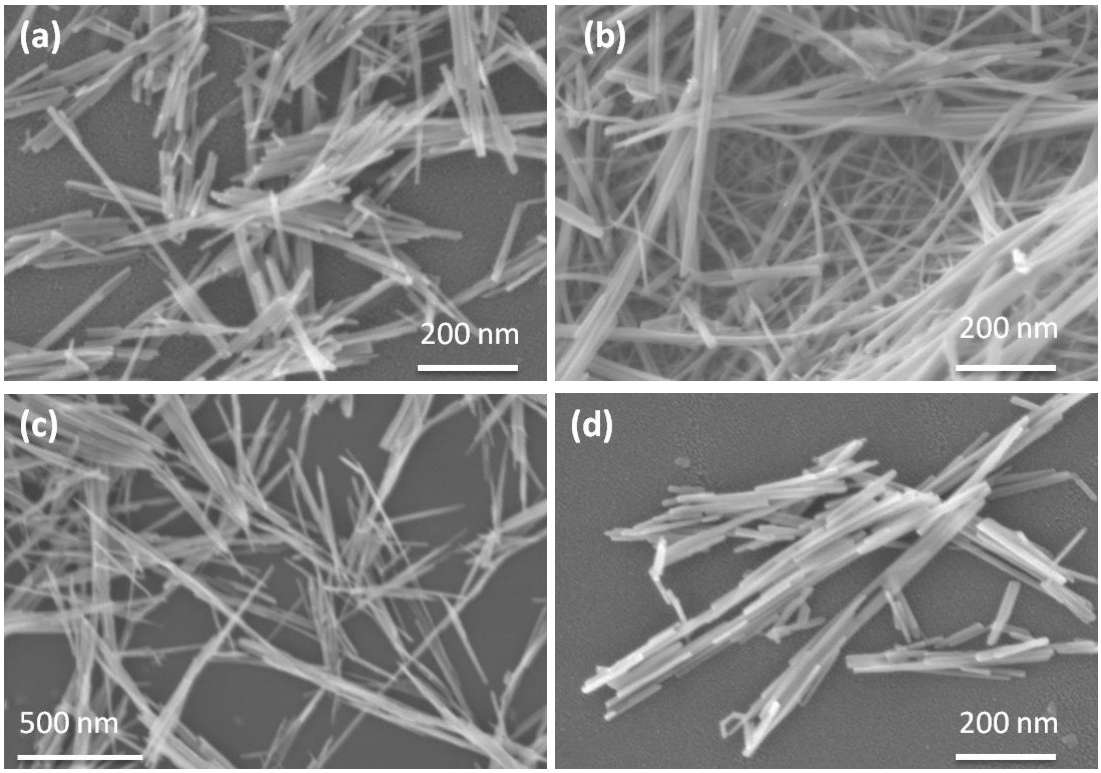

Figure 2.5. FE-SEM images of (a) K-OMS-2_{MWHY} (b) 0.50[Co]-K-OMS-2_{MWHY} (c) 0.50[Co]-K-OMS-2_{REF} and (d) 0.50[Co]-K-OMS-2_{HY}.

Figure 2.5 shows the typical morphologies of as-synthesized K-OMS-2_{MWHY} and [Co]-K-OMS-2 synthesized by different synthetic routes, obtained by FESEM. The pristine K-OMS-2_{MWHY} shows the typical fibrous morphology of K-OMS-2 synthesized by MWHY method at 200ºC in the previous studies (Figure 2.5a).[29] 0.50[Co]-K-OMS-2_{REF} (Figure 2.5c) consists of microwires (> 1 µm) with a narrow width. 0.50[Co]-K-OMS-2_{HY} (Figure 2.5d) consists of shorter fibers (~700 nm) compared to 0.50[Co]-K-OMS-2_{REF}. However, in both the cases fiber

length was higher than that of pristine K-OMS-2 (Figure 2.5a). In contrast to [Co]-K-OMS-2 obtained by the conventional methods, the materials obtained by a MWHY method consist of long microwires (Figure 2.5b). The diameters of the fibers/microwires range between 12 to 16 nm.

2.3.3. Effect of reaction parameters on the extent of cobalt doping

The cation compositions of undoped K-OMS-2_{MWHY} and [Co]-K-OMS-2 synthesized by different methods were determined by ICP-AES elemental analysis (Figure 2.6a). The potassium to manganese atomic ratio (K/Mn) in undoped K-OMS-2_{MWHY} was 0.122. The K/Mn atomic ratios in 0.50[Co]-K-OMS-2 were increased in the order of reflux method (0.115), conventional hydrothermal method (0.132), and microwave hydrothermal method (0.172). The same trend was observed in Co/Mn atomic ratio. In contrast to the reflux (Co/Mn = 0.053) and conventional hydrothermal (Co/Mn = 0.085) methods, MWHY method showed a very high cobalt content. (Co/Mn = 0.259).

EDX was used to analyze the atomic percentage of K, Co, and Mn in the bulk material with increasing initial Co^{2+} to Mn^{2+} molar ratio (Figure 2.6b). The potassium amount initially remained almost constant, but slightly increased with higher cobalt amounts. The cobalt amount was gradually increased from 2.6 to 26.0% while manganese amount was decreased from 84.3 to 58.9% with increasing *x* in the initial reaction mixture. The elemental maps shown in (Figure 2.7) suggest that there are no segregated cobalt oxide impurities, and both the Mn and Co species are well dispersed throughout the sample.

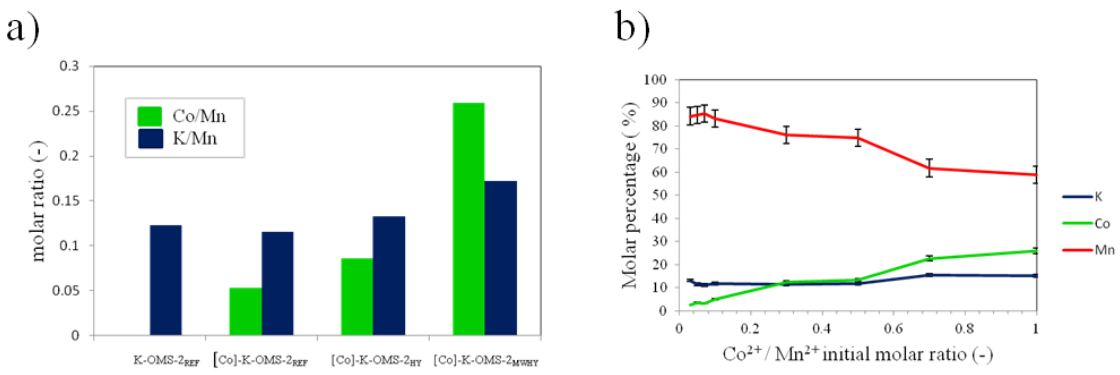

Figure 2.6. (a) Co/Mn and K/Mn molar ratios of K-OMS-2_{REF} and 0.50[Co]-K-OMS-2 synthesized with different synthesis methods, obtained by ICP-AES analysis (b) Change in composition of Mn, Co, and K with increasing cobalt amount obtained by EDX analysis.

2.3.4. Effect of cobalt doping on the microstructure

The microstructure of cobalt doped cryptomelane was confirmed by crystal structure studies carried out by TEM and HRTEM. As shown in Figures 2.8a, 2.8b and 2.8c, undoped K-OMS-2_{MWHY} method shows the typical fiber-like morphology of the OMS-2 materials. In contrast to its undoped counterpart, [Co]-K-OMS-2_{MWHY} showed long microwires with an average length of >1 µm. HRTEM images of undoped K-OMS-2_{MWHY} materials show periodic lattice fringes of 6.80 Å (Figure 2.9a) corresponding to the interplanar spacing of (110) planes ($d_{(110)}$). $d_{(110)}$ of 0.50[Co]-K-OMS-2_{MWHY} and 0.70[Co]-K-OMS-2_{MWHY} were 7.30 Å (Figure 2.9b) and 7.45 Å (Figure 2.9c), respectively. The $d_{(110)}$ values were comparable with the data obtained from XRD.

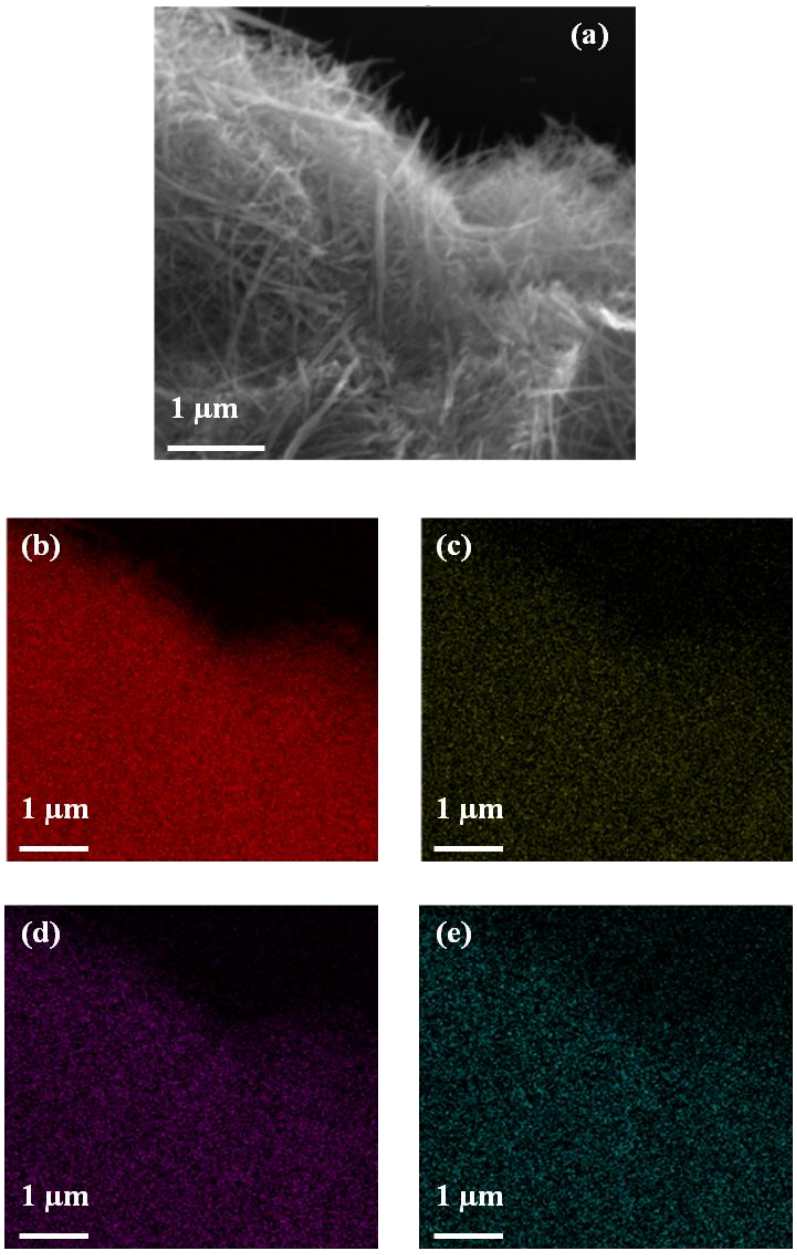

Figure 2.7. (a) FE-SEM image and EDX elemental maps of (b) oxygen (c) potassium (d) manganese and (e) cobalt in 0.50[Co]-K-OMS-2_{MWHY}.

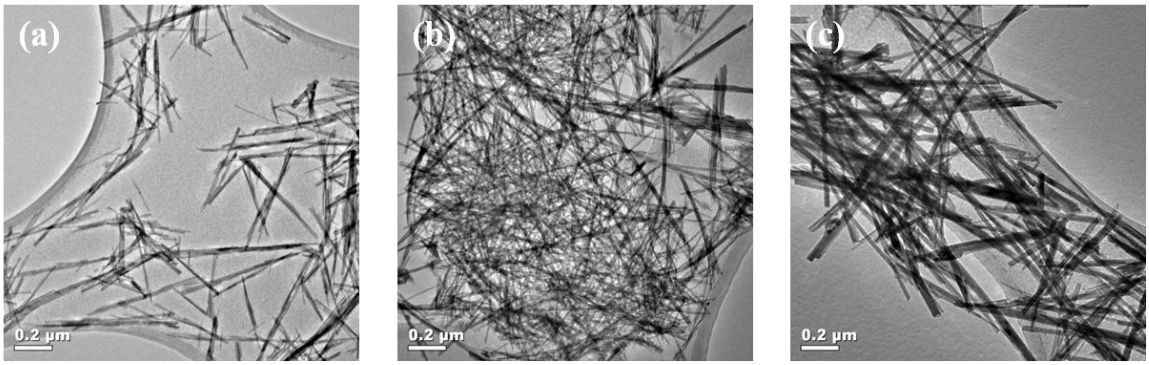

Figure 2.8. TEM images of (a) K-OMS-2_{MWHY} (b) 0.50[Co]-K-OMS-2_{MWHY} and (c) 0.70[Co]-K-OMS-2_{MWHY}.

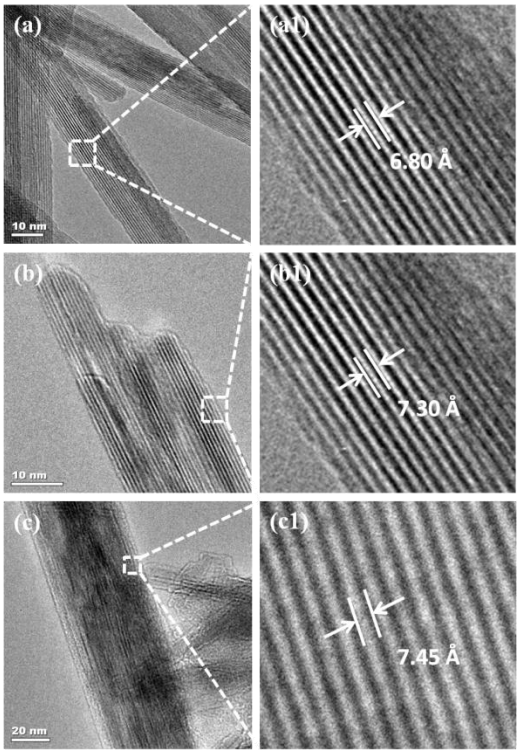

Figure 2.9. TEM and HRTEM images of (a) K-OMS-2_{MWHY} (b) 0.50[Co]-K-OMS-2_{MWHY} and (c) 0.70[Co]-K-OMS-2_{MWHY}.

2.3.5. Effect of cobalt doping on the surface properties, surface structure and composition

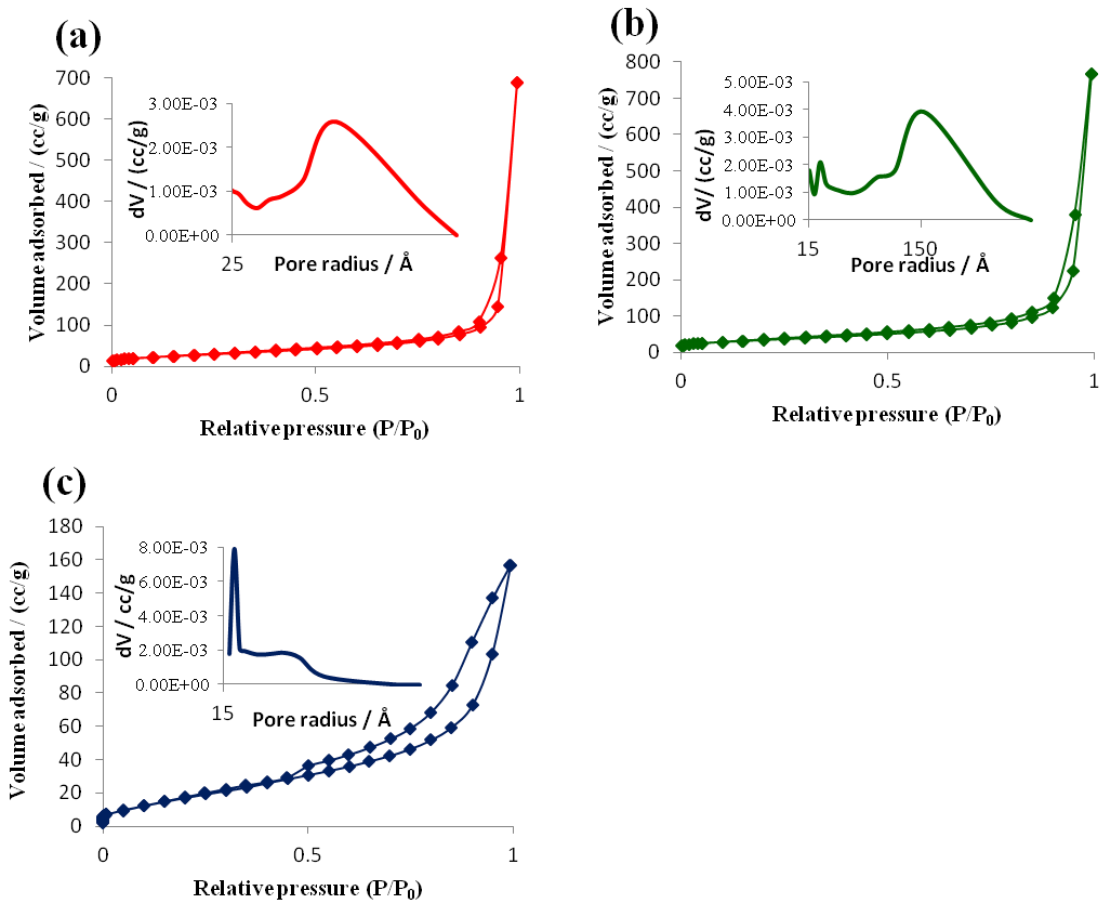

Figure 2.10. N_2 adsorption/ desorption isotherms and Barrett-Joyner-Halenda (BJH) desorption pore size distribution curves (inset) of (a) K-OMS-2_{MWHY} (b) 0.50 [Co]-K-OMS-2_{HY} and (c) 0.70 [Co]-K-OMS-2_{MWHY}.

As shown in Figure 2.10, the undoped K-OMS-2_{MWHY} and the [Co]-K-OMS-2_{MWHY} materials showed Type-IV N_2 adsorption/desorption isotherms (IUPAC classifications). These observations confirm that the as-synthesized materials are porous. The N_2 adsorption at low relative pressures suggest that monolayer

formation is the prevailing process, while at high partial pressures multi-layer formation takes place. The adsorption/desorption isotherms of the undoped K-OMS-2_{MWHY} and 0.50[Co]-K-OMS-2_{MWHY} were similar to those observed for K-OMS-2 materials prepared by other synthetic methods.[14,29] In contrast, the N_2 adsorption/desorption isotherm of 0.70[Co]-K-OMS-2_{MWHY} was quite different from those reported for regular K-OMS-2 materials. Compared to the reported hysteresis loops which occur at relative pressures (P/P_0) which are close to saturation, the observed hysteresis loop for 0.70[Co]-K-OMS-2_{MWHY} was fairly large and occurred at relatively low relative pressure values (0.45-0.80) which are far from saturation.[29] The BJH pore radii distribution curve for undoped K-OMS-2_{MWHY} was broad and centered at 15.6 nm which was consistent with the observed pore size distribution curves for similar materials.[29] In addition, 0.50[Co]-K-OMS-2_{MWHY} showed a narrow peak emerging at a lower pore radius, 1.9 nm. Interestingly, with increasing the cobalt amount, 0.70[Co]-K-OMS-2_{MWHY} showed only narrow peak centered at 1.9 nm.

The BET surface area of 0.50[Co]-K-OMS-2_{MWHY} was found to be higher than that for its undoped counterpart (124 over 101 m^2/g). On the other hand, 0.70[Co]-K-OMS-2_{MWHY} showed a lower surface area of 71 m^2/g. These results agree with the TEM data in terms of the particle size. When the material consists of significantly large particles, the surface area is decreased. In addition to the surface area, the pore volume of the as-synthesized materials follows the same trend. 0.50[Co]-K-OMS-2_{MWHY} shows a higher pore volume (1.18 cc/g) compared

to the undoped K-OMS-2_{MWHY} (1.06 cc/g), while 0.70[Co]-K-OMS-2_{MWHY} consists of the lowest (0.25 cc/g) (Table 2.1).

Table 2.1. BET surface area of as synthesized OMS-2 materials.

	SA (m^2/g)	Pore radii (Å)	Pore volume (cc/g)
(a) K-OMS-2_{MWHY}	101	156	1.06
(b) 0.50[Co]-K-OMS-2_{MWHY}	124	159	1.18
(c) 0.70[Co]-K-OMS-2_{MWHY}	71	19	0.25

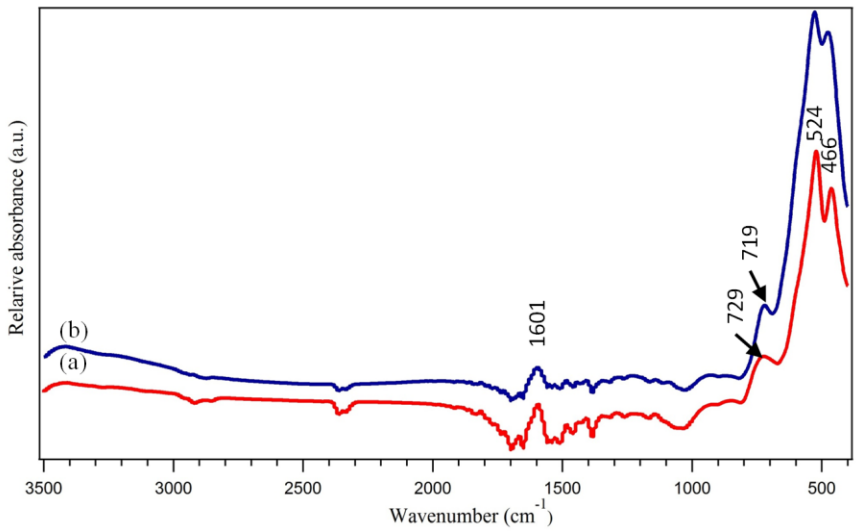

Figure 2.11. FTIR spectra of (a) K-OMS-2_{MWHY} (b) 0.50[Co]-K-OMS-2_{MWHY}.

The FTIR spectrum of the as-synthesized undoped K-OMS-2_{MWHY} (Figure 2.11) showed the features similar to those previously reported.[2,30,31] The broad band observed at about 3440 cm^{-1} and the band at 1634 cm^{-1} are identified as stretching and bending vibrations of adsorbed water molecules. Absorption bands were observed at around 729, 524, and 466 cm^{-1}. In 0.50[Co]-K-OMS-2_{MWHY}, the band at 729 cm^{-1} shifted towards lower wavelength (719 cm^{-1}) whereas the peak at 466 cm^{-1} decreased in intensity (Figure 2.12a).

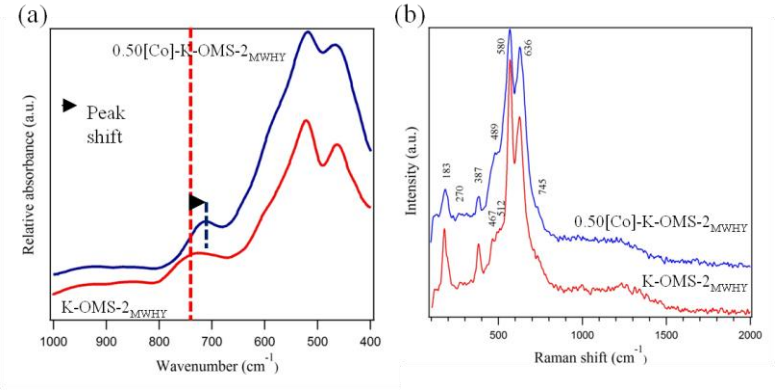

Figure 2.12. (a) FTIR spectra and (b) Raman spectra of K-OMS-2_{MWHY} and 0.50[Co]-K-OMS-2_{MWHY}.

Due to the sensitivity of FTIR towards short and long-range orders of materials, the observed FTIR spectra were analyzed for the probable segregated phases of cobalt oxide impurities in the as-synthesized [Co]-K-OMS-2 materials. However, no segregated cobalt oxide impurities were detected in the samples analyzed.

The Raman scattering spectrum (Figure 2.12b) of the pristine K-OMS-2_{MWHY} featured four main contributions at 183, 387, 580, and 636 cm^{-1} along with weak bands at 270, 467, 512, and 745 cm^{-1}. The 0.50[Co]-K-OMS-2_{MWHY} also

showed four main peaks along with three weak bands at the same peak positions, while the weak band at 467 cm^{-1} was absent. The four Raman peaks around 183, 387, 580, and 636 cm^{-1} were relatively broader and less intense for the doped K-OMS-2_{MWHY}. In addition, 0.50[Co]-K-OMS-2_{MWHY} showed a lower intensity ratio between the bands at 580 and 636 cm^{-1} (I_{580}/I_{636}) compared to that of undoped K-OMS-2_{MWHY}. The well-defined Raman spectra obtained are in good agreement with the reported structural studies and the XRD data.

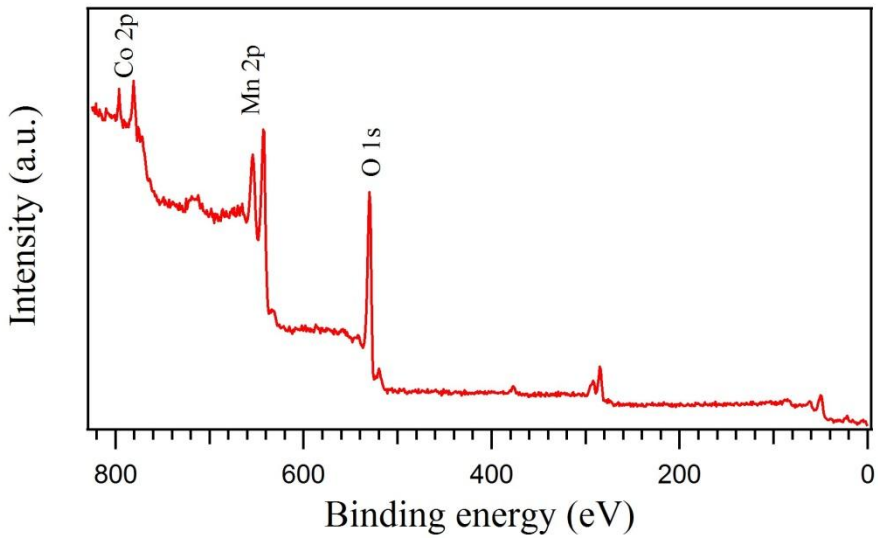

Figure 2.13. XPS spectrum of 0.50[Co]-K-OMS-2_{MWHY}.

XPS was used to analyze the binding energies of different elements present in pristine and cobalt doped K-OMS-2 materials. Figure 2.13 shows the full XPS spectra of undoped K-OMS-2_{MWHY} and 0.50[Co]-K-OMS-2_{MWHY}. In addition to the peaks that appear in undoped K-OMS-2_{MW-HY} material, two peaks were observed in 0.50[Co]-K-OMS-2_{MWHY}, which could be assigned to $2p_{3/2}$ and

$2p_{1/2}$ transitions of Co species. No other peaks were observed except for those assigned for C, Mn, O, and Co, suggesting the absence of impurity phases. The oxidation state of materials Co species in 0.50[Co]-K-OMS-2_{MWHY} was elucidated from the binding energy values corresponding to $2p_{3/2}$ and $2p_{1/2}$ transitions. Both peaks were deconvoluted into two peaks corresponding to two oxidation states of cobalt species according to their peak positions. The peaks at 779.6 and 795.5 eV correspond to the $2p_{3/2}$ and $2p_{1/2}$ transitions of Co^{3+}, while the peaks at 781.3 and 797.4 eV were assigned to $2p_{3/2}$ and $2p_{1/2}$ transitions of Co^{2+} respectively (Figure 2.14a). There was no peak observed at 778.1 eV, showing the absence of elemental Co metal and this observation suggests that all the cobalt is present as Co^{2+}/Co^{3+} species inside the OMS-2 structure.

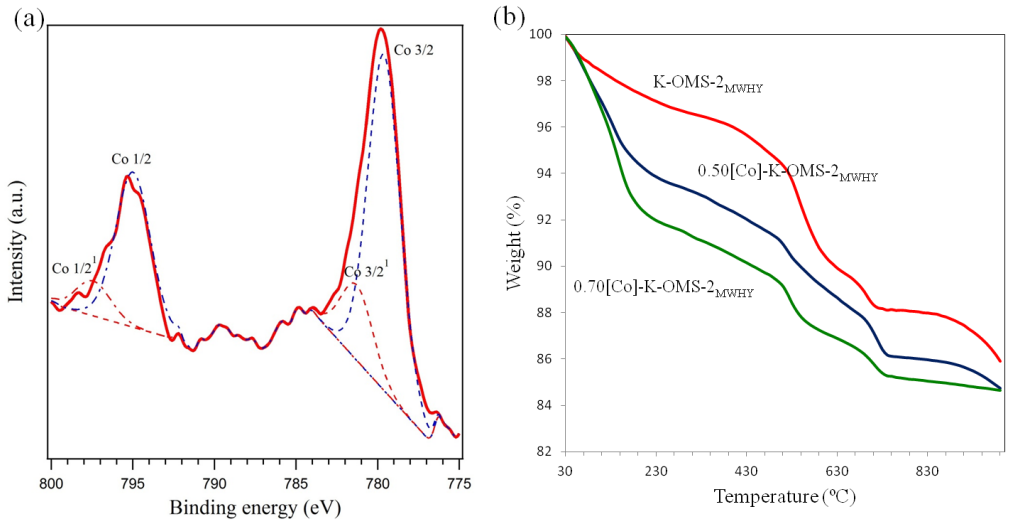

Figure 2.14. (a) XPS spectrum of Co 2p region of 0.50[Co]-K-OMS-2_{MWHY} (b) thermogravimetric analysis profiles of K-OMS-2_{MWHY}, 0.50[Co]-K-OMS-2_{MWHY} and 0.70[Co]-K-OMS-2_{MWHY}.

The O 1s core level spectrum (Figure 2.15) consists of a main peak at 528.8-528.9 eV which is corresponding to the binding energy (BE) of lattice oxygen. The undoped K-OMS-2_{MWHY} material showed two additional peaks appear at around 531.1 and 532.8 eV. The peak at 531.1 eV could be ascribed to the surface adsorbed O, OH- groups on the surface and O vacancies while the high BE peak at 532.8 eV is ascribed to adsorbed molecular H_2O. The O 1s spectrum of 0.50[Co]-K-OMS-2_{MWHY} also showed three distinct peaks, along with an additional peak at around 530.2 eV ascribed to the binding energy of oxygen belonging to the Co-O bond in the framework of K-OMS-2 material.

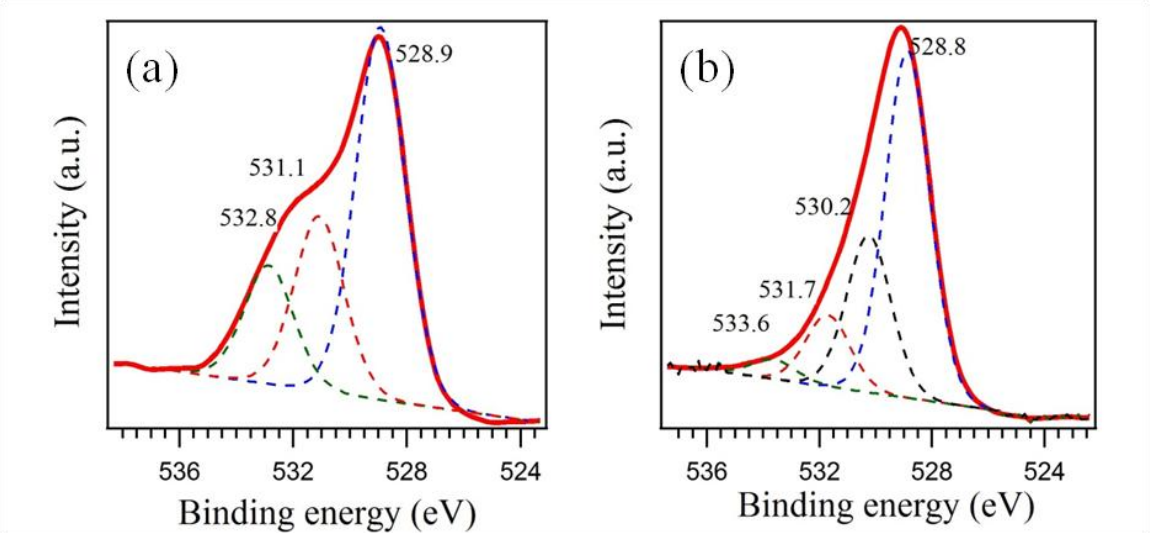

Figure 2.15. XPS spectra of O 1s region of (a) K-OMS-2_{MWHY} (b) 0.50[Co]-K-OMS-2_{MWHY}.

In the XPS analyses, slight peak shifts were observed in the binding energies corresponding to Mn $2p_{3/2}$ and Mn $2p_{1/2}$ transitions (Figure 2.16) for 0.50[Co]-K-OMS-2_{MWHY}. The observed BE values for both Mn $2p_{3/2}$ (642.4 eV) and Mn $2p_{1/2}$ (653.8 eV) of 0.50 [Co]-K-OMS-2_{MWHY} were higher than those of

undoped K-OMS-2_{MWHY} (641.7 and 653.1 eV, respectively). According to the literature, corresponding BE for Mn^{4+} is 642.4 eV which suggests that, the relative concentration of Mn^{4+} ions present on the surface of 0.50[Co]-K-OMS-2_{MWHY} was higher than that on the pristine material.

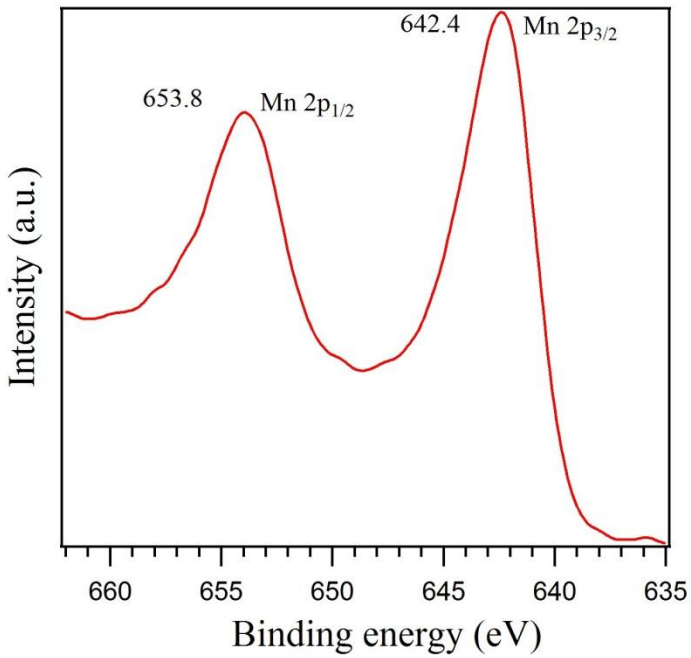

Figure 2.16. XPS spectrum of Mn 2p region of 0.50[Co]-K-OMS-2_{MWHY}.

2.3.6. Effect of cobalt doping on the Thermal stability

The TGA profiles, which were carried out under nitrogen atmosphere, of undoped K-OMS-2_{MWHY}, 0.50[Co]-K-OMS-2_{MWHY}, and 0.70[Co]-K-OMS-2_{MWHY} are shown in Figure 2.14b. The weight losses observed are in good agreement with the previous studies.[32,33] Four major losses were identified in both the undoped and doped materials. The thermal stability of the undoped material was found to be greater than that of the doped materials, and the thermal stability was decreased with increasing cobalt concentration. The first weight loss was

observed between room temperature and 150ºC and the cobalt content had a great impact on this particular weight loss. The second weight loss was observed in the region of 150-550ºC. The third weight loss occurred between 580-610ºC for the undoped material, while weight loss started at 550 and 540ºC for 0.50[Co]-K-OMS-2_{MWHY} and 0.70[Co]-K-OMS-2_{MWHY}, respectively. The fourth and final weight loss was observed between 710-740ºC.

2.3.7. Selective oxidation of benzyl alcohol to benzyl aldehyde

The catalytic performances of the synthesized materials were analyzed by their reactivity towards the selective oxidation of benzyl alcohol. The reactions were carried out in a conventional reflux system under atmospheric conditions using atmospheric air as the only oxidant. In a typical reaction, 50 mg of catalyst, 1 mmol of benzyl alcohol, and 15 mL of toluene were reacted in a 50 mL round bottomed flask (Scheme 2.1). An aliquot from the reaction mixture was withdrawn after 2 h, diluted with toluene and was analyzed using GC-MS. As the results shown in Table 2.2, benzyl aldehyde was observed as the only product, hence; selectivity of all the catalysts was 100%. The conversions obtained by the K-OMS-2_{REF}, and K-OMS-2_{MWHY} were 21 and 24% respectively. The 0.50[Co]-K-OMS-2_{HY} afforded 29% conversion. On the other hand, [Co]-K-OMS-2_{MWHY} materials gave very high conversions; 49% by 0.70[Co]-K-OMS-2_{MWHY}, and 55 % by 0.50[Co]-K-OMS-2_{MWHY}. The spent catalyst was recovered by centrifugation followed by drying at 200ºC for 12 h. The recovered catalyst was used in a successive reaction in order to test the catalytic stability and reusability. As Table

2.2 shows the recovered catalysts have no significant loss activity. Possible leaching of the catalyst was tested by removing the catalyst from the reaction mixture after 2 h and continuing for 24 more hours under the same reaction conditions. The absence of a change in conversion suggested that no homogeneous catalysis took place due to catalyst leaching.

Table 2.2. Selective oxidation of benzyl alcohol[a].

Catalyst	Conversion %[b]	Selectivity %[c]	TON[d]
0.50[Co]-K-OMS-2_{MWHY}	55	100	8.3
1st recovery[e]	38 (44[f])	100	7.6
0.70[Co]-K-OMS-2_{MWHY}	49	100	7.8
0.50[Co]-K-OMS-2_{HY}	29	100	4.6
K-OMS-2_{MWHY}	24	100	3.8
K-OMS-$2_{REF.}$	21	100	3.3

[a]Reaction conditions: 50.0 mg of catalyst, 1 mmol of benzyl alcohol, reaction time = 2 h, T = 110 ºC, and 15 mL of solvent. [b]Conversion (%): based on substrate = [1 – (concentration of substrate left after reaction) × (initial concentration of the substrate)$^{-1}$] × 100. [c]Selectivity: based on benzyl aldehyde. [d]TON: moles of substrate converted per mole of catalyst. [e]First recovery: mass of the catalyst recovered was 40 mg. [f]Calculated conversion for fresh catalyst.

2.3.8. Desulfurization performance for the removal of hydrogen sulfide

X-ray diffraction analyses performed on the samples after sulfidation at 250ºC are shown in Figure 2.17. Sulfidation of any K-OMS-2 material leads to a transformation of the tetragonal cryptomelane (space group *I4/m*) phase into a

mixture of cubic α-MnS and hexagonal γ-MnS phases. No other peaks from β-MnS were observed in the XRD pattern.

The EDX elemental maps (Figure 2.18) showed the sulfur distribution in the sulfided 0.50[Co]-K-OMS-2_{MWHY} material. The breakthrough curves are presented in Figure 2.19a. The undoped K-OMS-2_{MWHY}, 0.50[Co]-K-OMS-$2_{HY,}$ and 0.50[Co]-K-OMS-2_{MWHY} showed breakthrough (BT) times of 5.0, 5.1, and 12.8 h, respectively. Commercial MnO_2 did not show any significant activity towards H_2S sorption. The sulfur sorption capacity was calculated according to Eq. (1) and the values are compared in Figure 2.19b.

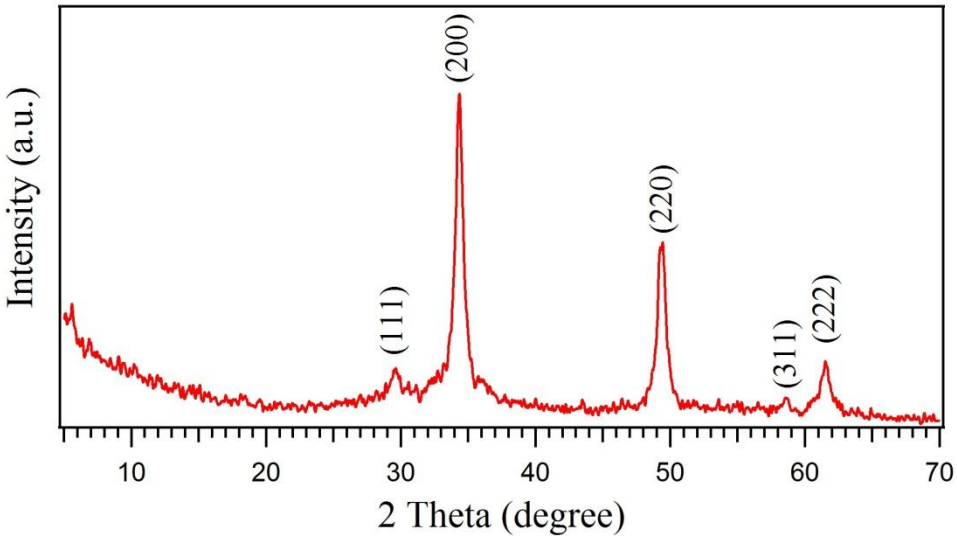

Figure 2.17. XRD pattern of 0.50[Co]-K-OMS-2_{MWHY} after sulfidation at 250ºC.

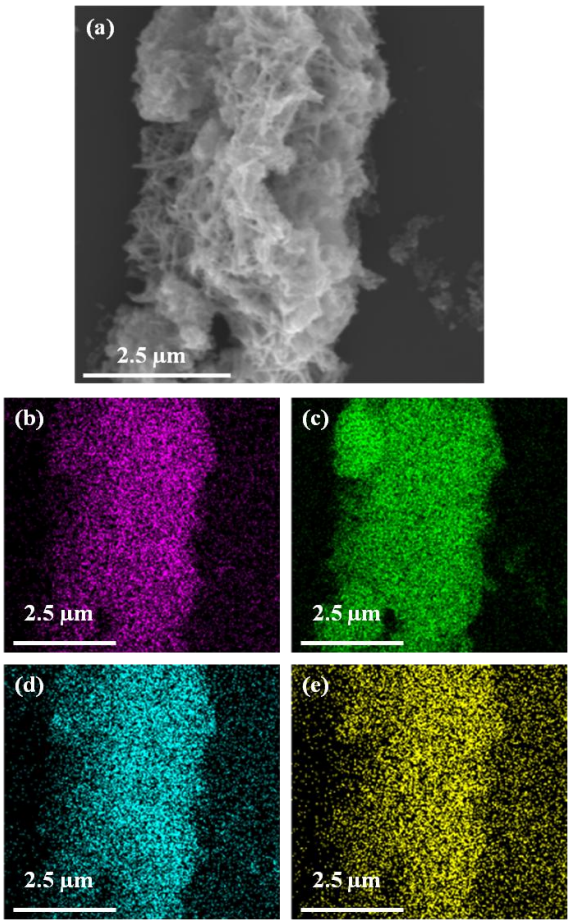

Figure 2.18. (a) FE-SEM image and EDX elemental maps of (b) oxygen (c) sulfur (d) manganese and (e) cobalt in 0.50[Co]-K-OMS-2_{MWHY} after sulfidation at 250ºC.

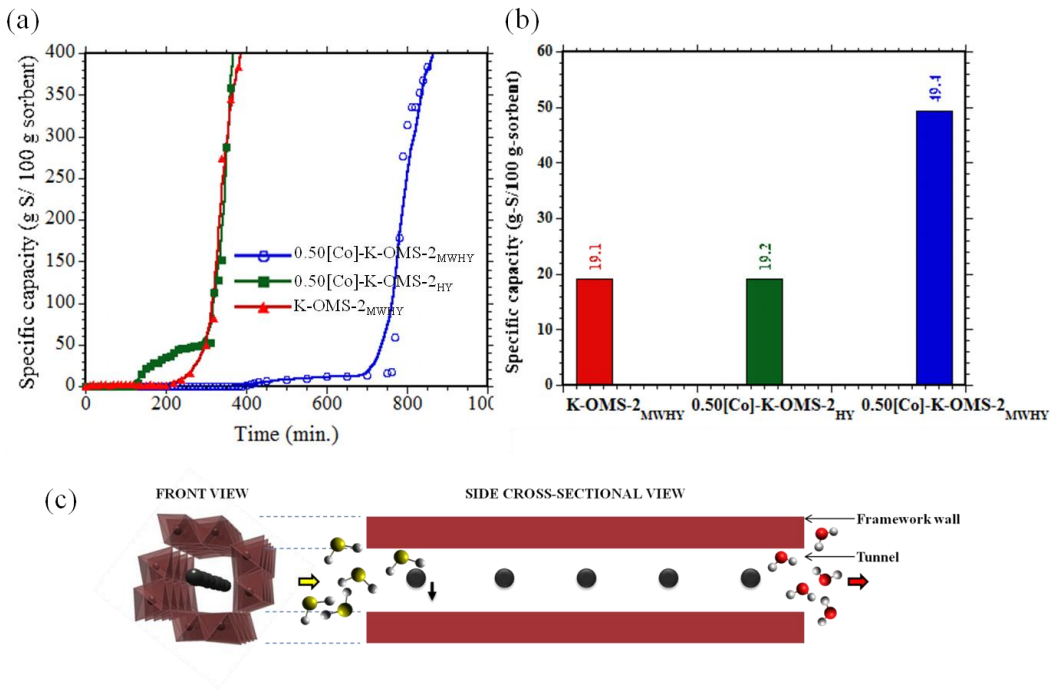

Figure 2.19. (a) Breakthrough curves (b) sulfur sorption capacities for K-OMS-2_{MWHY} , 0.50[Co]-K-OMS-2_{HY} and 0.50[Co]-K-OMS-2_{MWHY} and (c) possible $H_2S_{(g)}$ sorption mechanism by K-OMS-2: white, H; red, O; yellow, S; grey, K.

2.4. Discussion

In this work, K-OMS-2 and [M]-K-OMS-2 nanomaterials were prepared using a microwave assisted synthetic route in aqueous media under hydrothermal conditions. The precursors used for the synthesis of K-OMS-2_{MWHY} consist of $K_2S_2O_8$ as the oxidant which possesses a standard reduction potential of 2.01 V for the $S_2O_8^{2-}/SO_4^{2-}$ couple. Since the standard reduction potential of MnO_2/Mn^{2+} couple is 1.23 V, a redox potential of 0.78 V exists between the $S_2O_8^{2-}/SO_4^{2-}$ and MnO_2/Mn^{2+}, hence a spontaneous reaction takes place. On the other hand, in the presence of Co^{2+} where the standard reduction potential of Co^{3+}/Co^{2+} couple is 1.99 V, the oxidation of Co^{2+} to Co^{3+} is less favorable compared to the oxidation of Mn^{2+}.

During the initial phase of the reaction, a microwave induced nucleation takes place between the reactants which is achieved by a rapid temperature ramping or an instantaneous heating step. The temperature increases to 200ºC within 1 min and this rapid heating process gives rise to products with unique and novel chemical and physical characteristics. This rapid temperature ramp provides enough energy for cobalt ions to get inserted into the cryptomelane lattice structure. Hence, a higher amount of Co (51.8% doping) could be found in the structure compared to conventional reflux (10.6% doping) and hydrothermal (17.1% doping) methods (Figure 2.6a). Co species residing in framework sites, as shown in EDX elemental maps (Figure 2.7), are uniformly distributed throughout the final material with no segregated phases. The rapid heating

process is powered by a microwave power of 350-400 W. The quality of the final product depends on the careful control of temperature throughout the reaction. Therefore, the temperature inside the reaction vessel was maintained at 200ºC, forming a uniform thermal field during the growth phase.

During this stage the microwave power was maintained at a constant value around 50 W in order to eliminate uncontainable growth of the nanoparticles. The nanoparticle growth was governed by the Ostwald ripening mechanism under these conditions. The reaction was quenched rapidly after 10 min using a N_2 flow. The pressure inside the reaction vessel followed the same path as the temperature profile by reaching high pressures during the initiation step and by maintaining a constant value throughout the reaction process. Since ions in solution increase the absorption of microwave energy, the maximum pressure increased slightly (16 to 22 bar) with the increase of initial cobalt concentration.[27] Rapid super heating was not observed with water due to a relatively moderate dielectric loss tangent (tan δ) of 0.12.

In elucidating the final state of Co species, three possible mechanisms were identified. Co species could form oxides outside the K-OMS-2 nanoparticles and exist as a secondary phase. Since the characterization data, such as XRD, FESEM, TEM, FTIR spectroscopy, Raman spectroscopy, and TGA, for [Co]-K-OMS-2_{MWHY} strongly suggest that the product consists of a single phase, and the possibility of having a second phase of cobalt oxide could be ruled out. Two other possibilities could be taking place during the nucleation and growth processes where Co species is found inside the structure of K-OMS-2 materials. Cobalt ions

could substitute for K^+ in the VIII-fold tunnel sites maintaining the structural integrity which should result in a gradual loss in K^+ with increasing the Co amount. On the other hand, Co species can compete with Mn and obtain a VI-fold site in the framework of OMS-2 material. Considering the crystal radii (CR) of Co^{2+} (0.79 Å) and Co^{3+} (0.685 Å), which are significantly lower than that of K^+ (1.65 Å), it is difficult for Co species to occupy VIII-fold coordination sites. However, VI-fold coordination is possible according to Pauling's coordination principle.

Co CR are also very close to those of VI fold coordinated Mn^{3+} low spin (LS) (0.72 Å), VI fold coordinated Mn^{3+} high spin (HS) (0.785 Å), and VI fold coordinated Mn^{4+} (0.67 Å). Therefore, it is highly possible for Co to reside in the framework sites rather than in tunnel sites. Hence, Co is doped into the framework by substituting for Mn species. At the same time, ICP-AES and EDX data (Figures 2.6a and 2.6b, respectively) independently show that the amount of K in the structure does not decrease. Instead the K amount is increased while the amount of Mn is significantly decreased with higher Co amount.

This strongly suggests that Co resides at the framework sites which would potentially be occupied by Mn. The slight increase of K^+ with higher cobalt amount compensates the charge balance lost due to substitution of higher valent Mn^{3+} and Mn^{4+} by lower valent Co^{2+} and Co^{3+}. Since Co species reside in the framework sites, as suggested by EDX elemental maps, (Figure 2.7) they are uniformly distributed throughout the final material without being segregated. The compositions of the Co are significantly affected by the applied synthesis

method. When x = 0.50, a Co to Mn atomic ratio of 0.26 in the final material was observed with the MWHY method, while only 0.05 and 0.08 Co to Mn atomic ratios (by ICP-AES) were observed with conventional reflux and hydrothermal methods, respectively (Figure 2.6a).

The differences in the XRD patterns observed for $Co^{2+}(d^7)$, $Cu^{2+}(d^9)$, and $Ni^{2+}(d^8)$ doped materials from the other doped materials were associated with a lattice expansion of (110), and (220) planes and preferential growth along the [110] direction (Figure 2.2). However, the effects identified were more prominent with Co and Cu doped materials compared to that of Ni doped material. Further analyses of the electronic environments of these particular cations suggest that, these three dopant cations possess unequal electron occupancy of the d-orbitals that consist of the formal e_g set of the undistorted precursor. Although in the presence of an oxidant ($S_2O_8^{2-}$), according to Co 2p core level XPS spectra (Figure 2.14a), there is more than 25 % of initial Co^{2+} present in the final material with respect to the total Co^{2+} and Co^{3+} amount.

The characterization data collectively suggest that Co resides in the framework sites and both Pauling's rules and the literature suggest that Cu^{2+},and Ni^{2+} also reside in framework sites.[34] Hence, low spin Co^{2+} ($t_{2g}^6e_g^1$), Cu^{2+} ($t_{2g}^6e_g^3$), and low spin Ni^{2+} ($t_{2g}^6e_g^2$) cause tetragonal distortions of their respective MO_6 octahedra. This effect is induced by the *Jahn-Teller* effect, which in turn causes distortions in the lattice structure of metal doped K-OMS-2 nanomaterials. Although starting with the same Co^{2+} to Mn^{2+} molar ratio, the doping method

plays a significant role in determining the crystal structure of the final material (Figure 2.3a).

The MWHY and the conventional HY methods reached the same final temperature, pressure, and reaction time. However, the MWHY method possesses a very high T ramp (200ºC/min), hence the high pressure ramp (22 bar/min) compared to those of the conventional HY method (2.8 ºC/min and 0.3 bar/min respectively). The 0.50[Co]-K-OMS-2 material synthesized by reflux and microwave reflux methods were also analyzed as control experiments. Only [Co]-K-OMS-2_{MWHY} expressed a lattice expansion accompanied by a preferential growth along a particular direction (Figure 2.3a) suggesting that, not only high pressures and high temperatures, but also temperature ramps are responsible for such a pronounced effect. According to Figure 2.6a (ICP-AES data), the MWHY method showed the highest percentage of initial Co content in the final material. This could be due to the selective heating and rapid temperature ramp provided by the MWHY method as compared to conventional heating.

Both lattice expansion and preferential growth become more prominent with increasing Co concentration (Figure 2.4a) suggesting that, the afore-mentioned effects are determined by the amount of Co. The gradual expansion of the $d_{(110)}$ spacing (calculated using Debye-Scherrer equation) observed by XRD analysis (Figure 2.4b) further validates the assumption of framework doping. Conversely, if Co occupies the tunnel sites, such a gradual expansion of a particular plane may not be observed. The $d_{(110)}$ values observed with HRTEM are in accordance with those measured with XRD (Figure 2.9a, Figure 2.9b,

Figure 2.9c). The EDX data strongly suggests that it is Mn, but not K^+ in the tunnel sites, which gets substituted by Co since the Mn amount is greatly reduced while the Co amount is increased with increasing the initial Co^{2+} to Mn^{2+} molar ratio (Figure 2.6b).

Contrary to the fiber like morphology obtained for pristine K-OMS-2_{MWHY}, 0.50[Co]-K-OMS-2_{HY} and 0.50[Co]-K-OMS-2_{REF}, a homogenous microwire like morphology was observed with 0.50[Co]-K-OMS-2_{MWHY} (Figure 2.5). Huang et al. proposed a mechanism for the synthesis of K-OMS-2 with the microwave assisted hydrothermal method where manganese oxide octahedral unit (MnO_6) formation is followed by their aggregation forming flake like nanoparticles.[29] According to this model, at this stage, both the MnO_6 and CoO_6 octahedra are present in the reaction medium. During the course of the reaction these octahedral MnO_6 and CoO_6 units will aggregate and assemble into sheet like structures, which become slightly distorted due to the *Jahn-Teller* effect caused by Co. Due to the high pressure applied, the microwires start splitting apart (stress induced splitting) from the sheets (Figure 2.9b) while maintaining its longitudinal structural order. The lattice distortions originating due to Co make the splitting process easier with respect to the undoped K-OMS-$2_{MW\text{-}HY}$. Hence, in contrast to the nanofibers obtained by the other methods studied, Co-K-OMS-2 gives rise to longer microwire like morphologies.

The spectral features observed in the FTIR spectra can be ascribed to the Mn-O lattice vibrations of the MnO_6 octahedra and could be used to probe the effects caused by changes in the lattice structure. Since the local environment of

oxygen coordination is affected by the substitution of Mn which in turn affects the lattice vibrations, there are peak shifts and changes in intensities of their FTIR spectra.[16,35] Although α-MnO_2 type phases could be diagnosed by absorption at ~310 cm^{-1}, they are not observed in this study due to the limitation of the FTIR detection range. The observed FTIR spectrum for 0.50[Co]-K-OMS-2_{MWHY} shows a considerable peak shift of the band at 729 cm^{-1} (Figure 2.12a). Furthermore, a significant contribution from the tunnel cations in the FTIR spectrum should not be observed[36] hence the changes in the FTIR spectrum of [Co]-K-OMS-2_{MWHY} with respect to its undoped counterpart are entirely due to framework doping of cobalt.

Regular K-OMS-2 belongs to the space group I4/m and its factor group analysis leads to the following irreducible representations which could be attributed to the Mn-O lattice vibrations;

$$\Gamma_{Mn\text{-}O} = 6A_g + 6B_g + 3E_g + 2A_u + 3B_u + 5E_u \qquad (2)$$

where A_g, B_g, and E_g (doubly degenerated) modes are Raman active, the A_u, and E_u modes are IR active and the B_u mode is silent. In Raman spectra of both the as synthesized pristine K-OMS-2_{MWHY} and [Co]-K-OMS-2_{MWHY} materials, all the predicted Raman active modes were not expressed. The reason might be the low polarizabilities and low resolutions of some of the modes. The bands at 580 and 636 cm^{-1}, which arise due to symmetric Mn-O vibrations assigned to the A_g mode, are indicative of the well developed tetragonal structure of MnO_6 octahedral chains containing 2 × 2 tunnels. The band at 636 cm^{-1} is considered to be related to the Mn-O vibrations perpendicular to the direction of octahedral

double chains while the band at 580 cm^{-1} is considered to be responsible for the Mn-O vibrations along the direction of the octahedral chain. Hence, the relative intensities between these two bands indicate a change in structural parameters. In this study, a decrease of I_{580}/I_{636} is observed with cobalt doped material compared to undoped K-OMS-2, suggesting a deviation of the lattice structure with cobalt doping (Figure 2.12b). Furthermore, the band at 387 cm^{-1} is attributed to Mn-O bending vibrations while the band at 745 cm^{-1} is ascribed to antisymmetric stretching vibrations.

The TGA data show that the cobalt doped materials possess a lower stability compared to its undoped counterpart which is in good agreement with the work done by King'ondu et al. (Figure 2.14b).[14] The first weight loss (room temperature to 150ºC) occurs due to desorption of physisorbed water molecules and other gaseous molecules. Here, the doped materials show a greater weight loss compared to the undoped material and becomes more significant with increasing cobalt amount. This observation might be related to the tunnel size of the OMS material. The higher the cobalt amounts and larger the tunnel size are, the higher the amounts of physisorbed water and other gaseous species are. The K^+ amount slightly increases as the dopant concentration increases (see EDX data) and a small amount of Co^{2+}/Co^{3+} species might reside in the tunnel sites. These factors also increase the amount of physisorbed water due to electrostatic attraction. The second weight loss (150 -550 ºC) is due to the chemisorbed water and gaseous species such as oxygen. The third major weight loss (550 or 580-610ºC) occurs due to the evolution of lattice oxygen leading to a lattice

decomposition of the OMS structure forming Mn_2O_3. The reason for the lattice oxygen evolution from the doped materials at a lower temperature than the undoped material might be related with the lattice vacancies created by the substitution with lower valent cobalt ions and the lattice constraints caused by the slight difference in crystal radii. The fourth weight loss (710-740ºC) is due to the phase transformation from Mn_2O_3 phase to the Mn_3O_4 phase with the loss of framework oxygen. The TGA data suggests that with Co doping the M-O (where M = Co or Mn) bonds get weakened due to increased bond lengths. This results in more labile lattice oxygen and larger tunnel sizes with increasing the amount of Co.

The as-synthesized [Co]-K-OMS-2 materials showed excellent catalytic activity toward the selective oxidation of benzyl alcohol to benzyl aldehyde (Table 2.2). The undoped K-OMS-2_{REF} showed an activity which is in agreement with the previous data.[2] The catalytic activity of 0.50[Co]-K-OMS-2_{MWHY} (55% conversion) is more than twice the catalytic activity shown by the undoped K-OMS-2_{REF} (21% conversion) and K-OMS-2_{MWHY} (24% conversion). The higher activity of 0.50[Co]-K-OMS-2_{MWHY} as compared to 0.70[Co]-K-OMS-2_{MWHY} might be due to the higher surface area (Figure 2.10) of the former (124 vs.71 m^2/g). According to the Mars van Krevelen mechanism, where substrates get adsorbed, activated, and desorbed, the oxygen vacancies created by low valent metal substitution have a pronounced effect on the catalytic activity. In addition with increased tunnel sizes and change in growth direction, the diffusion barrier for substrates to reach active sites is overcome in this study.

At 250ºC 0.50[Co]-K-OMS-2_{MWHY} shows a significantly high sulfur adsorption capacity compared to the commercial manganese oxide, K-OMS-2_{MWHY} and 0.50[Co]-K-OMS-2_{HY}. The initial metal oxide was converted to sulfide and the EDX data show evenly distributed sulfur in the OMS-2 materials (Figure 2.18). Since, H_2S has to diffuse further into the material as the sulfidation progresses, this process is controlled by the nature of the surface and the diffusion barrier for sulfur to reach the active sites. During the adsorption and diffusion of hydrogen sulfide into the OMS-2 tunnel, potassium ions residing in the tunnel sites restrict their further movement. Hence, for an efficient sulfidation mechanism to take place either potassium ions have to move slightly off the centerline or the tunnel has to be increased (Figure 2.19c). Figure 2.20 shows the EDX spectra of the sulfided material, in which the Co to Mn atomic ratio is not affected but the S content is significantly high (Table 2.3). In this study, cobalt doped K-OMS-2 provides microwires with a larger tunnel size where H_2S molecules (kinetic diameter = 3.6 Å) can diffuse easily since the displacement of potassium ions is minimized. The basic desulfurization reaction for metal oxides is identified as follows;

$$MO_{x(s)} + xH_2S_{(g)} \longrightarrow MS_{x(s)} + xH_2O_{(g)} \qquad (3)$$

where $MO_{x(s)}$ and $MS_{x(s)}$ are initial metal oxide sorbent and final sulfide material respectively. Therefore $H_2O_{(g)}$ is produced and leaves the K-OMS-2 tunnel as the sulfidation proceeds (Figure 2.19c). Metal substitution creates oxygen vacancies (see TGA data) which enhance the number of adsorption sites. Also, the lattice

constraints of the doped materials make the process of oxygen substitution by sulfur, more feasible.

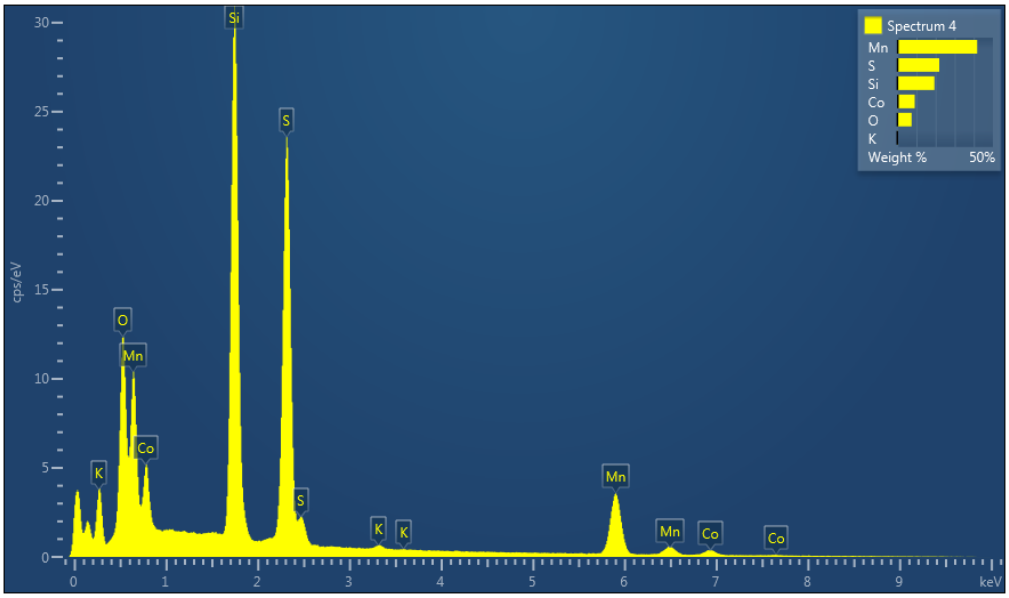

Figure 2.20. EDX spectrum of 0.50 [Co]-K-OMS-2_{MWHY} after sulfidation.

Table 2.3. Average weight and atomic percentages of elements in 0.50[Co]-K-OMS-2_{MWHY} after sulfidation.

Element	Weight %	Atomic %
O	8.98	22.0
S	27.36	33.4
Mn	49.65	35.4
Co	13.39	9.0

2.5. Conclusion

A fast, facile, and simple route for the synthesis of metal doped K-OMS-2 has been proposed and its lattice parameters, morphology, and growth direction have been carefully tailored by altering the dopant amount using microwave irradiation under hydrothermal conditions. Cobalt doped K-OMS-2 micro wires with $d_{(110)}$ ranging from 6.80 to 7.43 Å were synthesized for the first time using the MWHY method. The lattice spacing could be easily tuned by altering the Co amount. The dopant effect on the catalytic activity was studied based on benzyl alcohol oxidation to benzyl aldehyde where high catalytic performances were observed with a conversion of 55% and selectivity of 100%. By tuning the tunnel size, the as-synthesized materials were successfully evaluated as sorbents for removal of H_2S. The [Co]-K-OMS-2_{MWHY} material showed superior sulfur adsorption capacities (49.4 g sulfur/100 g sorbent) at temperatures as low as 250ºC where high conversions of oxide to sulfide were observed.

References

(1) Brock, S. L.; Duan, N.; Tian, Z. R.; Giraldo, O.; Zhou, H.; Suib, S. L. A review of porous manganese oxide materials. *Chem. Mater.* **1998**, *10*, 2619–2628.

(2) Dharmarathna, S.; King'ondu, C. K.; Pedrick, W.; Pahalagedara, L.; Suib, S. L. Direct sonochemical synthesis of manganese octahedral molecular sieve (OMS-2) nanomaterials using cosolvent systems, their characterization, and catalytic applications. *Chem. Mater.* **2012***, 24,* 705–712.

(3) Suib, S. L. Porous manganese oxide octahedral molecular sieves and octahedral layered materials. *Acc. Chem. Res.* **2008**, *41*, 479–487.

(4) Espinal, A. E.; Zhang, L.; Chen, C-H.; Morey, A.; Nie, Y.; Espinal, L.; Wells, B. O.; Joesten, R.; Aindow, M.; Suib, S. L. Nanostructured arrays of semiconducting octahedral molecular sieves by pulsed-laser deposition. *Nat. Mater.* **2010**, *9*, 54 - 59.

(5) Ding, Y-S.; Shen, X-F.; Sithambaram, S.; Gomez, S.; Kumar, R.; Crisostomo, V. M. B.; Suib, S. L.; Aindow, M. Synthesis and catalytic activity of cryptomelane-type manganese dioxide nanomaterials produced by a novel solvent-free method. *Chem. Mater.* **2005**, *17*, 5382–5389.

(6) Delimaris, D.; Ioannides, T. VOC oxidation over MnO_x–CeO_2 catalysts prepared by a combustion method. *Appl. Catal. B: Env.* **2008***, 84*, 303-312.

(7) Ghodbane, O.; Ataherian, F.; Wu, N.; Favier, F. In situ crystallographic investigations of charge storage mechanisms in MnO2-based electrochemical capacitors. *J. Power Sources* **2012***, 206*, 454-462.

(8) Gulbinska, M. K.; Suib, S. L. Vanadium-substituted porous manganese oxides with Li-ion intercalation properties. *J. Power Sources* **2011***, 196*, 2149-2154.

(9) Kumar, R.; Sithambaram, S.; Suib, S. L. Cyclohexane oxidation catalyzed by manganese oxide octahedral molecular sieves—Effect of acidity of the catalyst. *J. Catal.* **2009***, 262*, 304-313.

(10) Ramstad, A. L.; Mikkelsen, Ø. Structural characterisation of copper-containing manganese oxide octahedral molecular sieve (Cu-OMS-2) materials by X-ray absorption spectroscopy and cyclic voltammetry. *J. Mol. Struct.* **2004***, 697*, 109-117.

(11) X Makwana, V. D.; Son, Y.; Howell, A. R.; Suib, S. L. The role of lattice oxygen in selective benzyl alcohol oxidation using OMS-2 catalyst: A kinetic and isotope-labeling study. *J. Catal.* **2002***, 210*, 46-52.

(12) Takeuchi, K. J.; Yau, S. Z.; Menard, M. C.; Marschilok, A . C.; Takeuchi, E. S. Takeuchi, E. S. Synthetic control of composition and crystallite size of silver hollandite, $Ag_xMn_8O_{16}$: Impact on electrochemistry. *ACS Appl. Mater. Interfaces* **2012**, *4*, 5547–5554.

(13) Chen, X.; Shen, Y-F.; Suib, S. L.; O'Young, C. L. Characterization of manganese oxide octahedral molecular sieve (M−OMS-2) materials with different metal cation dopants. *Chem. Mater.* **2002**, *14*, 940–948.

(14) King'ondu, C. K.; Opembe, N.; Chen, C.; Ngala, K.; Huang, H.; Iyer, A.; Garcés, H. F.; Suib, S. L. Manganese oxide octahedral molecular sieves (OMS-2) multiple framework substitutions: A new route to oms-2 particle size and morphology control. *Adv. Funct. Mater.* **2011***, 21*, 312-323.

(15) Ming Sun, M.; Fei Ye, F.; Bang Lan, B.; Lin Yu, L.; ,Xiaoling Cheng, X.; Shengnan Liu, S.; Xiaoqing Zhang, X. One step hydrothermal synthesis of sn-doped OMS-2 and their electrochemical performance. *Int. J. Electrochem. Sci.* **2012**, *7*, 9278-9289.

(16) Cai, J. ;Liu, J.; Willis, W. S.; Suib, S. L. Framework doping of iron in tunnel structure cryptomelane. *Chem. mater.*, **2001**, *13*, 2413-2422.

(17) Liu, Z.; Xing, Y.; Chen, C-H.; Zhao, L.; Suib, S. L. Framework doping of indium in manganese oxide materials: synthesis, characterization, and electrocatalytic reduction of oxygen. *Chem. Mater.* **2008**, *20*, 2069–2071.

(18) Calvert, C.; Joesten, R.; Ngala, K.; Villegas, J.; Morey, A.; Shen, X.; Suib, S. L. Synthesis, characterization, and rietveld refinement of tungsten-framework-doped porous manganese oxide (K-OMS-2) material. *Chem. Mater.* **2008**, *20*, 6382–6388.

(19) Polverejan, M.; Villegas, J. C.; Suib, S. L. Higher valency ion substitution into the manganese oxide framework. *J. Am. Chem. Soc.* **2004**, *12*, 7774-7775.

(20) Sriskandakumar, T.; Opembe, N.; Chen, C-H.; Morey, A.; King'ondu, C.; Suib, S. L. Green Decomposition of Organic Dyes Using Octahedral Molecular Sieve Manganese Oxide Catalysts. *J. Phys. Chem. A* **2009**, *113*, 1523–1530.

(21) Bilecka, I.; Djerdj, I.; Niederberger, M. One-minute synthesis of crystalline binary and ternary metal oxide nanoparticles. *Chem. Commun.* **2008**, *7*, 886-888.

(22) Mohajerani, M. S.; Mazloumi, M.; Lak, A.; Kajbafvala, A.; Zanganeh, S.; Sadrnezhaad, S. K. Self-assembled zinc oxide nanostructures via a rapid microwave-assisted route. *J. Cryst. Growth* **2008***, 310*, 3621-3625.

(23) Lak, A.; Mazloumi, M.; Mohajerani, M. S.; Zanganeh, S.; Shayegh, M. R.; Kajbafvala, A.; Arami, H.; Sadrnezhaad, S. K. Rapid Formation of Mono-Dispersed Hydroxyapatite Nanorods with Narrow-Size Distribution via Microwave Irradiation. *J. Am. Ceram. Soc.* **2008***, 91*, 3580-3584.

(24) Tsuji, M.; Hashimoto, M.; Nishizawa, Y.; Kubokawa, M.; Tsuji, T. Microwave-assisted synthesis of metallic nanostructures in solution. *Chem. Euro. J.* **2005***, 11*, 440-452.

(25) Dias, A.; Matinaga, F.M.; Moreira, R. L. Vibrational spectroscopy and electron−phonon interactions in microwave-hydrothermal synthesized $Ba(Mn_{1/3}Nb_{2/3})O_3$ complex perovskites. *J. Phys. Chem. B* **2009***, 113,* 9749-9755.

(26) Liu, F.; Chang, Y.; Ko, F.; Chu, T. Microwave rapid heating for the synthesis of gold nanorods. *Mater. Lett.* **2004***, 58*, 373-377.

(27) Gedye, R. N.; Smith, F. E.; Westaway, K. C. The rapid synthesis of organic compounds in microwave ovens. *Can. J. Chem.* **1988**, 66, 17-26.

(28) Cheng, H.; Cheng, J.; Zhang, Y.; Wang, Q. Large-scale fabrication of ZnO micro-and nano-structures by microwave thermal evaporation deposition. *J. Cryst. Growth* **2007***, 299*, 34-40.

(29) Huang, H.; Sithambaram, S.; Chen, C-H.; Kithongo, C. K.; Xu, L.; Iyer, A.; Garces, H. F.; Suib, S. L. Microwave-assisted hydrothermal synthesis of cryptomelane-type octahedral molecular sieves (OMS-2) and their catalytic studies. *Chem. Mater.* **2010**, *22*, 3664–3669.

(30) Dharmarathna, S.; King'ondu, C. K.; Pedrick, W.; Pahalagedara, L.; Suib, S. L. Direct sonochemical synthesis of manganese octahedral molecular sieve (OMS-2) nanomaterials using cosolvent systems, their characterization, and catalytic applications. *Chem. Mater.* **2012**, *24*, 705–712.

(31) Opembe, N. N.; King'ondu, C. K.; Espinal, A. E.; Chen, C-H.; Nyutu, E. K.; Crisostomo, V. M.; Suib, S. L. Microwave-assisted synthesis of manganese oxide octahedral molecular sieve (OMS-2) nanomaterials under continuous flow conditions. *J. Phys. Chem. C* **2010***, 114,* 14417–14426.

(32) O Malinger, K. A.; Ding, Y.; Sithambaram, S.; Espinal, L.; Gomez, S.; Suib, S. L. Microwave frequency effects on synthesis of cryptomelane-type manganese oxide and catalytic activity of cryptomelane precursor. *J. Catal.* **2006***, 239*, 290-298.

(33) Li, J.; Wang, R.; Hao, J. Role of lattice oxygen and lewis acid on ethanol oxidation over OMS-2 Catalyst. *J. Phys. Chem. C* **2010**, *114,* 10544-10550.

(34) Hu, B.; Chen, C-H.; Frueh, S. J.; Jin, L.; Joesten, R.; Suib, S. L. Removal of aqueous phenol by adsorption and oxidation with doped hydrophobic cryptomelane-type manganese oxide (K−OMS-2) nanofibers. *J. Phys. Chem. C* **2010***, 114,* 9835–9844.

(35) Nyutu, E. K.; Chen, C-H.; Sithambaram, S.; Crisostomo, V. M. B.; Suib, S. L. Systematic control of particle size in rapid open-vessel microwave synthesis of K-OMS-2 nanofibers. *J. Phys. Chem. C* **2008***, 112,* 6786–6793.

(36) Gao, T.; Glerup, M.; Krumeich, H.; Nesper, R.; Fjellvåg, H.; Norby, P. microstructures and spectroscopic properties of cryptomelane-type manganese dioxide nanofibers. *J. Phys. Chem. C* **2008**, *112,* 13134–13140.

CHAPTER III. STRUCTURE AND OXIDATION ACTIVITY CORRELATIONS FOR CARBON BLACKS AND DIESEL SOOT

3.1. Introduction

Atmospheric aerosol particles are considered as air pollutants [1,2] due to their impact on the environment, climate, and public health, including in vitro mammalian cell chromosomal and DNA damage activities.[3] Among these pollutants, Diesel Particulate Matter (DPM) or soot – primarily composed of carbon – has significant adverse impact on global warming and health issues.[1,4] DPM is typically trapped using Diesel Particulate Filters (DPFs), which are periodically regenerated to oxidize the accumulated soot particulates.[1] Due to the highly complex nature,[5,6] ambiguity, and unpredictability of the multi-component soot structure, as well as varying diesel engine operating conditions, optimized DPF operation and regeneration is a challenging task.[7] Since the DPF regeneration behavior is highly dependent on the oxidation reactivity of soot, several studies have been conducted to explore the effect of structure on the soot oxidation activity.[1,8,9]

In the previous studies, structure and activity of diesel soot and other carbonaceous materials have been investigated using various characterization techniques. Su and colleagues used High Resolution Transmission Electron Microscopy (HRTEM) and Thermo Gravimetric Analysis (TGA) to study the relation between microstructure and oxidation behavior of soot from exhausts of different heavy duty diesel engines and discovered the microstructure-controlled

oxidation behavior of diesel soot.[10] Boehman *et al*. also used Transmission Electron Microscopy (TEM) and HRTEM along with TGA and Differential Scanning Calorimetry (DSC) to study the relationship between soot nanostructure and oxidation reactivity, and thereby the DPF regeneration behavior.[11] In addition to the TEM/HRTEM and TGA studies, Muller *et al*. used Diffuse Reflectance Infra-red Fourier Transform Spectroscopy (DRIFTS) to correlate the reactivity with oxygen containing functional groups and nanostructure of spark discharge soot, soot from a heavy duty diesel engine, soot from a diesel engine in black smoking, and furnace carbon black.[12] They concluded that the amount of defects and types of functional groups are important in determining the reactivity. Muller and colleagues also studied the relation between the oxidative behavior and the microstructure of black smoke soot using a diesel engine soot sample (P1 soot) and a commercial carbon black sample (Lamp black), and discovered that P1 soot is more aromatic and contains higher surface functionality with lower oxidation temperatures than lamp black.[9] Song *et al*. used various characterization techniques, such as TEM/HRTEM, X-Ray Diffraction (XRD), Electron Energy Loss Spectroscopy (EELS), Fourier Transform Infrared (FT-IR) spectroscopy, Raman spectroscopy, and TGA, and determined correlations between some structural properties, such as degree of organization and number of stacking, and the oxidation rate constants. They also studied the oxidation mechanism of one of the soot samples describing the importance of presence of surface oxygen groups in addition to the initial structure and pore size distribution.[8] Both Knauer *et al*. and Schmid *et al*. studied

the soot structure and reactivity correlations mainly with Raman spectroscopic studies and temperature programmed oxidation studies using various soot samples from different engine conditions as well as commercial carbon black samples.[4,13] These two groups respectively discussed how the dispersive character of Raman “D mode” can be used in structural analysis of carbonaceous material, and how the multi wavelength Raman microscopy (MWRM) can be applied in the prediction of diesel soot oxidation behavior. Lapuerta *et al*. studied the effect of the different engine conditions on soot structural characteristics, such as primary particle size, Raman band area ratios (A_{D1}/A_G, A_{D3}/A_G) and intensity ratios (I_{D1}/I_G, I_{D3}/I_G), crystallite stacking height (Lc), and crystallite length (La), using a biodiesel soot and a diesel soot with three different loading modes. Their studies revealed that biodiesel soot is higher in oxidation activity than diesel soot, and suggested the internal graphitic structure of biodiesel soot alone does not describe its oxidation behavior, but other analyses are needed for a satisfactory explanation .[14]

The aforementioned literature studies have focused on limited structural characterization of diesel soot formed under various diesel engine operating conditions,[4,8,14,15] as well as of commercially available carbon black materials.[9,10,13] However, a fundamental understanding about the direct correlations between the important structural parameters and the reactivity under oxidative environments using a large number of samples and multiple characterization methods is lacking. To address this gap, we focus on structural characterization of two different diesel engine soot samples and ten commercial

carbon black samples using six techniques, viz., Scanning Electron Microscopy (SEM), TEM/HRTEM, nitrogen sorption, Raman spectroscopy, XRD, and TGA.

Use of microscopic studies such as Field Emission Scanning Electron Microscopy (FE-SEM) and TEM is quite common in studies on soot and other carbonaceous materials. These techniques have been used to study the aggregation patterns and the morphology of primary particles, to calculate the average primary particle size, to analyze the microstructure of primary particles, etc.[4,6,16,17] Nitrogen sorption methods, such as total surface area, pore structure,[18] and pore size distribution,[19] morphological changes upon chemical modification,[20] and defects on carbon surfaces,[21] have been widely used in structure related studies of diesel soot and commercial carbon blacks. Raman spectroscopy is a promising and sensitive technique for the analysis of crystalline long range order (e.g., graphitic materials),[22] as well as molecular structures with a short range order (e.g., amorphous carbon or disturbed graphitic lattices).[23] In the previous studies on soot using Raman spectroscopy, the structure has been described considering either the relative D band (stands for “defect”) and G band (stands for “graphitic”) intensities or the relative D band and G band areas.[8,13] These ratios have been quantitatively analyzed, since they reflect the structural defects in the basal planes of graphene layers.[14] XRD profile analysis for carbon blacks has been used in earlier studies to obtain two structural parameters, crystallite stacking height (Lc) and the interplanar distance.[24] The bands observed in the XRD patterns for diesel soot and other carbonaceous materials have been identified as (002), (100), (004), and (110); and the (002) band has

been used to calculate both the interplanar layer spacing (d_{002}) of crystallites composed of stacked graphene layers using Bragg's law,[14] and the average crystallite height (Lc) using the Debye-Scherrer equation.[25] Finally, TGA has been widely applied in determining structural stability and direct studies on the kinetics of diesel soot oxidation, based on the change in weight of the carbonaceous material.[6,7,9]

Based on the SEM, TEM/HRTEM, nitrogen sorption, Raman spectroscopy, XRD, and TGA analyses, we present four structure-activity correlations in this work, viz., (i) light-off temperature vs. SEM particle size, (ii) light-off temperature vs. surface area, (iii) light-off temperature vs. Raman D1/G peak ratio, and (iv) light-off temperature vs. XRD crystallite height. These structure-activity correlations could be critical for the improved design and operation of DPFs.

3.2. Experimental Section

3.2.1 Materials

The two diesel engine soot samples (diesel soot-1 and diesel soot-2) were provided by Corning (see Table 3.1 for engine operating conditions), whereas ten carbon black samples (Mogul-E, Monarch 280, Monarch 1300, Monarch 1400, Printex-G, Printex-U, Printex-XE2B, Regal 330R, Regal 400R, and Vulcan XC 72R) were obtained from various manufacturers/suppliers. Table 3.2 shows the

physical properties and oxidation activity data for all the samples, based on the characterization techniques described next.

Table 3.1. Engine operating conditions during diesel soot sampling. All soot was collected under steady-state operating conditions.

Name	Engine type	Engine swept volume [L]	Rpm [min^{-1}]	Torque [Nm]	Power [kW]	Exhaust gas flow rate [kg/h]
Diesel soot-1	Light-duty	2	3250	50	17	253
Diesel soot-2	Heavy-duty	9.3	1900	373	75	680

Table 3.2. Physical properties and oxidation activity data for carbon black and diesel soot samples.

SN*	Name	Particle size and (standard deviation) [nm]	Surface area [m^2/g]	Raman D1/G intensity ratio [-]	L_C [Å]	T_{10} [°C]	T_{50} [°C]
1	Diesel soot-1	68.5 (16.9)	155	1.39	11.7	541	640
2	Mogul-E	69.7 (17.0)	49	0.99	14	548	630
3	Monarch 280	73.0 (22.3)	46	0.80	13.3	617	674
4	Monarch 1300	21.5 (2.8)	342	2.13	10.4	482	563
5	Monarch 1400	20.9 (3.0)	443	1.52	11.5	513	616
6	Printex-G	74.0 (14.0)	45	0.75	18.5	637	696
7	Printex-U	68.6 (28.9)	96	2.07	10.9	543	615
8	Printex-XE2B	26.7 (3.0)	1005	1.71	11.2	479	547
9	Regal 330R	32.4 (7.6)	98	1.36	13.1	587	659
10	Regal 400R	46.1 (8.4)	91	0.99	12.6	565	641
11	Vulcan XC 72R	39.3 (5.1)	213	1.32	12.1	631	692
12	Diesel soot-2	40.5 (11.6)	351	1.67	7.7	548	620

3.2.2. Material Characterization

3.2.2.1. X-Ray Powder Diffraction Studies

XRD studies were performed on the carbon black and diesel soot samples to investigate the structure. The patterns were analyzed with a Rigaku Ultima IV diffractometer using Cu Kα (λ = 0.15406 nm) radiation. The phases were identified by using the International Center for Diffraction Data (ICDD) data base. Average crystallite height (Lc) of the carbon black and diesel soot samples was determined using the Debye-Scherrer equation based on the (002) peak.

3.2.2.2. Scanning Electron Microscopy (SEM)

Morphological and particle size analyses of the carbon black materials and diesel soot samples were carried out using a Zeiss DSM 982 Gemini FE-SEM with a beam current of 1 mA and a Schottky emitter operating at 2 kV. FE-SEM sample preparation was done by suspending the samples in absolute ethanol and then a drop of the suspension was dispersed on Au coated silicon chips formerly mounted onto stainless-steel sample holders with double-sided carbon tape. The average primary particle size of carbon black and diesel soot samples was determined using FE-SEM images obtained under 50,000 and 100,000 magnifications, by measuring the diameter of nearly 200 particles for each sample. The standard deviation for each sample is listed in Table 3.2.

3.2.2.3. Transmission Electron Microscopy (TEM)

The HRTEM studies were carried out using a JEOL 2010 instrument with an accelerating voltage of 200 kV. The samples were prepared by dispersing the material in ethanol. A drop of a homogeneous like dispersion was loaded on to a carbon coated copper grid and allowed to dry before analysis. The obtained TEM images were used to analyze the microstructure of carbon black and diesel soot samples.

3.2.2.4. N_2 Sorption Studies

The nitrogen sorption experiments were conducted using a Quantachrome Autosorb iQ_2 surface area system. Prior to the experiments, all samples were

degassed at 200 °C for 12 h. The Brunauer−Emmett−Teller (BET) method was used to determine the specific surface area of carbon black samples from data obtained at P/P_o between 0.05 and 0.30. The pore size distribution and the pore volume were calculated from the desorption data using the BJH method.

3.2.2.5. Raman Spectroscopy

Raman measurements were taken at room temperature on a Renishaw 2000 Ramascope attached to a CCD camera, with an Ar^+ ion laser (514.4 nm) as the excitation source. Before each measurement was taken, the spectrometer was calibrated with a silicon wafer. Curve fitting for the determination of spectral parameters was performed with the software program GRAMS/32.

3.2.2.6. Thermo Gravimetric Analysis

TGA experiments were performed in 10% O_2 atmosphere (balance Ar) using a TGA Q5000 IR analyzer from TA instruments. The temperature ramp rate was 5 °C/min. Light-off temperatures corresponding to 10% and 50% conversion are denoted as T_{10} and T_{50}, respectively.

3.3. Results

3.3.1. Effect of particle size on oxidation activity

FE-SEM images (Figure 3.1) of some carbon blacks (Monarch 1400, Monarch 280, Printex-U) and diesel soot-1 show the agglomerates, which

are composed of their fundamental units called primary particles.[7] The average particle size (diameter) was estimated by analysis of nearly 200 particles in the FE-SEM images. The average particle size of all the samples varied between 20 nm and 74 nm. Monarch 1400 (Figure 3.1a) and Monarch 1300 (not shown) had the smallest average particle sizes (20.9 nm and 21.5 nm, respectively). On the other hand, Monarch 280 (Figure 3.1b) and Printex-G (not shown) had the largest particle sizes (73 nm and 74 nm, respectively). Printex-U (Figure 3.1c) and diesel soot-1 (Figure 3.1d) had almost the same average particle sizes (68.5 nm vs. 68.6 nm, respectively), supporting the idea of morphological similarity between the two materials.[26]

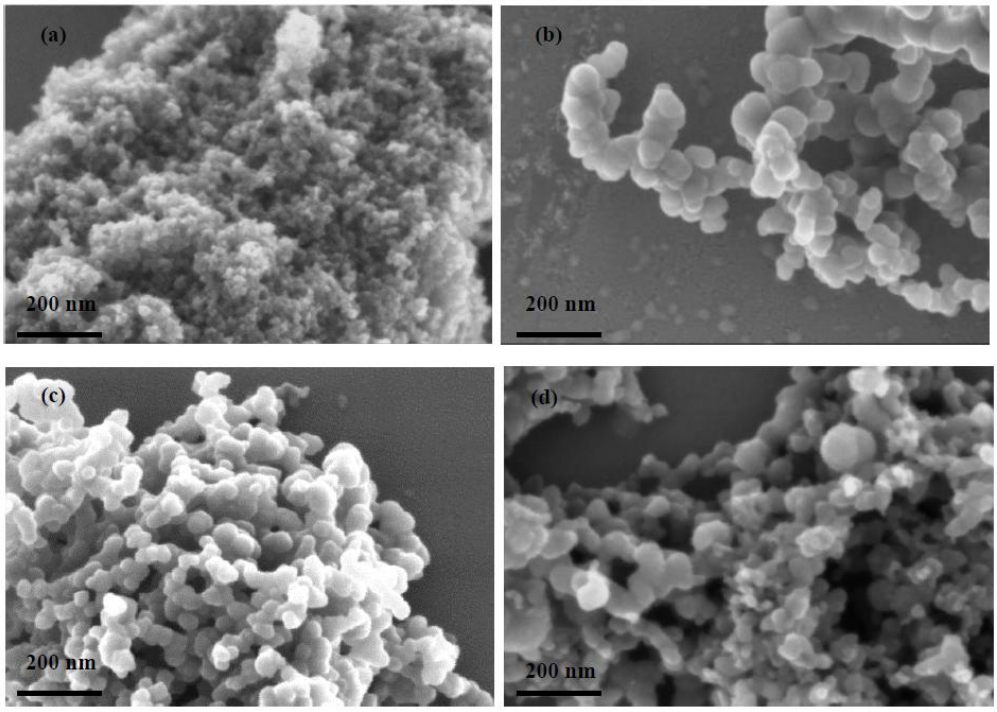

Figure 3.1. FE-SEM images for (a) Monarch 1400, (b) Monarch 280, (c) Printex U, and (d) diesel soot-1.

As the samples selected in our work had a broad distribution of average particle sizes, the oxidation activity data obtained from TGA were correlated with the average particle sizes, as shown in Figure 3.2. Even though the data did not follow a clear correlation for all the points (e.g., Vulcan XC 72R and Printex-XE2B were outliers), a general trend that the oxidation activity decreases (i.e., the light-off temperatures T_{10} and T_{50} increase) as the average particle size increases was observed, consistent with the literature studies.[1]

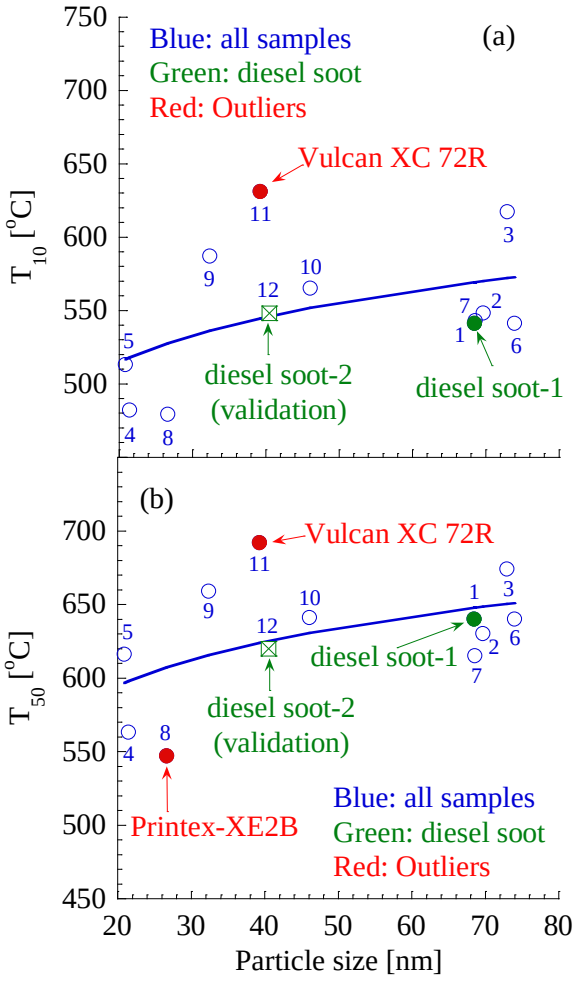

Figure 3.2. Correlation for oxidation activity with the average initial particle size. Panels a and b correspond to the light-off temperatures T_{10} and T_{50}, respectively.

The average particle size of diesel soot-2 (Figure 3.3) was 40.5 nm, composed of smaller particles than diesel soot-1. To validate the structure-activity correlations in Figure 3.2, we also included the diesel soot-2 sample in the plot, which showed that the diesel soot-2 sample was very close to the correlation trend line.

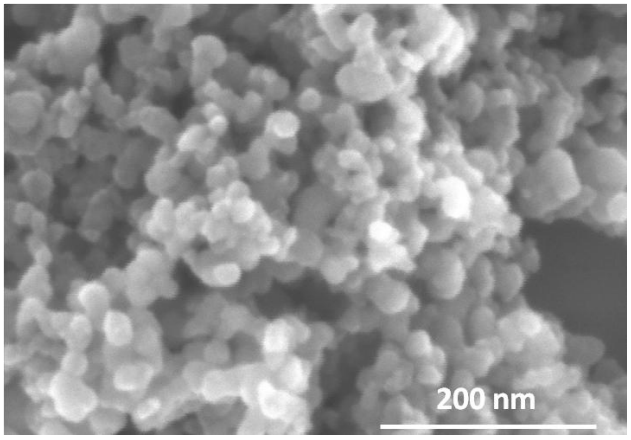

Figure 3.3. FE-SEM image for diesel soot-2.

3.3.2. Effect of surface area on oxidation activity

Figures 3.4a and 3.4b show the variation of light-off temperatures T_{10} and T_{50}, respectively, with the specific surface area. The general trend was that the oxidation activity increased (i.e., T_{10} and T_{50} decreased) as the specific surface area increased. The correlation for T_{10} was better than that for T_{50}, which was expected since after a 50% mass loss, the significance of surface area should be lower due to less contribution by the inner coagulated crystallites to the total surface area.[27] The specific surface area of diesel soot-1 and carbon blacks ranged between 45 m^2/g and 1005 m^2/g, with Printex-G and Printex-XE2B showing the lowest and highest surface areas, respectively. In the correlation plots, Vulcan XC 72R was again identified as an outlier. Diesel soot-1 had a

moderate specific surface area of 155 m^2/g; and correspondingly had a moderate oxidation activity.

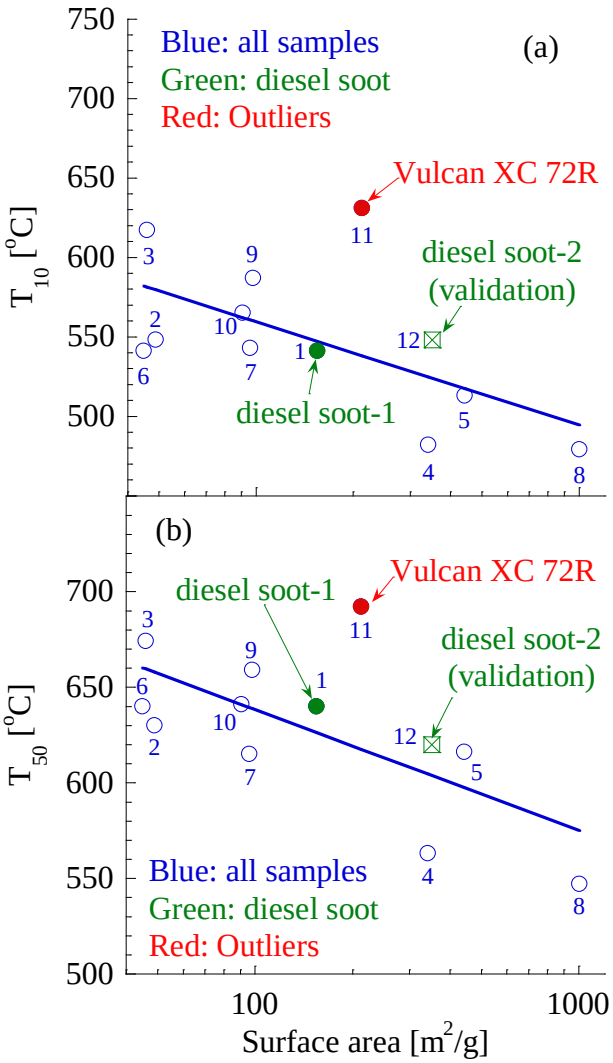

Figure 3.4. Correlation for oxidation activity with the specific surface area. Panels a and b correspond to the light-off temperatures T_{10} and T_{50}, respectively.

The specific surface area of diesel soot-2 was 351 m^2/g, which was greater than that of diesel soot-1. To validate these structure-activity correlations

in Figures 3.4a and 3.4b, we also included diesel soot-2 in the plots, which showed that diesel soot-2 was reasonably close to the correlation trend line.

3.3.3. Effect of degree of organization on oxidation activity

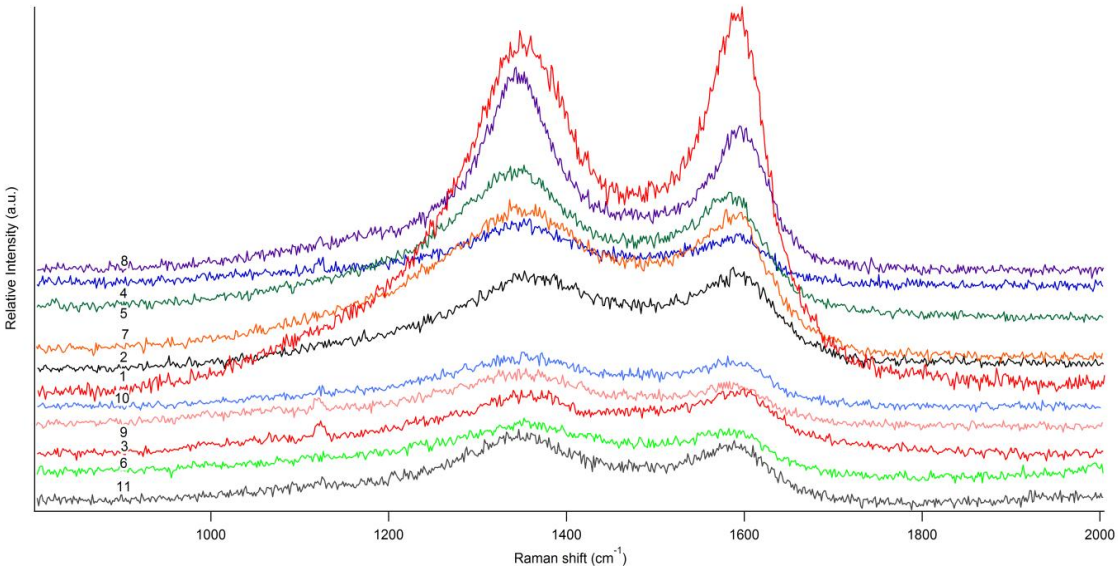

Figure 3.5. Raman spectra for carbon blacks and diesel soot-1.

Raman spectra (λ= 514 nm) shown in Figure 3.5 for carbon blacks and diesel soot-1 consisted of two overlapping bands, one around 1600 cm^{-1} (G band) and the other around 1350 cm^{-1} (D band). The curved fitted spectra (not shown) showed the presence of five bands (G, D1, D2, D3, and D4 around 1580, 1345, 1620, 1500, and 1200 cm^{-1}, respectively). From these spectra, a ratio of the intensity of the D1 and G band peaks could be used as a measure of the relative degree of organization, i.e., amorphous nature. Figure 3.6 shows the variation of T_{50} with the D1/G intensity ratios of carbon blacks and diesel soot-1.

The nearly linear relationships clearly indicated a strong dependence of the oxidation activity on the degree of organization of the carbonaceous material. Samples with higher D1/G intensity ratios had lower T_{50} and vice versa. Here, the D1/G intensity ratio varied between 0.75 and 2.13, with Printex-G and Monarch 1300 having the lowest and highest ratios, respectively. The D1/G intensity ratio for diesel soot-1 was 1.39, which was considered as a moderate value of the series, corresponding to moderate oxidation activity.

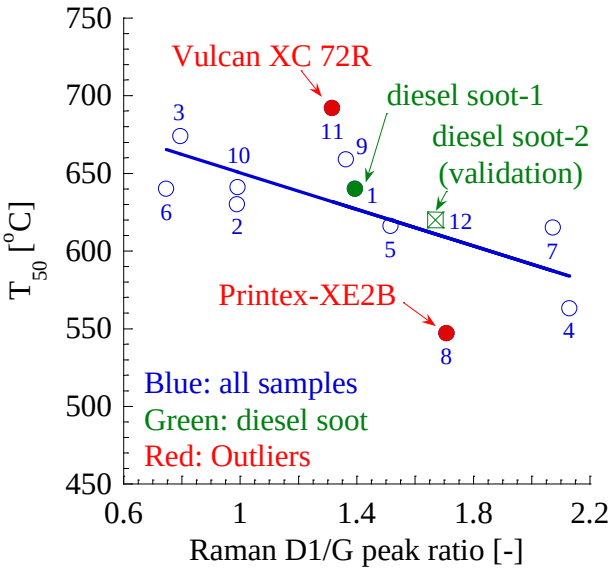

Figure 3.6. Correlation for oxidation activity with the intensity ratio of the Raman D1 and G peaks.

Raman spectrum of diesel soot-2 (Figure 3.7) had a D1/G intensity ratio of 1.67. To validate the structure-activity correlation in Figure 3.6, we also included diesel soot-2 in the plot, which showed that the diesel soot-2 was very close to the correlation trend line.

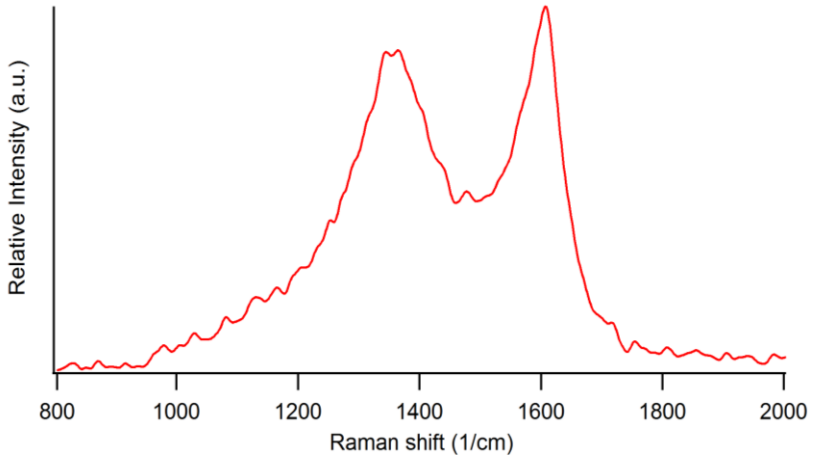

Figure 3.7. Raman spectrum (λ=514 nm) for diesel soot-2.

3.3.4. Effect of crystallite stacking height on oxidation activity

Figure 3.8 shows the XRD patterns observed for commercial carbon blacks and diesel soot-1. The patterns consisted of two broad diffuse peaks, one indexed as the crystalline reflection (002) and the other as two dimensional lattice reflections (10*l*), which could be considered as a poorly crystalline graphite X-ray pattern.

Figure 3.9 shows the variation of T_{50} with crystallite stacking height (Lc). Samples with a lower Lc showed a higher oxidation activity and vice versa. Here, Lc ranged between 10.4 Å to 18.5 Å, with Monarch 1300 and Printex-G showing the lowest and highest Lc, respectively. Diesel soot-1, which showed good agreement with the observed trend, had crystallites with an average height of 11.7 Å and might be composed of 4 graphene layers (d_{002} = 3.62 Å).

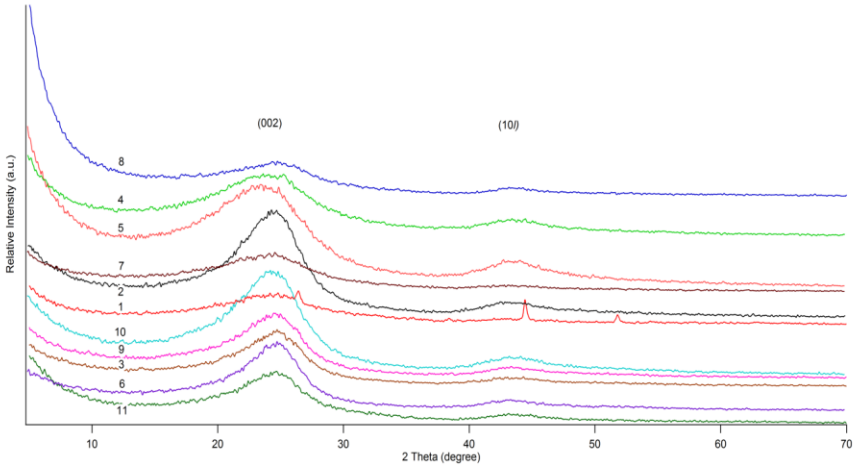

Figure 3.8. XRD patterns for carbon blacks and diesel soot-1.

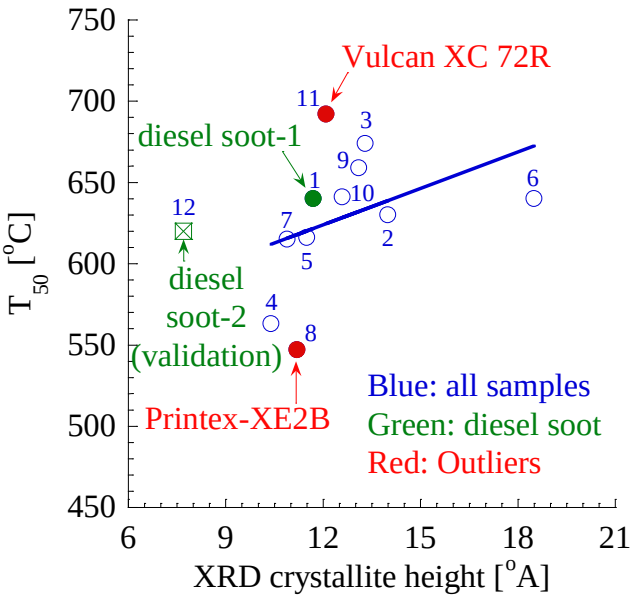

Figure 3.9. Correlation for oxidation activity with the crystallite stacking height.

The crystalline reflection (002) of the XRD pattern of diesel soot-2 (Figure 3.10) showed Lc of 7.7 Å (d_{002} = 3.60 Å), which was the smallest of the series and outside of the range for the ten carbon blacks and diesel soot-1. To validate

the structure-activity correlation in Figure 3.8, we also included diesel soot-2 in the plot, which showed that the diesel soot-2 did *not* lie close to the correlation trend line. This indicates that the correlation of oxidation activity with Lc is the poorest of the four correlations presented in this work.

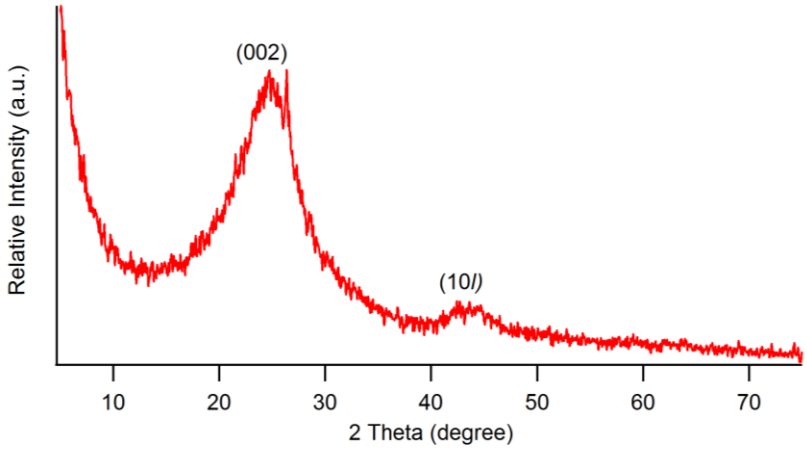

Figure 3.10. XRD spectrum for diesel soot-2.

3.4. Discussion

The morphology and the microstructure of carbon black and diesel soot samples, along with their correlations with the oxidation behavior in Figure 3.2 can be explained with a careful analysis of their TEM and HRTEM images. As a general trend, smaller particles show lower T_{10} and T_{50} values with higher oxidation activities, whereas the larger particles show higher T_{10} and T_{50} values with lower oxidation activities. Spillover of oxidant onto soot surface followed by adsorption at the active carbon sites are found to be important in many oxidation mechanisms proposed for soot oxidation.[28] Hence, smaller particles, having a larger surface area to volume ratio, should have better contact with the oxidant, resulting in higher oxidation activity. The average particle size influences the oxidation activity, but is not a very clear descriptor in such correlations; therefore, additional structural features are also studied and described next.

Even though the carbon gasification mechanism is quite complex,[29] influence of surface area on the oxidation behavior of carbon black and diesel soot samples is expected to provide important insights, as the chemisorption of oxidant on the active surface sites and the subsequent formation of oxygen surface complexes are expected to strongly depend on the specific surface area. In Figure 3.4, we proposed a correlation for oxidation activity vs. BET surface area. To explain the trend and the low vs. high surface areas of certain samples (e.g., Printex-G vs. Printex-XE2B), we propose that the primary particles are composed of two major parts, as shown in Figure 3.11: (i) an inner core made out of several fine particles and several carbon layers with distorted structure,

and (ii) an outer shell made out of micro crystallites with periodic orientation of planar graphene layers.[17]

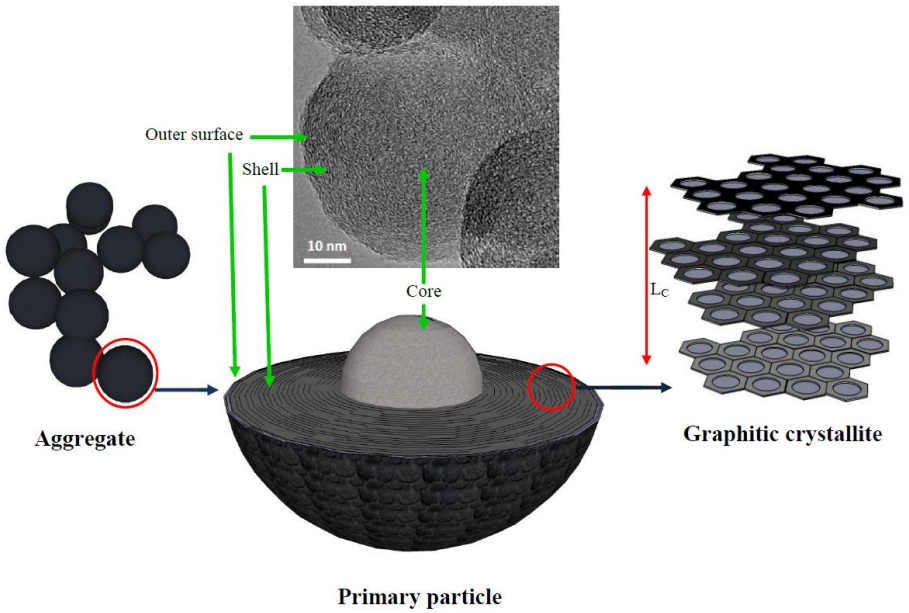

Figure 3.11. Proposed structure of carbon black.

The HRTEM image of Printex-G (Figure 3.12) shows the microstructure of individual primary particles. Lattice fringe contrast from the stacking of the graphene units is clearly visible in the shell of the primary particle. Both the shell and the outer surface of the particle show long range ordered contrast, indicating a highly dense shell and a less defected surface, and hence a very low surface area (45 m^2/g). The low surface area of Printex-G results in one of the samples with very low oxidation activity.

On the other hand, the overview HRTEM image of Printex-XE2B (Figure 3.13a) reveals the microstructure of the primary particle shell in which the lattice fringes are clearly visible but they are with weak long range order. The curved

graphene layers form a less dense shell, whereas shells of the neighbouring particles appear to be merged, forming a continuous surface with a large number of small crystallites (Figure 3.13b). A higher amount of crystallites confirms the presence of a higher number of crystallite edges, which in turn result in a higher density of surface active sites. The high surface area of Printex-XE2B is responsible for the highest oxidation activity.

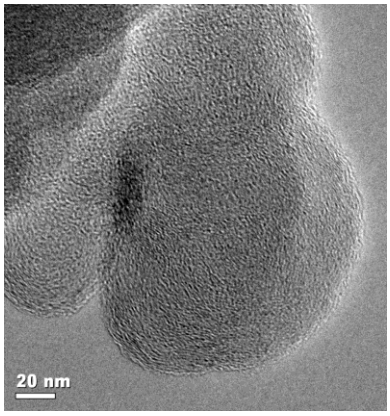

Figure 3.12. Overview HRTEM image of Printex-G.

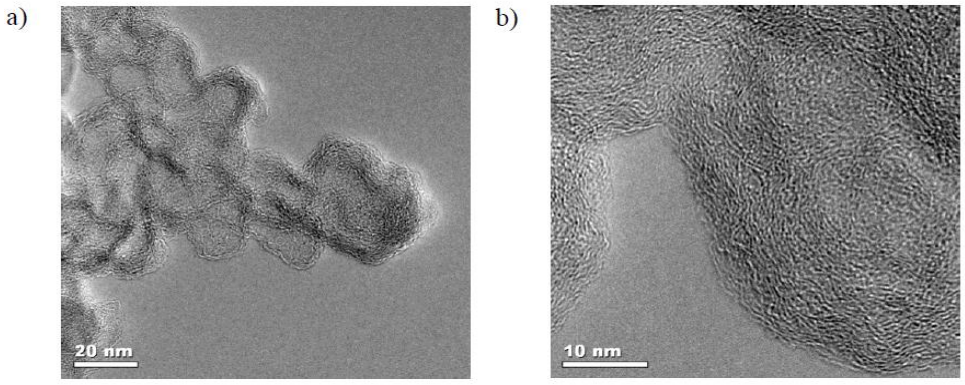

Figure 3.13. (a) Overview and (b) enlarged HRTEM images of Printex-XE2B.

The agglomerated primary particles are comprised of graphite-like crystalline and amorphous domains;[23] and carbon blacks change into coagulations of crystallites as oxidation proceeds.[27] Therefore, it is important to understand the microstructure of the carbonaceous materials. As mentioned earlier, Raman spectroscopy can be used for the analysis of crystalline long range order (e.g., graphitic materials)[22] as well as molecular structures with a short range order (e.g., amorphous carbon or disturbed graphitic lattices).[23] The curve fitted Raman spectra in Figure 3.5 for carbon blacks and diesel soot-1 contain one first order band at around 1585 cm^{-1} (G band) and four additional bands (D1, D2, D3, and D4 bands, represented by D band), which are characteristic for disordered graphite structure. The G band stands for the in-plane bond-stretching motions of the sp^2 hybridized carbon atoms of graphene plane, which has the E_{2g} symmetry.[4] The D1 band, which appears at around 1345 cm^{-1}, is associated with the graphitic lattice motions with A_{1g} symmetry of carbon atoms from graphene layers close to the lattice disturbances.[23]

In the correlation for oxidation activity vs. degree of organization (Figure 3.6), Monarch 1300 had the highest D1/G intensity ratio, and hence the lowest degree of organization. The HRTEM image of Monarch 1300 in Figure 3.14 shows twisted ribbon-like molecular units in addition to the basic structural units of graphene; they are strongly curved, indicating less dense and highly disordered crystalline (highly amorphous) structure. In some areas, the crystallites are not clearly observed due to the presence of disordered,

amorphous carbon. This structural feature of Monarch 1300 brings about a faster gasification mechanism, and hence a high oxidation activity.

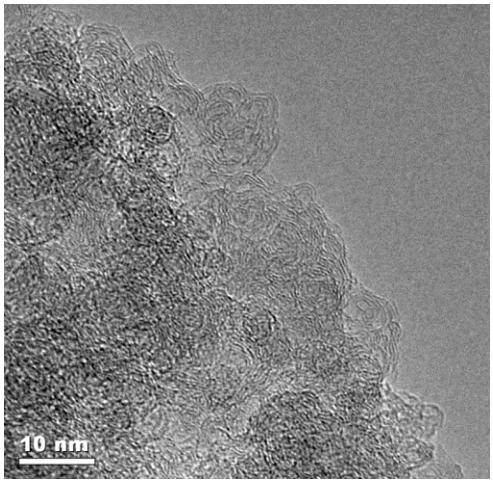

Figure 3.14. Overview HRTEM image of Monarch 1300.

On the other hand, Printex-G had the lowest D1/G intensity ratio, and hence the highest degree of organization. The HRTEM image of Printex-G in Figure 3.12 consists of more pronounced long-range ordered onion-like graphene structures with very low curvature for the graphitic sheets. The highly dense, less spaced, and ordered structure limits the gasification process and leads to low oxidation activity.

Both diesel soot-1 and diesel soot-2 have moderate D1/G intensity ratios (1.4 and 1.67, respectively); hence they show moderate oxidation activities. The HRTEM image of diesel soot-1 in Figure 3.15 shows the presence of primary soot particles with different shapes as well as dark particles of metal oxides with clearly observed lattice fringes. Overall, the D1/G intensity ratio based on Raman

spectroscopy is an excellent *descriptor* for the oxidation activity of the carbon black and diesel soot samples.

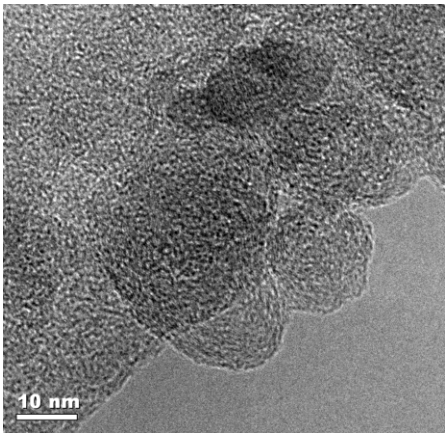

Figure 3.15. Overview HRTEM image of diesel soot-1.

The carbon black particles are composed of densely packed stacks of almost perfect graphite layers;[24] and it is important to identify the effect of structural parameters of a single crystallite on the oxidation behavior. XRD profile analysis for carbon blacks has been used in the past studies to obtain two structural parameters, crystallite stacking height (Lc) and the interplanar distance.[24] The XRD patterns consist of two broad diffuse peaks, one indexed as the crystalline lattice reflection (002) and the other as two dimensional lattice reflections (100)/(101).[30] The absence of (hkl) peaks indicates random orientation around the layer normal and lack of three dimensional order.[24]

Diesel soot-2 had the lowest Lc, whereas Printex-G had the highest Lc. HRTEM image of diesel soot-2 in Figure 3.16 shows that the primary particles have highly curved graphene layers, which are loosely stacked on each other. The curvature, formed due to a less sp^2 character of the graphene layers,

discourages the formation of a higher number of stacks per crystallite, which increases its oxidation activity by inducing a faster gasification mechanism. Similar features are observed from the HRTEM image of Monarch 1300 in Figure 3.14.

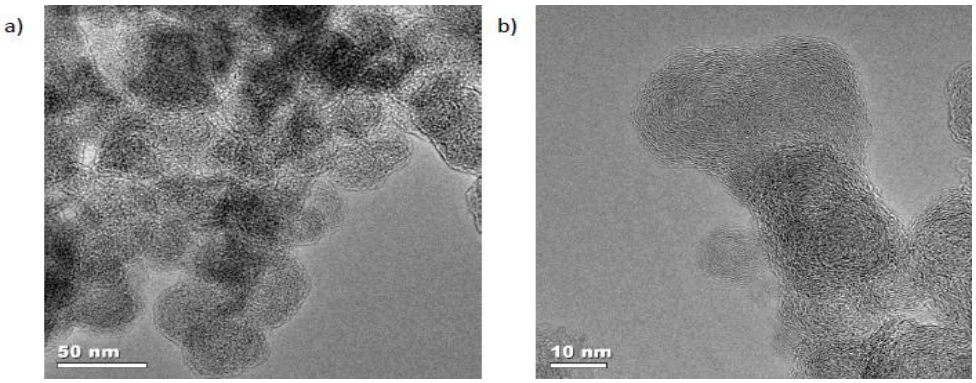

Figure 3.16. (a) TEM and (b) HRTEM images of diesel soot-2.

On the other hand, the HRTEM image of Printex-G in Figure 3.12 shows the closely packed graphene layers with a very low curvature, indicating a higher sp^2/sp^3 hybridized carbon ratio. Overall, larger crystallite stacking height is associated with smaller amount of surface carbons being exposed to the oxidant; therefore more energy is needed to dissociate the graphene planes from the crystallite, resulting in elevated oxidation temperatures (i.e., low oxidation activity).

In the aforementioned structure-activity correlations, Vulcan XC 72R and Printex-XE2B were determined as the most common outliers. Here, we provide a possible explanation for the different behavior of these two samples.

Vulcan XC 72R (the first outlier) is much more difficult to oxidize compared to the predicted oxidation activity based on the correlations. The HRTEM images of Vulcan XC 72R in Figure 3.17 confirm the presence of three types of primary particles: first being the smallest (~10 nm) and composed of curved, more spaced graphene layers and agglomerated in-order to form chain like structures, second being the most abundant and middle sized (~39 nm) (Figure 3.17a), and third being the largest (~84 nm) and the least abundant (Figure 3.17b). Both middle sized and large particles are composed of planar, closely packed graphene layers. Although the relative abundance of middle sized (~39 nm) particles in the sample is the highest, the smallest (~10 nm) and more amorphous particles may have been more observed in Raman and XRD studies. Due to its amorphous nature, the smaller primary particles may have a higher surface area, which results in a moderate surface area value (213 m^2/g) for Vulcan XC 72R. Since, both the XRD peaks and Raman peaks become narrower with the development of crystallographic structures,[31] the peaks originating from larger, more crystalline primary particles may have been obscured inside the broad peaks arising due to the smallest (~10 nm), more amorphous particles. Hence, a larger D1/G intensity ratio and a lower Lc value are observed for Vulcan XC 72R.

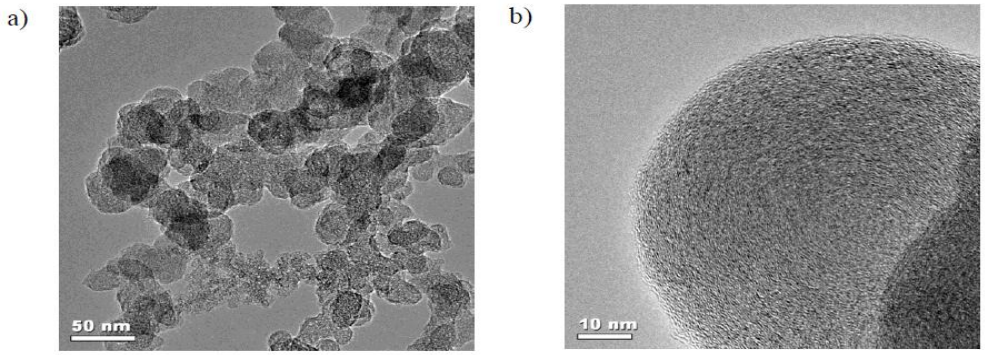

Figure 3.17. HRTEM images of (a) the smallest (~10 nm) and middle sized (~39 nm), and (b) the largest (~84 nm) particles of Vulcan XC 72R.

On the other hand, Printex-XE2B (the second outlier) is easier to oxidize compared to the predicted oxidation activity based on the correlations. The TEM image of Printex-XE2B in Figure S8b shows that the shell of the primary particle is very narrow, and the core has an amorphous nature. Although the Raman and XRD data analyses give information about the crystallinity of the shell, they do not represent depth analyses. Hence, the T_{50} value of Printex-XE2B, which includes both shell and amorphous core oxidation, is lower than expected. Also, the very high surface area observed for Printex-XE2B (1005 m^2/g), observed due to the high concentration of surface active sites, might be responsible for its low T_{10} and T_{50} values.

We combine the aforementioned structure-activity correlations in Figure 3.18, which presents an overall summary schematic of the dependence of oxidation activity on the structure for all the samples considered in this work. A general trend could be explained from most of the samples. Carbonaceous

materials with smaller particle sizes, higher surface areas, lower degree of organization, and lower crystallite stacking heights are easier to oxidize and vice versa.

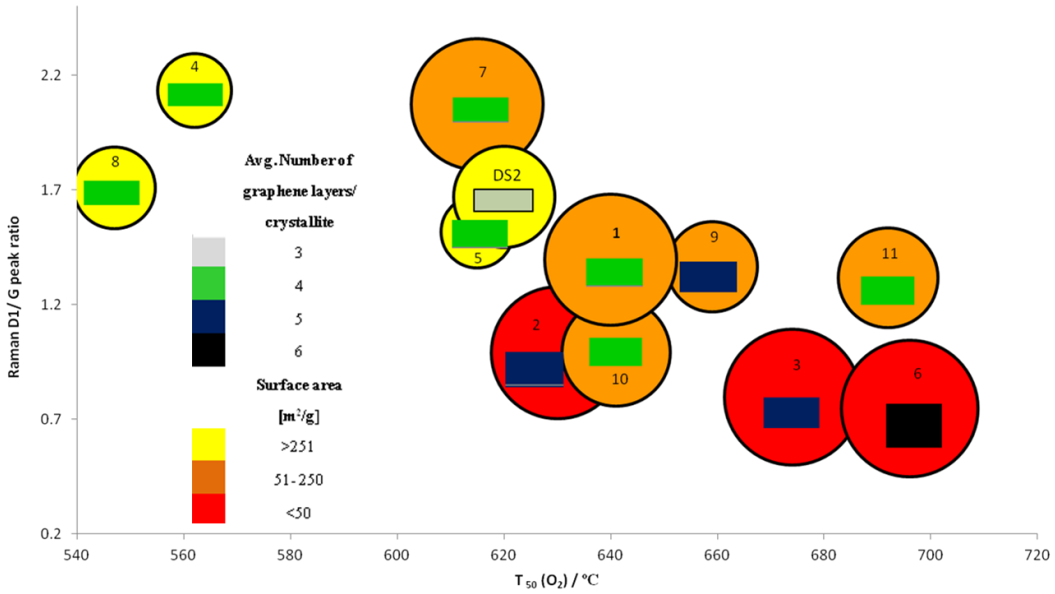

Figure 3.18. Summary of the variation of oxidation activity as correlated to particle size, surface area, degree of organization, and crystallite stacking height.

3.5. Conclusions

Our comprehensive investigation of ten commercial carbon black samples and two diesel engine soot samples has provided novel and clear insights that explain the origin of their oxidation activity linked to their structural characteristics. Four structure- activity correlations were identified by analyzing their structural characteristics, such as initial primary particle size, specific surface area, degree of organization (amorphous nature), and crystallite stacking

height, and their oxidation activity using a diesel engine soot sample (diesel soot-1) and ten commercial carbon black materials. Validity of these correlations was proven by the structure and reactivity analysis of the second diesel engine soot sample (diesel soot-2). Such fundamental understanding combined with the unique soot structure-activity correlations will be key to the improved design and operation of Diesel Particulate Filters.

References

(1) van Setten, B. A. A. L.; Makkee, M.; Moulijn, J. A. Science and technology of catalytic diesel particulate filters. *Catal. Rev. Sci. Eng.* **2001**, *43* (4), 489-564.

(2) Pöschl, U. Atmospheric Aerosols: Composition, Transformation, Climate and Health Effects. *Angew. Chem. Int. Ed.* **2005**, *44* (46), 7520-7540.

(3) Risom, L.; Dybdahl, M.; Bornholdt, J.; Vogel, U.; Wallin, H.; Møller, P.; Loft, S. Oxidative DNA damage and defence gene expression in the mouse lung after short-term exposure to diesel exhaust particles by inhalation. *Carcinogenesis* **2003**, *24* (11), 1847-1852.

(4) Knauer, M.; Schuster, M. E.; Su, D.; Schlögl, R.; Niessner, R.; Ivleva, N. P. Soot Structure and Reactivity Analysis by Raman Microspectroscopy, Temperature-Programmed Oxidation, and High-Resolution Transmission Electron Microscopy. *J. Phys. Chem. A* **2009**, *113* (50), 13871-13880.

(5) Palotás, Á. B.; Rainey, L. C.; Feldermann, C. J.; Sarofim, A. F.; Vander Sande, J. B. Soot morphology: An application of image analysis in high-resolution transmission electron microscopy. *Microsc. Res. Tech.* **1996**, *33* (3), 266-278.

(6) Clague, A. D. H.; Donnet, J. B.; Wang, T. K.; Peng, J. C. M. A comparison of diesel engine soot with carbon black. *Carbon* **1999**, *37* (10), 1553-1565.

(7) Stanmore, B. R.; Brilhac, J. F.; Gilot, P. The oxidation of soot: a review of experiments, mechanisms and models. *Carbon* **2001**, *39* (15), 2247-2268.

(8) Song, J.; Alam, M.; Boehman, A. L.; Kim, U. Examination of the oxidation behavior of biodiesel soot. *Combust. Flame.* **2006**, *146* (4), 589-604.

(9) Müller, J. -O.; Su, D. S.; Jentoft, R. E.; Wild, U.; Schlögl, R. Diesel Engine Exhaust Emission: Oxidative Behavior and Microstructure of Black Smoke Soot Particulate. *Environ. Sci. Technol.* **2006**, *40* (4), 1231-1236.

(10) Su, D. S.; Jentoft, R. E.; Müller J-; Rothe, D.; Jacob, E.; Simpson, C. D.; Tomovic, Z.; Müllen, K.; Messerer, A.; Pöschl, U.; Niessner, R.; Schlögl, R. Microstructure and oxidation behaviour of Euro IV diesel engine soot: a comparative study with synthetic model soot substances. *Catal. Today* **2004**, *90* (1-2), 127-132.

(11) Boehman, A. L.; Song, J.; Alam, M. Impact of Biodiesel Blending on Diesel Soot and the Regeneration of Particulate Filters. *Energy Fuels* **2005**, *19* (5), 1857-1864.

(12) Müller J. -O.; Su, D. S.; Jentoft, R. E.; Kröhnert, J.; Jentoft, F. C.; Schlögl, R. Morphology-controlled reactivity of carbonaceous materials towards oxidation. *Catal. Today* **2005**, *102–103*, 259-265.

(13) Schmid, J.; Grob, B.; Niessner, R.; Ivleva, N. P. Multiwavelength Raman Microspectroscopy for Rapid Prediction of Soot Oxidation Reactivity. *Anal. Chem.* **2011**, *83* (4), 1173-1179.

(14) Lapuerta, M.; Oliva, F.; Agudelo, J. R.; Boehman, A. L. Effect of fuel on the soot nanostructure and consequences on loading and regeneration of diesel particulate filters. *Combust. Flame* **2012**, *159* (2), 844-853.

(15) Kirchner, U.; Vogt, R.; Natzeck, C.; Goschnick, J. Single particle MS, SNMS, SIMS, XPS, and FTIR spectroscopic analysis of soot particles during the AIDA campaign. *J. Aerosol. Sci.* **2003**, *34* (10), 1323-1346.

(16) Cain, J. P.; Gassman, P. L.; Wang, H.; Laskin, A. Micro-FTIR study of soot chemical composition-evidence of aliphatic hydrocarbons on nascent soot surfaces. *Phys. Chem. Chem. Phys.* **2010**, *12* (20), 5206-5218.

(17) Ishiguro, T.; Takatori, Y.; Akihama, K. Microstructure of diesel soot particles probed by electron microscopy: First observation of inner core and outer shell. *Combust. Flame* **1997**, *108* (1-2), 231-234.

(18) Darmstadt, H.; Roy, C.; Kaliaguine, S.; Joo, S. H.; Ryoo, R. Pore structure and graphitic surface nature of ordered mesoporous carbons probed by low-pressure nitrogen adsorption. *Micropor. Mesopor. Mat.* **2003**, *60* (1-3), 139-149.

(19) Ustinov, E. A.; Do, D. D.; Fenelonov, V. B. Pore size distribution analysis of activated carbons: Application of density functional theory using nongraphitized carbon black as a reference system. *Carbon* **2006**, *44* (4), 653-663.

(20) Borah, D.; Satokawa, S.; Kato, S.; Kojima, T. Characterization of chemically modified carbon black for sorption application. *Appl. Surf. Sci.* **2008**, *254* (10), 3049-3056.

(21) Darmstadt, H.; Roy, C. Comparative investigation of defects on carbon black surfaces by nitrogen adsorption and SIMS. *Carbon* **2001**, *39* (6), 841-848.

(22) Jawhari, T.; Roid, A.; Casado, J. Raman spectroscopic characterization of some commercially available carbon black materials. *Carbon* **1995**, *33* (11), 1561-1565.

(23) Sadezky, A.; Muckenhuber, H.; Grothe, H.; Niessner, R.; Pöschl, U. Raman microspectroscopy of soot and related carbonaceous materials: Spectral analysis and structural information. *Carbon* **2005**, *43* (8), 1731-1742.

(24) Peng, W. G.; Strauss, M.; Pieper, T.; Kilian, H. G. X-ray diffraction and model calculation on carbon blacks. *Mol. Phys.* **1993**, *80* (2), 419-429.

(25) Fujimoto, H. Theoretical X-ray scattering intensity of carbons with turbostratic stacking and AB stacking structures. *Carbon* **2003**, *41* (8), 1585-1592.

(26) Hansen, C. W.; Kamp, C. J.; Skoglundh, M.; Andersson, B; Carlsson P. -A. Experimental Method for Kinetic Studies of Gas–Solid Reactions: Oxidation of Carbonaceous Matter. *J. Phys. Chem. C* **2011**, *115* (32), 16098-16108.

(27) Kamegawa, K.; Nishikubo, K.; Yoshida, H. Oxidative degradation of carbon blacks with nitric acid (I)—Changes in pore and crystallographic structures. *Carbon* **1998**, *36* (4), 433-441.

(28) Krishna, K.; Bueno-López, A.; Makkee, M.; Moulijn, J. A. Potential rare earth modified CeO_2 catalysts for soot oxidation: I. Characterisation and catalytic activity with O_2. *Appl. Catal. B-Environ.* **2007**, *75* (3-4), 189-200.

(29) Jeguirim, M.; Tschamber, V.; Brilhac, J. F.; Ehrburger, P. Oxidation mechanism of carbon black by NO_2: Effect of water vapour. *Fuel* **2005**, *84* (14-15), 1949-1956.

(30) Saenko, N. S. The X-ray diffraction study of three-dimensional disordered network of nanographites: Experiment and theory. *Physics Procedia* **2012**, *23*, 102-105.

(31) Xue, P.; Gao, J.; Bao, Y.; Wang, J.; Li, Q.; Wu C. An analysis of microstructural variations in carbon black modified by oxidation or ultrasound. *Carbon* **2011**, *49* (10), 3346-3355.

APPENDIX I: FUTURE WORK

This appendix present some ideas for future work with metal oxides and metal sulfides for catalytic applications.

1. Cu impregnated mesoporous silica core shell nanoreactor which contains Pd, MnO_2, and BaO nanopartitcles in its inner wall can be synthesized for catalytic reduction of NO_x in the presence of SO_2. The synthetic method will be multistep which can be summarized with two steps involving (1) synthesis of MnO_2, BaO, and Pd loaded carbon nanosphere using microwave energy and (2) synthesis of Cu impregnated silica mesoporous shells around the nanospheres followed by removal of carbon particles by calcination. The synthesized hollow shell nanoreactors will be expected to show high reactivity, high NO_x diffusion in the storage material, high thermal stability with no particle aggregation, and high SO_2 tolerance capacity.

2. Cobalt sulfide nanoparticle-carbon nanotube (CNT) composites can be synthesized as efficient catalysts for electrochemical/ photoelectrochemical water splitting where hydrogen evolution reactions (HER) and oxygen evolution reactions (OER) take place. First, cobalt oxide nanoparticles supported on CNT will be synthesized using a microwave assisted hydrothermal method. The sulfidation of cobalt oxide nanoparticles will be carried out using H_2S as the sulfur source. The synthesized materials will be expected to show high activities for HER and OER in an acidic medium due high surface areas, small particle sizes,

high conductivity and synergic effects between cobalt sulfide nanoparticles and CNT.

APPENDIX II: PATENTS

1. Pahalagedara, M. N.; Dharmarathna, S.; **Pahalagedara, L. R.**; Suib, S. L. Adsorptive Desulfurization Method. United States Patent and Trademark Office, US Patent Application 65/077,535. Patent Pending, Nov. 2014.

2. **Pahalagedara, L.**; Dharmarathna, S.; Suib, S. L. Method for Removing Soot from Exhaust Gases. United States Patent and Trademark Office, US Patent Application 62/093,180, Patent Pending, Dec. 2014.

3. Kuo, C-H.; **Pahalagedara, L. R.**; Suib, S. L. Adsorptive Desulfurization. United States Patent and Trademark Office, US Patent Application 62/093,196, Patent Pending, Dec. 2014**.**

APPENDIX III: PUBLICATIONS

1.**Pahalagedara, L. R.**; Sharma, H.; Kuo, C-H.; Dharmarathna, S.; Joshi, A.; Suib, S. L.; Mhadeshwar, A. B. Structure and oxidation activity correlations for carbon blacks and diesel Soot. *Energy Fuels* **2012**, *26*, 6757-6764.

2.Sharma, H.; **Pahalagedara, L. R.;** Joshi, A.; Suib, S. L.; Mhadeshwar, A. B. Experimental study of carbon black and diesel engine soot oxidation kinetics using thermogravimetric analysis. *Energy Fuels* **2012**, *26*, 5613–5625.

3.Dharmarathna, S.; King'ondu.; C. K.; Pedrick, W.; **Pahalagedara, L.**; Suib, S.L. Direct Sonochemical Synthesis of manganese octahedral molecular sieve (OMS-2) nanomaterials using cosolvent systems, their characterization, and catalytic applications. *Chem. Mater.* **2012,** *24,* 705-712.

4.Dharmarathna, S.; King'ondu.; C. K.; **Pahalagedara, L.**; Kuo, C-H.; Zhang, Y.; Suib, S. L. Manganese octahedral molecular sieve (OMS-2) catalysts for selective aerobic oxidation of thiols to disulfides, *Appl. Catal. B: environ.* **2014**, *147*, 124-131.

5.Kuo, C-H.; Poyraz, A. S.; Jin, L.; Meng, Y.; **Pahalagedara, L.**; Chen, S-Y., Kriz, D.; Guild, C.; Gudz, A.; Suib, S. L. Heterogeneous acidic TiO_2 nanoparticles for efficient conversion of biomass derived carbohydrates. *Green. Chem.* **2014**, *16*, 785-791.

6.Pahalagedara, M.N.; **Pahalagedara, L. R.**; Kuo, C-H.; Dharmarathna, S.; Suib, S. L. Ordered Mesoporous Mixed Metal Oxides: Remarkable Effect of Pore Size on Catalytic Activity. *Langmuir* **2014**, *30*, 8228-8237.

7.Pahalagedara, M.N.; Samaraweera, M.; Dharmarathna, S.; Kuo, C-H.; **Pahalagedara, L. R.**; Gascon. J.; Suib, S. L. Removal of Azo Dyes: Intercalation into Sonochemically Synthesized NiAl Layered Double Hydroxide. *J. Phys. Chem. C*, **2014**, *118* (31), 17801–17809.

8.**Pahalagedara, L. R**.; Dharmarathna, S.; King'ondu.; C. K.; Pahalagedara, M. N.; Meng, Y.; Kuo, C-H.; Suib, S. L. Microwave-Assisted Hydrothermal Synthesis of α-MnO_2: Lattice Expansion via Rapid Temperature Ramping and Framework Substitution**.** *J. Phys. Chem. C* 2014**,** *118* (35), 20363–20373.

9.Kuo, C-H.; Li, W.; **Pahalagedara, L**.; El-Sawy, A. M.; Kriz, D.; Genz, N.; Guild, C.; Ressler, T.; Suib, S. L.*; He, J.* Understanding the Role of Gold Nanoparticles in Enhancing the Catalytic Activity of Manganese Oxides in Water Oxidation Reactions, *Angew. Chem. Int. Ed.* **2014,** *126*, 1-7.

10.**Pahalagedara, L. R.**; Poyraz, A. S.; Song, W.; Kuo, C-H.; Pahalagedara, M. N.; Meng, Y.; Suib, S. L. Low temperature Desulfurization of H_2S: High sorption capacities by mesoporous cobalt oxide via increased H_2S diffusion. *Chem. Mater.* **2014**, *26,* 6613-6621.

11.**Pahalagedara, L. R.**; Dharmarathna, S.; Kuo, C-H.; Sharma, H.; Joshi, A.; Mhadeshwar, A. B.; Suib, S. L. Comparative analysis of the structure and chemical nature of carbon black and diesel soot (*Manuscript Submitted, Energy Fuels*).

12.**Pahalagedara, L. R.**; Dharmarathna, S.; Wasalathanthri, N.; Pahalagedara, M. N.; Kuo, C-H.; Garces, F.; Suib, S. L. Low temperature diesel soot oxidation by Pt and Co doped manganese oxide octahedral molecular sieves (*In preparation).*

APPENDICES IV: PRESENTATIONS

1.**Pahalagedara, L.;** Sharma, H; Kuo, C-H.; Dharmarathna, S.; Joshi, A.; Suib , S.L.; Mhadeshwar, A. B. Influence of Particle Size and Microstructure On the Oxidation Behavior of Carbon Blacks and Diesel Soot, 12 th AIChE Meeting, Pittsburgh, PA, October 28 – November 3, **2012.**

2.**Pahalagedara, L. R.**; Dharmarathna, S.; Kuo, C-H.; Sharma, H.; Joshi, A.; Suib, S. L.; Mhadeshwar, A. B.; Comparative Analysis of the Structure and Chemical Nature of Carbon Blacks and Diesel Soot , 12 th AIChE Meeting, Pittsburgh, PA, October 28 – November 3, **2012.**

3.**Pahalagedara, L. R**.; Dharmarathna, S.; King'ondu.; C. K.; Pahalagedara, M. N.; Meng, Y.; Kuo, C-H.; Suib, S. L. α-MnO_2 lattice expansion by rapid temperature ramping: A case of Jahn-Teller distortion, 248th ACS National Meeting & Exposition, San Francisco, CA, August 10-14, **2014.**

4.Pahalagedara, M. N.; **Pahalagedara, L. R**.; Dharmarathna, S.; Kuo, C-H.; Suib, S. L. Ca-Al layered double hydroxides (LDH) as a potential sorbent for fuel desulfurization: Application to the removal of dibenzothiophene, 248th ACS National Meeting & Exposition, San Francisco, CA, August 10-14, **2014.**

5.Dharmarathna, S.; Iyer. A.; Li, N.; King'ondu, C. K.; Kuo, C-H; **Pahalagedara**, **L**; Suib, S.L.; Facile Microwave Accelerated Hydrothermal Synthesis of Manganese Oxide Molecular Sieve Nanomaterials and Their Catalytic Applications. The 244th ACS National Meeting, Philadelphia, PA, August 19-22, **2012**